Experimental analysis of the confined behavior of concrete under static and dynamic shear loading

Reem Abdul Rahman

Communauté
UNIVERSITÉ Grenoble Alpes

THÈSE

Pour obtenir le grade de

DOCTEUR DE LA COMMUNAUTE UNIVERSITE GRENOBLE ALPES

Spécialité : **2MGE : Matériaux, Mécanique, Génie civil, Electrochimie**

Arrêté ministériel : 25 mai 2016

Présentée par

Reem ABDUL RAHMAN

Thèse dirigée par **Pascal FORQUIN**

préparée au sein du **Laboratoire Sols, Solides, Structures et Risques**
dans **l'École Doctorale I-MEP2-Ingénierie-Matériaux, Mécanique, Environnement, Energétique, Procédés, Production**

Experimental analysis of the confined behavior of concrete under static and dynamic shear loading

Thèse soutenue publiquement le **7 Février 2018,**
devant le jury composé de :

M. Ignacio CAROL
Professeur, Université Polytechnique de Catalogne, Président
M. Fabrice GATUINGT
Professeur, Ecole normale supérieure de Cachan, Rapporteur
M. François TOUTLEMONDE
Ingénieur Général des Ponts HDR, IFSTTAR, Rapporteur
M. Jean-Luc HANUS
Maître de Conférences, INSA Centre Val de Loire, Examinateur
M. Christophe PONTIROLI
Ingénieur-Chercheur, CEA Gramat, Examinateur
M. Pascal FORQUIN
Professeur, Université Grenoble Alpes, Directeur de thèse
M. Dominique SALETTI
Maître de Conférences, Université Grenoble Alpes, Co-encadrant de thèse

Acknowledgements

I debt my gratitude to a lot of people who helped me to accomplish the PhD thesis.

First, I would like to thank my supervisors Pascal Forquin and Dominique Saletti for the help and guidance through the three years of the thesis. I would also like to thank the members of the jury for their participation in the thesis and specially Francois Toutlemonde and Fabrice Gatuingt for accepting to report my work.

Furthermore, I would like to thank all my colleagues in 3SR, a especial thanks to Bratislav Lukic for the numerous and valuable discussions and Maria Ghannoum who was always available for a chat or a nag.

An experimental thesis can not be done without the help of the technicians, thanks for them and specially for Jean-Luc for his help with the Giga tests.

Besides, I am deeply grateful to my parents and my sisters for their love and support. Thank you for always being there for me.

Finally, a special thanks to Abdallah, for many many things that can not be listed here. And to Racha, who came into my life and encouraged me to finalize my work. Each smile of her was a motivation to focus more on the work even during her sleepless nights.

Abstract

This PhD thesis focuses on studying the confined behavior of concrete under shear loading in static and dynamic conditions. An experimental method based on the Punch-Through Shear (PTS) test is used in order to investigate shear behavior in mode II conditions. The concept of this test is to first subject the specimen to a confining pressure and then an axial loading is applied to punch through the central portion of the core.

In order to introduce confinement to the concrete sample prior to testing it under shear, two methods have been used. The first one is an active confinement applied by means of a high capacity triaxial press Giga. The second method consists in confining the sample with a pre-stressed metallic cell instrumented with hoop strain gages in order to evaluate the confinement acting in the ligament of the concrete sample.
Samples confined with the pre-stressed cell are subjected to two types of loading; static and dynamic. The static tests are carried out by means of a normal hydraulic press while dynamic shear testing are performed using a modified Split Hopkinson Bar setup which allows to determine the shear response of concrete over a wide range of strain-rates.

The results of test campaigns show that the shear strength of the concrete increases significantly with an increase of confining pressure. Furthermore, dry and saturated concrete samples have been tested in order to study the influence of saturation ratio on the shear behavior of concrete. The results show a higher shear strength with dry samples than in wet ones. Moreover, a small influence (compared to what was observed in dynamic tension) of the strain rate was observed. A high performance concrete was also studied to investigate the influence of concrete composition on its shear strength. It was observed that its shear strength strongly exceeds that of the ordinary concrete. The obtained results are compared with data from literature obtained with different experimental methods.

Keywords: Mode II, High confinement, Pre-stressed cell, R30A7 concrete, High Performance Concrete, Saturation ratio,High strain-rate, Giga, Split-Hopkinson Pressure Bar

Résumé

L'objectif de cette thèse est de caractériser le comportement confiné en cisaillement du béton sous chargement statique et dynamique. La méthode expérimentale reprend le concept de l'essai 'Punch Through Shear' qui consiste dans un premier temps à soumettre une éprouvette de béton à un chargement radial puis à appliquer au cours d'une deuxième étape un chargement axial qui permet de cisailler la partie centrale de l'échantillon.

Deux méthodes ont été utilisées pour appliquer la contrainte de confinement à l'éprouvette avant de la soumettre à un chargement de cisaillement. La première méthode consiste à appliquer une pression hydrostatique via un fluide de confinement. Ces essais sont réalisés avec la presse Giga. La deuxième méthode consiste à utiliser une cellule métallique pré-déformée à l'aide d'une presse hydraulique. Durant le déchargement de la cellule, des contraintes de confinement sont transmises à l'éprouvette de béton. Cette cellule est instrumentée avec des jauges de déformation qui permettent de mesurer le niveau de confinement appliqué au béton.
Les éprouvettes de béton confinées avec la cellule sont soumises à deux types de chargement : l'un statique avec une presse hydraulique normale et l'autre dynamique avec un système aux barres de Hopkinson. Cela permet d'étudier le comportement du béton en cisaillement confiné sur une large gamme de vitesse de déformation.

Les résultats des campagnes d'essais montrent que la contrainte de cisaillement du béton augmente avec la pression de confinement. D'autre part, des échantillons saturés d'eau et d'autres séchés à l'étuve sont testés afin de vérifier l'influence de la teneur d'eau sur la résistance au cisaillement. Une résistance au cisaillement des échantillons de béton R30A7 sec supérieure à celle des échantillons saturés est observée sur la plage de déformation considérée. Une influence modeste de la vitesse de déformation en comparaison de ce qui est observé sous chargement en traction dynamique a été remarquée. De plus, un béton haute performance a été testé pour étudier l'influence de la composition du béton sur sa résistance au cisaillement. Il a été observé que la résistance au cisaillement du béton haute performance dépasse fortement celle du béton ordinaire. Les résultats obtenus sont comparés à ceux de la littérature, pour lesquels des méthodes expérimentales différentes avaient été utilisées.

Mots clés: Mode II, Fort confinement, Pré-confinement, Béton R30A7, Béton haute performance, Degré de saturation, vitesse de déformation élevée, Giga, Système aux barres de Hopkinson

Contents

INTRODUCTION

During their lifetime, concrete structures might be subjected to different types of loading that can be caused intentionally such as projectile or missile impacts or accidentally such as collisions and earthquakes. For example, when a concrete target is subjected to a projectile impact (Figure 1), several damage modes can be observed (Zukas [1992]). First, the penetration of the projectile into the front face of the target causes the development of a crater, it is the scabbing phenomenon (Forquin et al. [2008b]). The projectile then progresses into the target by subjecting the surrounding material to extreme pressure levels (tunneling phase) and by generating triaxial compression and shear stresses (Forquin et al. [2015b]). Radial cracking can often be seen on the front face and inside the target. Finally, when the projectile approaches the back face of the target, another crater known as 'spalling' is formed. These different stages happen in most ballistic tests carried out on concrete as function of several parameters such as the speed of the projectile and its geometry (Zhang et al. [2005], Hanchak et al. [1992]).

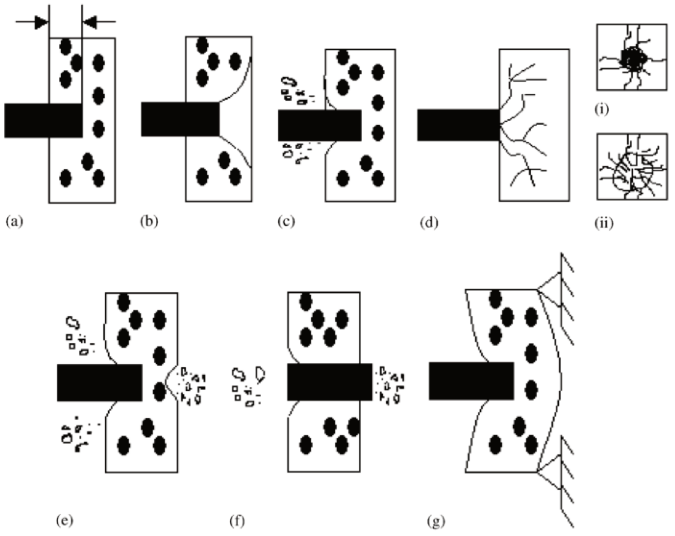

FIGURE 1: Missile impact effects on concrete target, (a) Penetration, (b) Cone cracking, (c) Spalling, (d) Cracks on (i) proximal face and (ii) distal face, (e) Scabbing, (f) Perforation, and (g) Overall target response. [Li et al. [2005]]

Since it is necessary to protect massive structures from these severe loadings, different studies have emerged to understand the behavior of concrete under extreme conditions. Experimental methods are necessary in order to better understand real phenomena and validate analytical solutions (Ravichandran [1995], Carol et al. [1997]) and numerical models (Pontiroli et al. [2010], Forquin and Hild [2010]).

Triaxial compression tests have been performed for several decades on concrete (Schmidt et al. [2009] and Warren et al. [2004]). The concrete specimen is subjected to a hydrostatic pressure in a first stage then an axial stress is applied. A transition from a brittle to a ductile behavior, which is a characteristic of cohesive materials, was observed. A study (Gabet et al. [2008]) on 'real concrete' specimens allowed applying a pressure up to 0.85 GPa and a maximum volumetric strain of about 12% was reached.

However, triaxial tests are difficult to perform under dynamic conditions because they require impermeability between the fluid and the specimen. Another method was used to characterize the confined behavior of concrete over a wide range of strain-rates: the quasi-oedometric compression test. This method was proposed by Bazant et al. [1986], Burlion [1997] and Gatuingt [1999] and fully revisited by Forquin et al. [2007] under static conditions and by Forquin et al. [2008c], Forquin et al. [2010] and Piotrowska and Forquin [2015] in dynamic (SHPB) testing conditions. A maximum pressure of 800 MPa was reached with a volumetric strain of 15 %.

Since shear fracturing in mode II was also observed in impact tests, it is important to understand the concrete behavior under such loading (Forquin et al. [2008c], Forquin et al. [2010] and Lukić and Forquin [2015]). The Punch through shear test is one of the techniques that exist in the literature to study the shear behavior of concrete in which high deformations are reached inside concrete sample. These tests were conducted on concrete with a low level of pressure (around 8 MPa) (Montenegro et al. [2007]) or on rocks with a hydrostatic pressure up to 70 MPa (Backers [2004]). Moreover, punch-through shear testing technique was developed and performed in static and dynamic conditions with a passive confining pressure which varies during the test (Forquin [2011b]) and constitutes a main drawback of the method.

In the present work, we are concerned in studying the confined shear behavior under low and high rates of loading, this behavior has not yet been completely studied despite being of a real concern during impact of concrete structures. The objective of the work is to complete the tests existing in the literature to investigate the behavior of concrete subjected to high confining pressures with high deformation levels and over a wide range of strain-rates.

For this purpose, two types of tests were developed. The first test is a triaxial punch-through shear test, it consists of applying in a first phase a hydrostatic pressure to a predetermined level, this pressure is maintained constant while the axial load increases at a constant loading rate before material failure in the second phase. The second test consists of confining the concrete sample with a pre-stressed metallic cell prior to applying the shear loading.The numerical simulations done for the design of each test will be described then the test procedures and the different results will be presented.

In the first chapter, a bibliographic study will be devoted to recapitulate the tests describing the behavior of concrete structures subjected to impact. Different experimental methods will be presented, the compression tests, the triaxial tests, the quasi-oedometric compression tests and the punching-through shear tests.

In chapter two, quasi static tests performed by applying a hydrostatic pressure and then a shearing to the concrete sample are presented. These tests are done with the press Giga in which the loading stamps were modified in order to be able to apply shearing to concrete samples. These tests will be performed on real concrete with the largest aggregates size of 8 mm.

In the third chapter, a new technique based on pre-stressing concrete samples with a metallic ring is presented. This ring is instrumented with hoop gages and is deformed elastically by applying a compressive load which is released after inserting the specimen. The ring applies a confinement to the sample while retrieving its initial position. After applying the confinement, a normal hydraulic press (Schenck) is used to perform static shear testing and a Split Hopkinson Pressure bar setup is used to perform dynamic testing. This study was performed on two different types of concrete, an ordinary concrete R30A7 and a high performance concrete (HPC). Also, two sets of R30A7 specimens have been studied, dry and wet samples. Wet samples are placed in water and dry specimens are oven dried at 60°C until their mass stabilization.

In the last chapter, final conclusions of this PhD work are drawn by comparing the results of this work to the ones that can be found in the literature. The perspectives raised by this work will be also proposed.

Chapter 1

State of the art

1.1 Experimental characterization of concrete

Concrete is the most used material in civil engineering due to its low cost and durability. It is widely used in structures such as bridges, dams, bunkers or nuclear power plants. When subjected to an impact, high mean stresses and high strain rates occur inside concrete targets. Adequate experimental techniques are generally used to understand the concrete mechanical response and model it as accurately as possible. In order to answer the problematic of the thesis, a state of the art of the existing experiments is presented in this chapter. The mechanical behavior of concrete will be presented for different loading path: simple compression, quasi-oedometric compression, triaxial and shear loading. Results for different moisture contents and concrete compositions over a wide range of strain-rates will be discussed.

1.2 Simple Compression tests under static and dynamic loading

Simple compression test is one of the classical tests done on concrete to measure its compressive strength, the main property of concrete. The test is conducted on cylindrical specimens aged of at least 28 days, the two surfaces of the sample are rectified to obtain two flat and parallel surfaces and avoid the frictional resistance in contact with the compression plates. The measurement of the axial strain of the sample can be obtained by means of different sensors: LVDT (Linear Variable Displacement Transducer), extensometers or strain gauges.

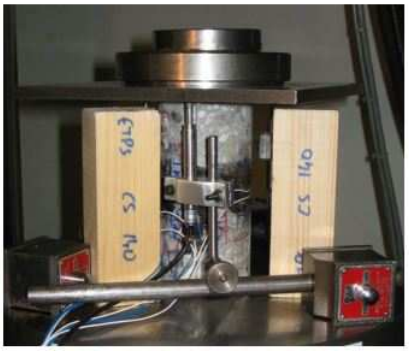

FIGURE 1.1: Instrumented sample ready to be tested under simple compression (Vu [2007]).

In order to study the dynamic behavior of concrete under uniaxial compression, the Split Hopkinson bar technique is used. The Hopkinson bar setup was first introduced by John and Bertram Hopkinson which measured pressure through induced-wave propagation in an elastic metal bar. Kolsky [1949] added another bar to this setup and put the specimen between the two bars, this new configuration is known as Kolsky bar or Split-Hopkinson pressure bar and is represented in Figure 1.2.

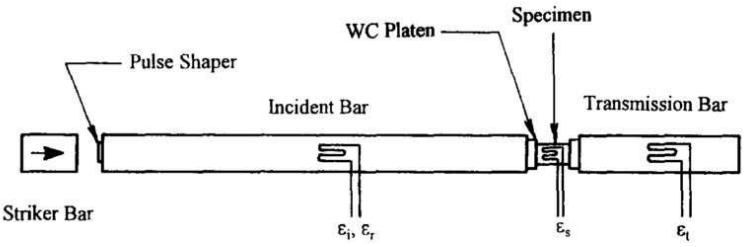

FIGURE 1.2: A schematic view of the Split-Hopkinson bar apparatus

This conventional Kolsky pressure bar consists of a striker bar, an incident bar and a transmission bar. The specimen is sandwiched between the incident and transmission bars. When the striker bar impacts the incident bar, an elastic compression pulse, called incident pulse, is generated and propagates along the incident bar and hits the specimen. A part of this pulse is reflected back in the bar and the remaining part is transmitted through the specimen into the transmitted bar. Strain-gauges, glued on the bars, allow the knowledge of forces and particle velocities at both faces of the specimen.

Bischoff and Perry [1995] gathered different tests done on concrete and found that there is an increase of the compressive strength at high strain rate (Figure 1.3). This relative increase might be produced because of two different modes: the first mode corresponds to a strain rate less than 10/s and can be explained by the presence of water in the pores of concrete which exhibits the so-called Stefan effect causing the strengthening in concrete (Toutlemonde [1994]). The second mode for which the strain rate is higher than 10/s is related, at least in part, to a structural effect. The inertia generates radial

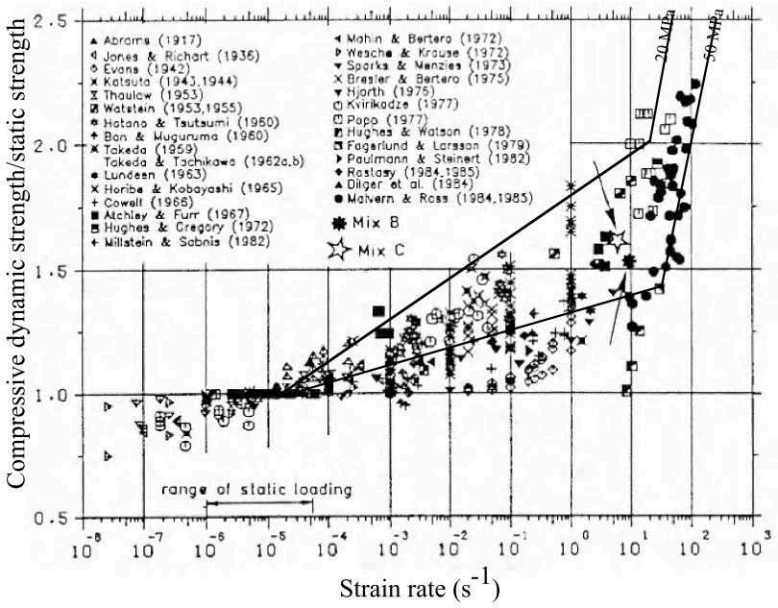

FIGURE 1.3: Compressive strength increase versus strain-rate (Bischoff and Perry [1995])

constraints which act like a confining pressure and thus increase concrete strength (Rossi [1991], Bailly [1994]).

1.3 Confined compression behavior of geomaterials

During impact problems, concrete is subjected to high confinement compressive stresses and is compacted mechanically (Burlion [1997] and Burlion et al. [2000]). During compaction process, there is a damage of the cementitious matrix and closing of the porosity accompanied by an irreversible decrease of the material volume and an evolution of the mechanical properties. In order to highlight the importance of lateral pressure on the behavior of concrete, several experimental techniques have been developed.

Triaxial tests have shown their interest to characterize the confined behavior of concrete in quasi-static loading but they can not be easily adapted to the characterization of concrete in dynamics. Another common characterization method, which uses a different loading path for studying the confined behavior of concrete, is the quasi-odometric test. Both tests will be presented hereafter.

1.3.1 Quasi-oedometric compression tests

The standard triaxial test does not closely simulate the conditions of concrete in structures designed to resist explosions during impact. In these structures, concrete is confined by heavy reinforcement in three directions, which causes the lateral normal stresses to increase along with the axial stress. The behavior of concrete in these structures is better simulated by confined compression tests (Bazant et al. [1986]). Therefore, the strength of concrete can be thought to be pressure dependent and strain independent as a first approximation. This assumption is necessary to deduce the confined behavior of concrete materials from a single quasi-oedometric compression test (Forquin et al. [2007]).

1.3.1.1 Static tests

Bazant et al. [1986] carried out confined compression tests on specimens of hardened Portland cement paste and mortar. Samples were tightly fit into a cylindrical cavity in a pressure vessel which prevents lateral deformation and then loaded axially by a hard piston. A significant improvement of the test was obtained by considering a steel cell which allows the application of pressure of several hundreds of MPa in one hand and measuring the confinement pressure in the other hand (Burlion [1997] and Burlion et al. [2001]). Figure 1.4 shows a description of the apparatus.

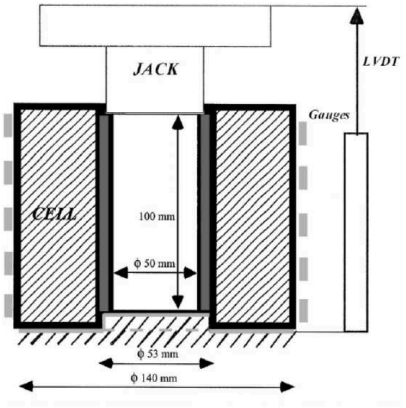

FIGURE 1.4: Uniaxial confined compression apparatus (Burlion et al. [2001])

The pressure applied by concrete on the inner part of the steel tube was supposed uniform and was obtained by the measurement of the transverse strains on the external face of the cell assumed to be elastic. The gap between the specimen and the cell is filled with epoxy chrysor C6120 and a Teflon coating is applied on the inner surface of the specimen in order to minimize friction and ensure a correction of any possible defects of cylindricality, parallelism and coaxiality of the surfaces of the specimen. Several

assumptions were made: the interface product is incompressible and the friction between specimen and steel is negligible. A pressure of 600 MPa has been reached on concrete samples of 50 mm diameter and 100 mm height. Tests on mortar with different W/C ratio were done and they showed that the higher the porosity, the larger the irreversible volumetric strain which represents the compaction process. The author also compared the results of quasi oedometric compression tests with true hydrostatic tests on mortar specimens (W/C=0.5), a much lower compaction process is observed in this case and it was concluded that the hydrostatic response of the mortar depends on the applied deviatoric stresses (Figure 1.5).

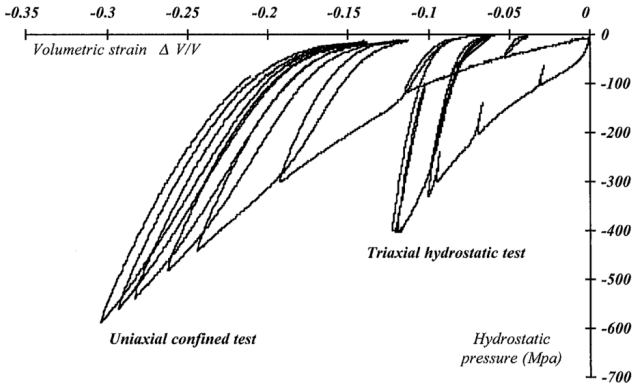

FIGURE 1.5: Experimental hydrostatic and oedometric tests results on mortar (W/C=0.5) (Burlion et al. [2001])

The axial contraction of the specimen and the barrel deformation of the vessel were not taken into account in the analysis of Burlion et al. [2001]. Forquin [2003] made an improvement on the measurement technique and took into consideration these two subjects. He considered a relationship between the orthoradial deformations and the internal pressure taking into account that the confining pressure is not distributed over the entire height of the cell but on a portion that corresponds to the height of the specimen. A new processing method was introduced to make possible the use of a confining cell that deforms with non-purely elastic (elasto-plastic) behavior. A validation of the testing procedure was done experimentally and numerically on aluminum (Forquin et al. [2007]) and applied to different concrete microstructures (Forquin et al. [2008a]). More detailed results will be presented in the following paragraph.

1.3.1.2 Dynamic tests

Gatuingt [1999] made static and dynamic confined test on samples of micro-concrete MB50 of 50 mm height and 30 mm or 50 mm internal diameter. The geometry of these tests is presented in Figure 1.6.

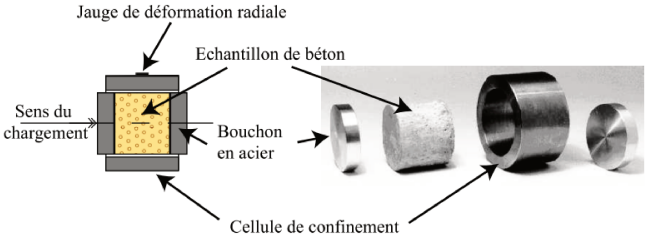

FIGURE 1.6: Geometry of quasi-oedometric tests (Gatuingt [1999])

Tests with different loading rates from 100 to 400/s showed a strong hardening of the material followed by a saturation of the axial stress at 870 MPa. These dynamic tests showed a small influence on the dynamic response (Figure 1.7) which is in contradiction with the big influence of strain rate in dynamic uniaxial compression tests (cf. Figure 1.3). The radial confinement appears to reduce the effect of the radial inertia of the material observed during uniaxial tests.

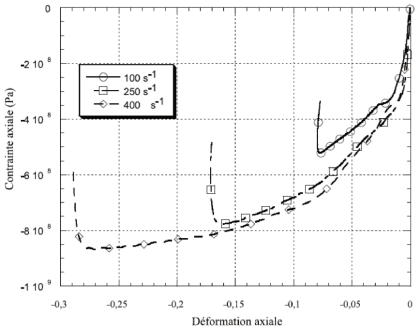

FIGURE 1.7: Stresses versus deformations for QOC dynamic tests (Gatuingt [1999])

The methodology developed by Forquin [2003] in quasi-static conditions was applied to dynamic quasi-oedometric compression tests using a split-Hopkinson Pressure Bar device (Forquin et al. [2008c]). The loading cell instrumentation is shown in Figure 1.8. Specimens have a diameter varying from 28.8 to 28.9 mm and are 40 mm long. The hydrostatic and deviatoric behavior obtained for different strain-rates are shown in Figure 1.9.

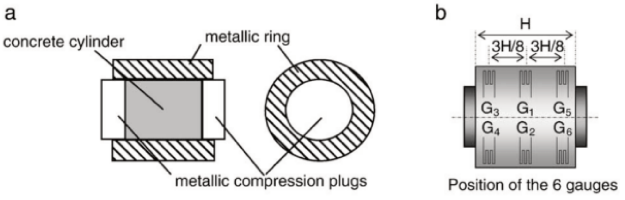

FIGURE 1.8: Loading cell used for quasi-oedometric tests (Forquin et al. [2008c])

The results obtained for different strain-rates are close to each other which justifies the conclusion obtained by Gatuingt [1999] that the behavior of concrete is weakly influenced by the strain-rate.

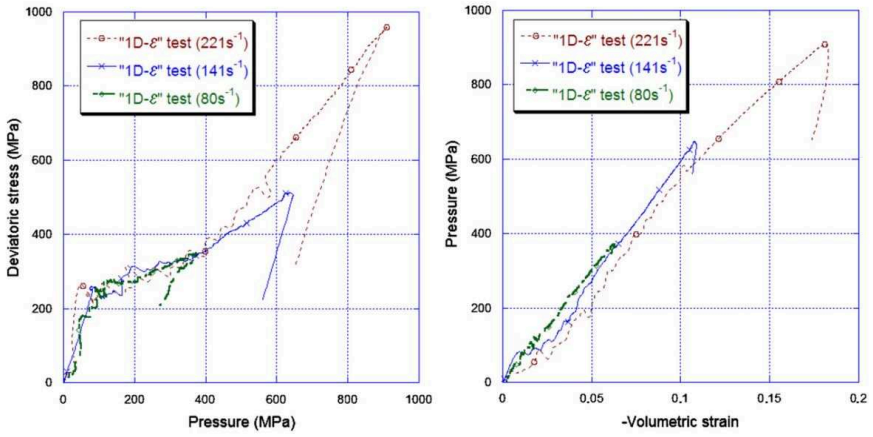

FIGURE 1.9: Deviatoric and hydrostatic behavior of MB50 concrete conducted by (Forquin et al. [2008c]) at different strain-rates

Forquin et al. [2015a] conducted quasi-oedometric tests on R30A7 concrete and they considered 4 levels of saturation ratio: dry, 60%, 80% and 100%. The specimen is 40 mm in diameter and 40 mm long. In the study, static tests were done with the GIGA press which was used as a standard hydraulic press and dynamic tests with split Hopkinson pressure bars.

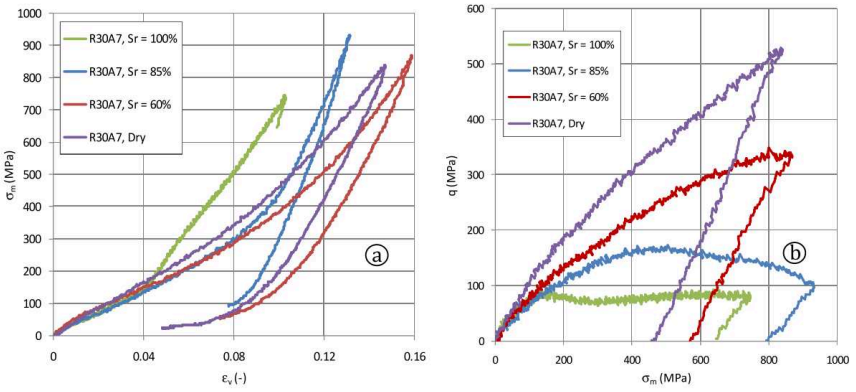

FIGURE 1.10: Quasi-static tests performed on R30A7 concrete (a) Compaction curve (b) Deviatoric behavior (Forquin et al. [2015a])

It was noticed that for a given pressure, the level of compaction is greater for dried specimens. Moreover, one can clearly see on Figure 1.10 that the deviatoric stress of dry concrete keeps increasing with the increase of pressure while wet concrete has a limited strength even under high hydrostatic pressure. An increase of pore-pressure in the micro-structure is the cause of the limited strength in saturated samples according to tests and results obtained with micro-concrete MB50 (Forquin et al. [2010]). Similar behavior was seen for dynamic tests (Figure 1.11). A concentration of deviatoric stress

was observed for saturated concrete which also has a stiffer hydrostatic response. It was concluded that the saturation ratio has a big influence on the response of the concrete R30A7 while the strain rate has a limited (but non-zero) influence on its response.

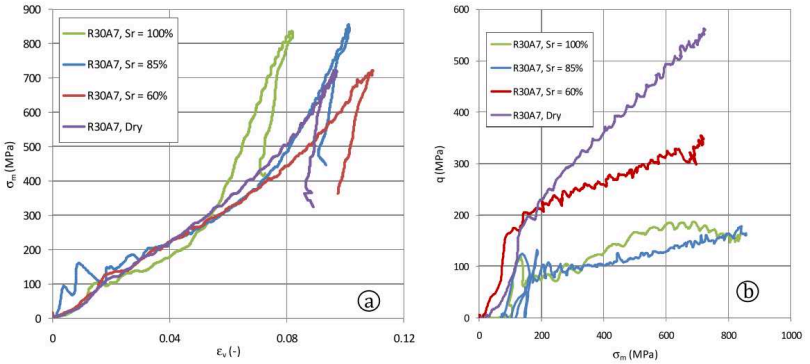

FIGURE 1.11: Dynamic quasi-oedometric experiments on R30A7 concrete (a) volumetric behavior (b) deviatoric behavior (Forquin et al. [2015a])

The same testing technique was conducted on high strength concrete (fc28=80 MPa) (Piotrowska and Forquin [2015]) and compared to ordinary one. In both static and dynamic conditions, dry specimens of the two concretes reach approximately same deviatoric stress while for saturated specimens, the deviatoric stress is much greater in high strength concrete (Figure 1.12 and Figure 1.13).

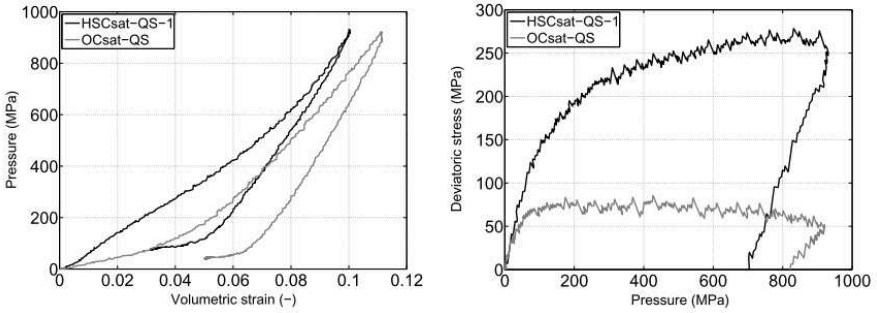

FIGURE 1.12: Comparison of the behaviors of high strength concrete HSC and ordinary concrete OC under static quasi-oedometric compression for saturated samples (Piotrowska and Forquin [2015])

Because of the low porosity of the high strength concrete, this latter shows a stiffer volumetric behavior. Same conclusion than with the ordinary concrete was deduced for the high strength concrete; their behavior is strongly dependent on the water content and weakly dependent on the strain rate.

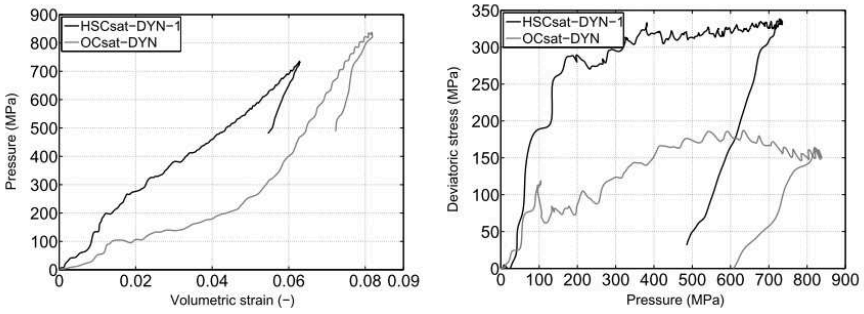

FIGURE 1.13: Comparison of the behaviors of high strength concrete HSC and ordinary concrete OC under dynamic quasi-oedometric compression for saturated samples (Piotrowska and Forquin [2015])

1.3.2 Triaxial tests

1.3.2.1 Static tests

Triaxial loading with a moderate level of confining pressure have been addressed by many authors (Warren et al. [2004], Sfer et al. [2002], Williams et al. [2006] and Schmidt et al. [2009]). These authors have revealed the increase of concrete strength and a transition from brittle to ductile behavior with the confinement (Figure 1.14).

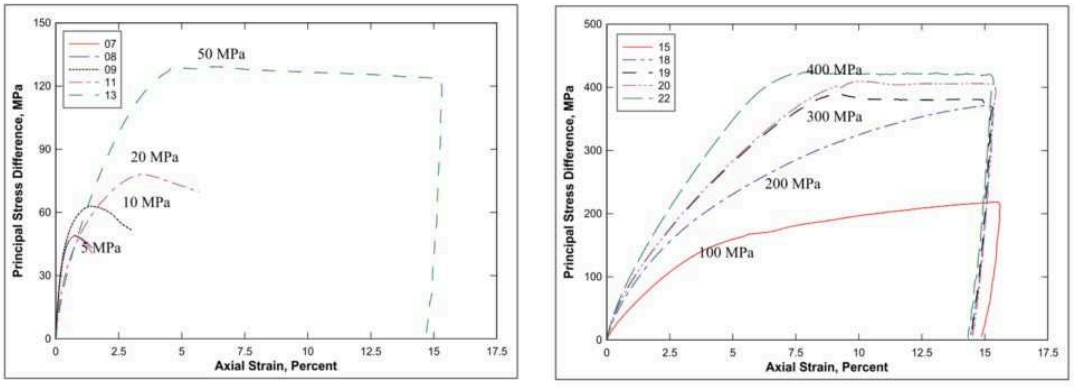

FIGURE 1.14: Deviatoric behavior for triaxials tests done on SAM-35 concrete (Porosity=20%, Sr=40%) for confining pressures going from 5 MPa to 400 MPa (Williams et al. [2006])

Gabet et al. [2008] performed hydrostatic, triaxial and oedometric tests with the Giga press testing apparatus (described in Chapter 2). Levels of confinement of the order of the GigaPascal, axial stress of 1.6 GPa and volumetric strains of 12% have been reached during these tests. The results have revealed an influence of the loading path on the compaction behavior which confirms previous studies carried out on mortar specimens (Warren et al. [2004] and Schmidt et al. [2009]) and it has also been proved that the deviatoric stress, associated to shear stress increases the compaction process (Burlion et al. [2001]). In other words, for a given mean stress, the higher the deviatoric stress, the

more compacted the specimen. This sensitivity to the deviatoric stress can be explained by a granular rearrangement inside the matrix under shear stress.

Influence of saturation ratio

Vu [2007] carried out experiments about the effect of the saturation ratio on the concrete behavior under high confinement. The test results show that the saturation degree has a major influence on the concrete behavior. The behavior of an ordinary concrete is only slightly dependent on the saturation ratio at low confining pressures while under high mean stress, the hydrostatic behavior of very wet or saturated concrete clearly become stiffer than that of dried concrete. The curves of the deviatoric behavior show that the strength of dried concrete strongly increases with the confining pressure whereas it is limited for saturated samples (Figure 1.15).

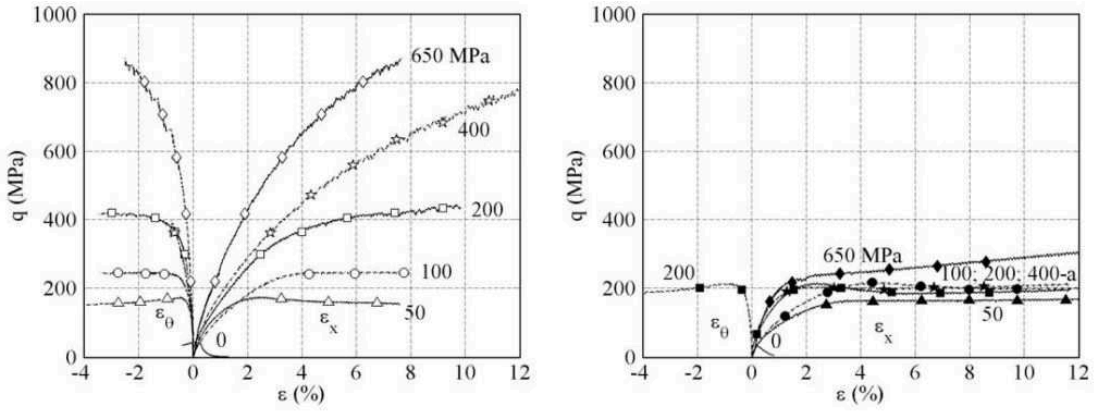

FIGURE 1.15: Effect of saturation ratio on the deviatoric behavior of concrete subjected to different level of confining pressure (a) Dried concrete Sr=11% (b) Saturated concrete Sr=100% (Vu et al. [2009a])

Regarding the limit states, it is found that at a low level of mean stress (below 150 MPa), the states of the dried, wet and saturated samples all lie very close to one another (Figure 1.16) since at such stress levels, concrete behavior is governed by a cohesive character. The presence of water in the sample does not exert therefore a very significant effect on the limit state.

Conversely, it was shown that for higher confinement levels, the effect of water becomes predominant. The increase in peak deviatoric stress with respect to mean stress remains very low for the saturated samples; this phenomenon may be explained by a pore pressure effect. These observations can be explained by a combination of two phenomena. On the one hand, the loss of cohesion in the cementitious matrix due to high confinement makes the concrete a non-cohesive granular material type (Vu et al. [2009a]). The dried concrete shear strength increases nearly linearly with confining pressure, and this

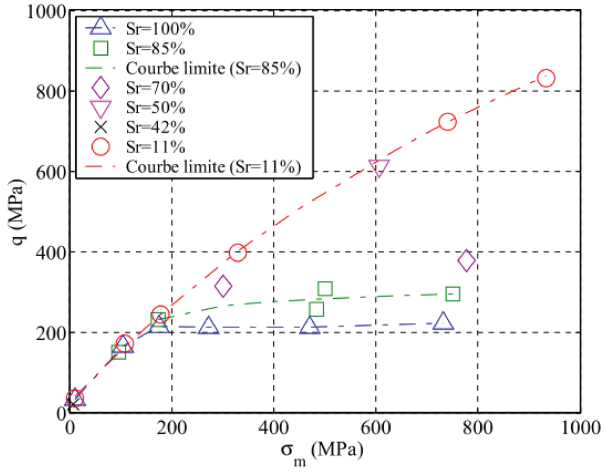

FIGURE 1.16: Limit states of the dry and saturated concrete in the stress invariant space (Vu et al. [2009a])

is explained by the friction existing between stacking grains. On the other hand, the high level of volumetric strains in comparison with the sample initial air volume serves to trend sample humidity closer to saturation. The pore pressure developing in the material becomes sizable and increases the volumetric stiffness of the concrete while limiting its shear strength.

Influence of matrix porosity

Zingg [2013] and Zingg et al. [2016] studied the influence of cement matrix porosity on the behavior of concrete. He conducted tests on concrete samples with different porosity values (high performance concrete HPC and low performance concrete LPC) and compared them with the ordinary concrete OC. The evolution of the tangent volumetric stiffness versus the means stress for the three types of concrete is presented in Figure 1.17.

Figure 1.17 shows that the same behavior occurs with the three types of concrete: the curve is characterized by a linear constant part then by a fast decrease of stiffness due to the damage of cement matrix and afterwards a slight increase of the volumetric stiffness happens due to the compaction process.

For low mean stress level, the limit state of the concrete is highly dependent on porosity: the resistance and stiffness are less important for a more porous concrete. For high confinement, the behavior of concrete becomes similar because the porosity of each sample is closed by the compaction process and the cement matrix behaves like a granular stacking independently from its initial strength.

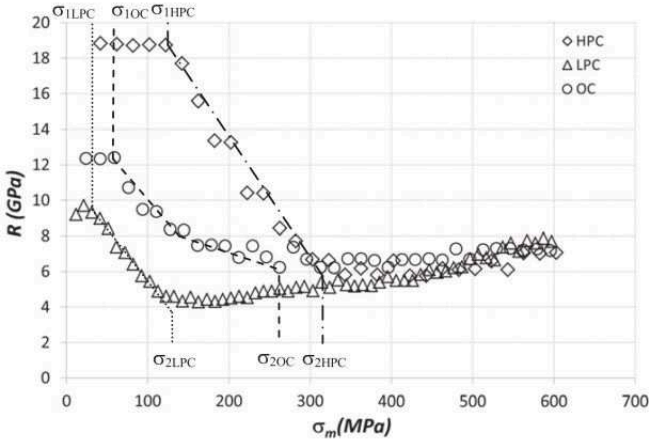

FIGURE 1.17: Evolution in volumetric stiffness vs.mean stress during hydrostatic loading (Zingg et al. [2016])

1.3.2.2 Dynamic tests

Martin et al. [2013] used a modified Kolsky bar to conduct dynamic triaxial compression experiments on a dry sand. A high pressure hydraulic confining cell is introduced to impose a confining pressure up to 400 MPa (Figure 1.18) prior to dynamic loading. Different density, confining pressure and strain-rate were investigated. They concluded that the pressure has a high influence on the response of the sand studied, the strain-rate has a limited influence and same response was obtained regardless its initial density.

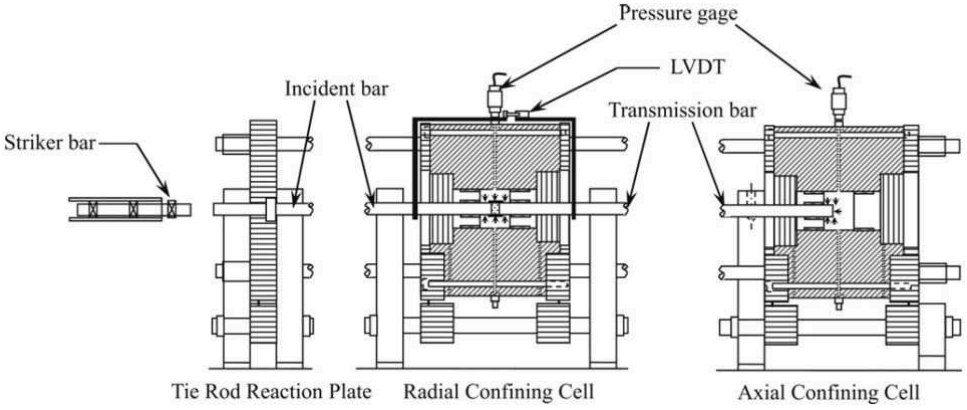

FIGURE 1.18: Schematic view of the confined Kolsky bar set-up used in triaxial experiments done by Martin et al. [2013]

1.4 Shear Behavior of geomaterials

In fracture mechanics, cracks or fractures are usually subdivided into three basic propagation modes: namely mode I (opening), mode II (sliding), and mode III(tiring) (Irwin

[1958]). All loading combination can be described by the superposition of these basic modes.

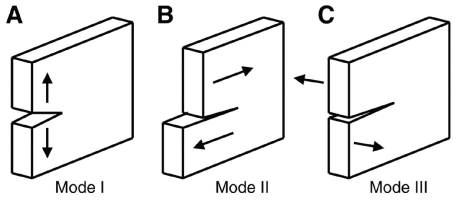

FIGURE 1.19: Illustration of the different fracture modes

In mode I, the crack tip is subjected to a displacement perpendicular to the crack plane, it occurs mainly when concrete is subjected to a tensile test. In mode II, the crack surfaces slide relative to each other and the crack surface displacements are in the crack plane and perpendicular to the crack front. Mode III fractures occur when a shear stress acts parallel to the plane of the crack and parallel to the crack front (Figure 1.19).

The understanding of tensile cracking in cementetious material has improved rapidly in the last decades however the cracking process under mixed mode loading has not been fully understood. Some of the existing methods elaborated to study mode II crack propagation are introduced hereafter.

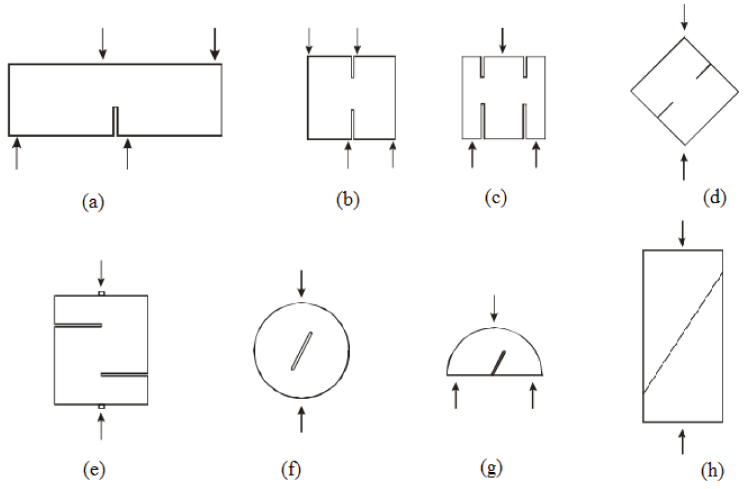

FIGURE 1.20: Mode II fracture toughness testing methods. (a) Antisymmetric Four-Point Bending, (b) Anti-symmetric Four-Point Bending Cube, (c) Punch through Shear, (d) Compression-Shear Cube, (e) Short Beam Compression, (f) Centrally cracked Brazilian test, (g) Three point bending semi-disk and (h) Triaxial Compression. [Backers [2004]]

The anti-symmetric four bending test (a, b) in Figure 1.20, introduced by Ingraffea [1981] was used for both mixed Mode I-II and Mode II loading and then tested by Barr and Derradj [1990] but was not able to avoid tensile stresses. Watkins [1983] was the first to introduce Punch through Shear test (c) which was done on cubic samples. This type of test has been developed by many authors and will be the subject of the following

work. Compression-Shear Cube tests (d) were performed by Rao [1999] to investigate the influence of confining pressure on the stress intensity factor in mode II (KIIC) of marble and granite. The author observed a linear increase of KIIC with the confining level. The Short Beam Compression test (e) with two notches orientated perpendicular to the loading direction was developed by Watkins and Liu [1985]. The centrally cracked Brazilian test (f) and three-point bending semi disk were used with an inclined notch but was not practical since results showed a mixed mode conditions. Rice [1980] and Hakami and Stephansson [1990] introduced the triaxial compression test (h) and they found that the fracture toughness is influenced by the pressure.

1.4.1 Punch-Through Shear Test concept

The punch through shear test that maximizes mode II conditions of crack propagation was first proposed by Watkins [1983] and then conducted by many authors (Luong [1990], Backers [2004] , Montenegro et al. [2007], and Forquin [2011b]).

It consists of short cylinders with cylindrical notches on top and bottom faces leaving a cylindrical ligament. Watkins [1983] used a cubic geometry and finite element analysis in order to calculate the fracture toughness KII. Experiments were made on soil-cement sample compacted by hand in 100x100 mm standard concrete molds. The load displacement curve is shown in Figure 1.21(b), it is observed that during the elastic phase, a sub-critical tensile crack was initiated and the vertical mode II fracture was formed at the peak.

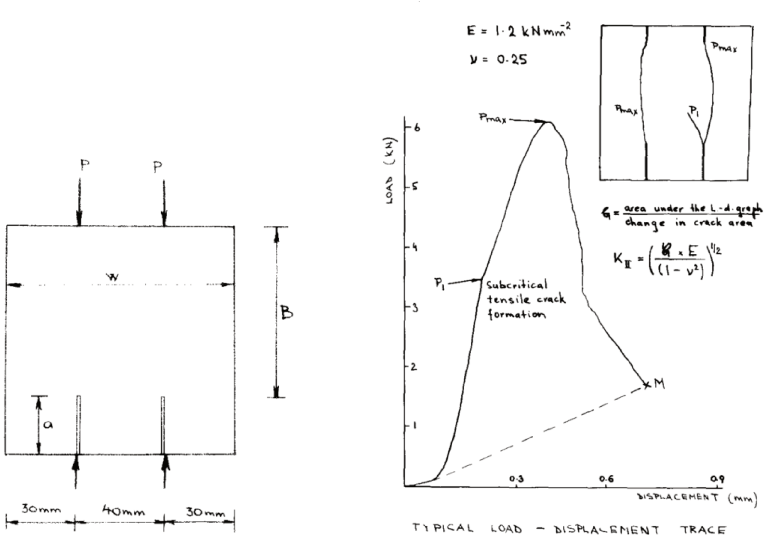

(a) (b)

FIGURE 1.21: (a) Geometry of the Punch-Through Shear test done by Watkins (b) A typical Load displacement curve obtained from experiments (Watkins [1983])

Luong [1990] and Luong [1992] has developed a technique to maximize mode II conditions of crack propagation in rocks. A circular tube is subjected on its internal and external faces to a shear stress parallel to Z axis. To avoid normal stresses induced by sliding on the facets (Reynolds dilatancy effect), four concentric tubular parts were made in the sample as shown in Figure 1.22

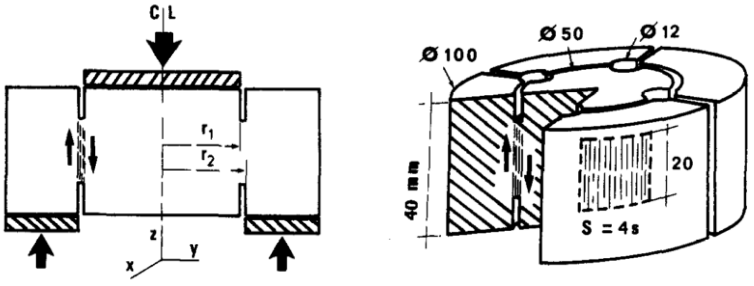

(a) (b)

FIGURE 1.22: (a) Geometry of the shearing zone of the direct shear test specimen, (b) Optimized dimensions of the proposed test (Luong [1992])

1.4.2 Triaxial Punch-Through Shear Test

In order to suppress the dilatancy in concrete and to avoid a tensile Mode I fracturing of the sample, some authors applied a confining pressure to the sample prior to shear loading. Backers et al. [2002] and Backers et al. [2004] conducted laboratory tests and finite element modeling on six different types of rock subjected to up to 70 MPa of confining pressure to measure Mode II fracture toughness. The specimen was first subjected to a hydrostatic pressure and then an axial load was applied to create shear stresses in the ligament. They concluded that fracture toughness increases with confining pressure and reaches a constant value at confining pressures higher than 20-35 MPa. The results of two types of rocks are presented in Figure 1.23.

The authors deduced that with the increase of shear stress, primary macroscopic wing fractures develop at about 30% of the maximum stress. They propagate out of the stressed zone and stop. Further elevation of shear stress in limestone results in development of an 'echelon fracture' with an angle depending on the confining pressure. This echelon fracture forms an almost straight fracture (mode II) at the peak of loading. Marble and granite show a somewhat similar fracture sequence, the energy requirement for the formation of the two types of fractures is different.

Montenegro et al. [2007] and Montenegro et al. [2013b] used the same method and evaluated the fracture energy associated to mode II fracture in confined and unconfined

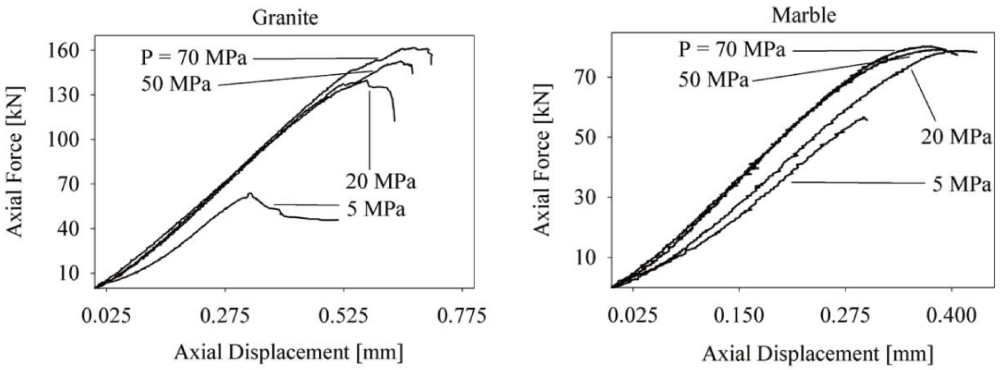

(a) (b)

FIGURE 1.23: Influence of confining pressure on the stress intensity factor for two types of rocks (a) Carrara Marble (b) Aue Granite (Backers et al. [2002])

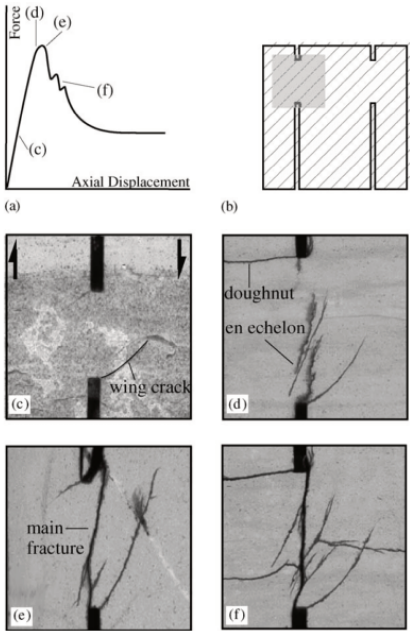

FIGURE 1.24: Fracture evaluation in limestone at different stages of loading for a confining pressure of 5MPa (Backers et al. [2002])

conditions. The specimens employed are similar to those proposed by Bakers and consist of short cylinders with coaxial cylindrical notches on top and bottom faces which leaves a cylindrical ligament. In the developed setup, this specimen is introduced in a large-capacity triaxial cell, protected with membranes and subjected to different levels of confining pressure prior to vertical loading. Measurements include vertical as well as circumferential displacements. The top and bottom drills have slightly different diameters, so that, given their finite thickness, the fracture surface going from outer side of top notch to inner side of bottom notch, remains as vertical as possible.

A higher peak load was observed for a confined test (2 MPa) done on a conventional

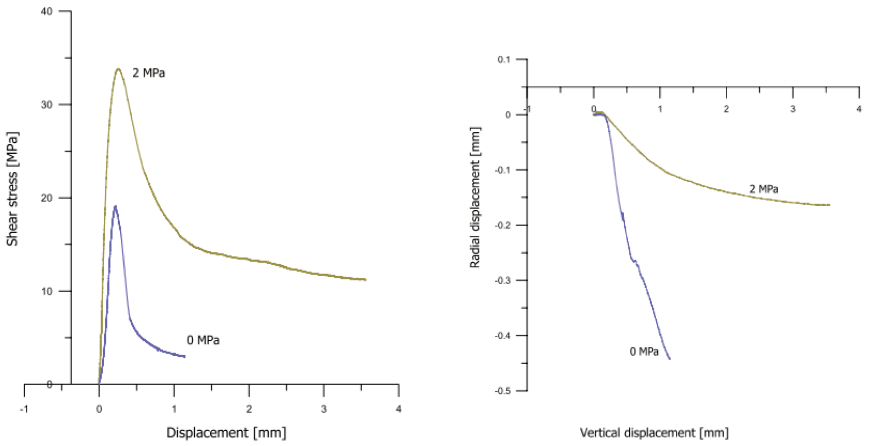

(a) (b)

FIGURE 1.25: Shear stress and radial displacement obtained for unconfined and confined tests (Montenegro et al. [2007])

concrete with a maximum aggregate size of 10 mm (Figure 1.25). After the peak, a steep descending branch followed by a gentle slope branch was observed. It was associated to two types of cracking, a vertical cracking between the notches followed by the opening of tensile radial cracks. It was concluded that shear strength and ductility are increased with lateral confinement and that dilatancy is reduced with high confinement.

1.4.3 Punch-Through Shear Test with passive confinement

Forquin [2011a] developed a new technique where a passive confining cell is used to apply confinement to the specimen (Figure 1.26). The same technique was used in quasi-oedometric compression tests (Forquin et al. [2007], Forquin et al. [2008b]) and samples were tested over a wide range of strain rate.

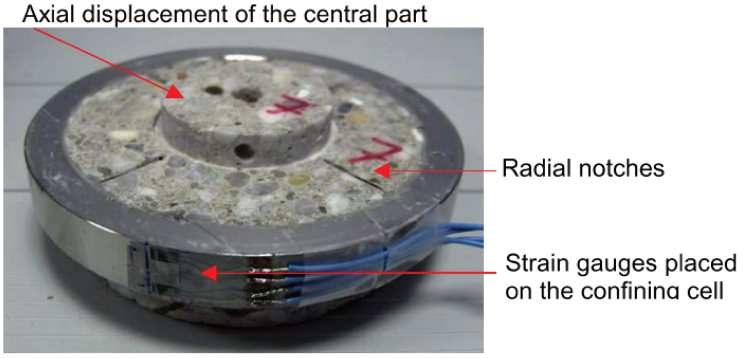

FIGURE 1.26: Concrete sample confined in a metallic ring and subjected to punch-through shear tes (Forquin [2011a])

1.4.3.1 Static tests

Forquin [2011b] conducted experiments on dry and saturated concrete samples with different stiffnesses of passive confinement cells and with circular notches to avoid self-confinement of the sample. Since steel is stiffer than aluminum, higher confinement was obtained in the concrete sample an thus higher shear strength was observed (Figure 1.27). Moreover, the author observed higher strength with dry samples than with wet ones (Figure 1.28).

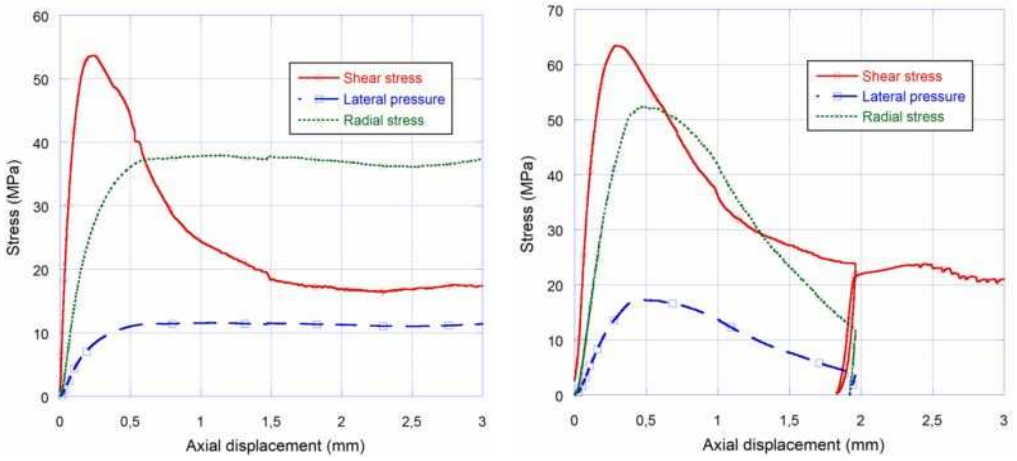

FIGURE 1.27: Quasi-static tests done on dry specimens with (a) aluminum and (b) steel confining cells (Forquin [2011b])

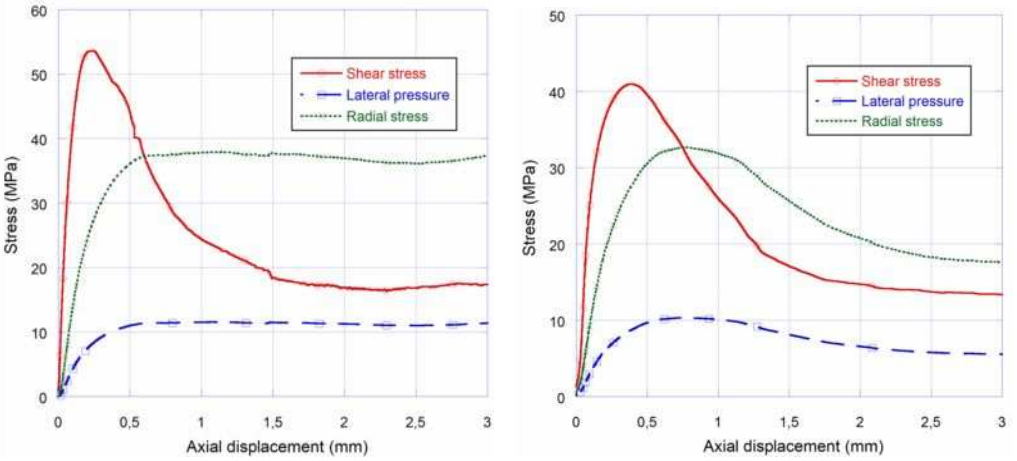

FIGURE 1.28: Quasi-static tests done on (a) dry and (b) wet specimens (Forquin [2011b])

1.4.3.2 Dynamic tests

Forquin and Sallier [2013] also studied the behavior of concrete at high strain rates using a Split Hopkinson Pressure Bar device and concluded that both sets of concrete (dry and wet) are weakly sensitive to strain rates up to 100/s (Figure 1.29).

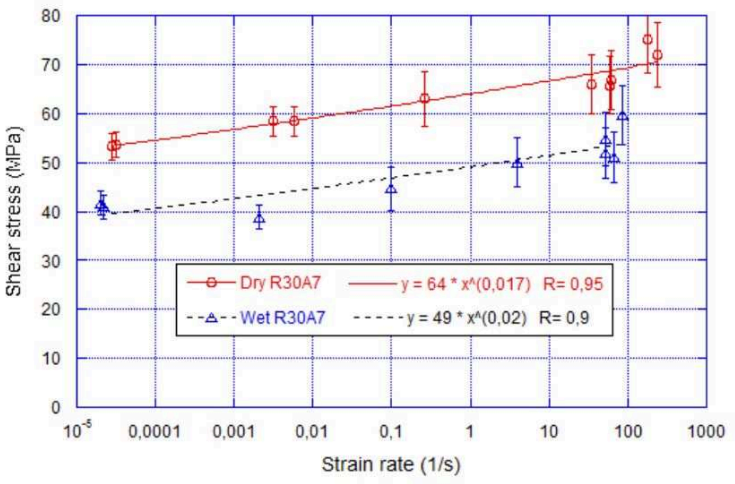

FIGURE 1.29: Quasi-static and dynamic tests performed on dry and wet concrete for different strain-rate, (Forquin [2011a])

More recently, Lukić and Forquin [2015] used the same technique to study the shear behavior of Ultra-High Performance Concrete with and without steel fibers under static and dynamic conditions. Four or eight radial notches were performed on the sample to suppress its self confinement and thus deduce radial stresses inside the ligament. They discovered a decrease of shear strength for a higher number of radial notches for both static and dynamic tests. They also obtained higher shear strength of about factor two in dynamic tests in comparison to static ones for Ultra-High Performance Concrete and Fibered Ultra-High Performance Concrete. Moreover, a higher shear strength was obtained for Fibered UHPC (Figure 1.30).

By comparing shear stress as a function of radial stress (Figure 1.31), it was deduced that at high strain-rates the increase of shear strength results from a higher radial stress. The authors stated that this difference of shear strength might be induced by the adjournment of tensile fracturing and an alteration of crack propagation prior to mode II cracking.

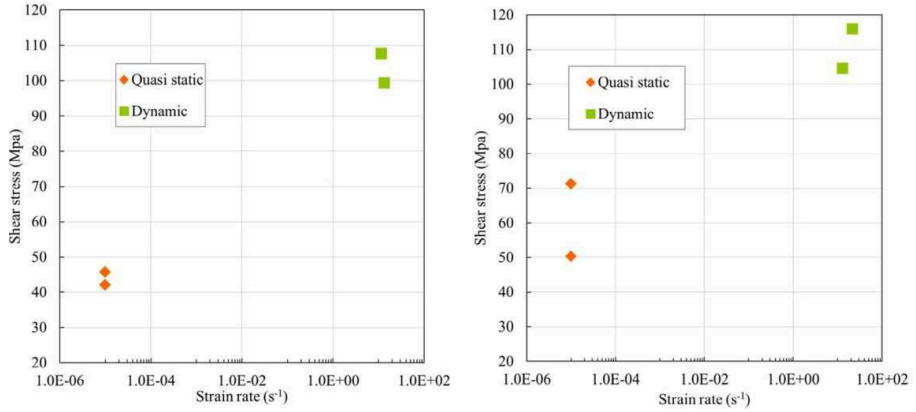

FIGURE 1.30: Shear stress Vs Radial stress of quasi-static and dynamic tests done on (a) Ultra-High Performance Concrete and (b) Fibered Ultra-High Performance Concrete (Lukić and Forquin [2015])

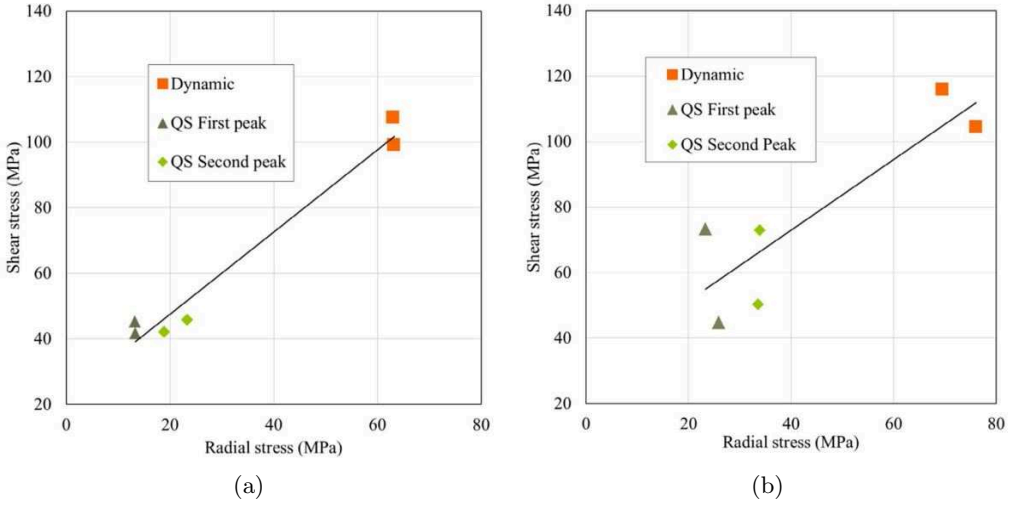

FIGURE 1.31: Shear stress Vs Strain-rate for (a) Ultra-High preformance concrete (b) Fibered Ultra-High performance concrete (Lukić and Forquin [2015])

The split Hopkinson pressure bar technique was also used to study dynamic shear failure of different materials such as rocks, steel or polymers. Yao et al. [2017] used the same geometry suggested by Backers and Stephansson [2012] to determine the dynamic fracture toughness of Fangshan marble and concluded that it increases with the loading rate (Figure 1.32). They also used the micro CT to analyze fracture pattern and modes and noticed that the main fracture developed at peak force is the mode II fracture.

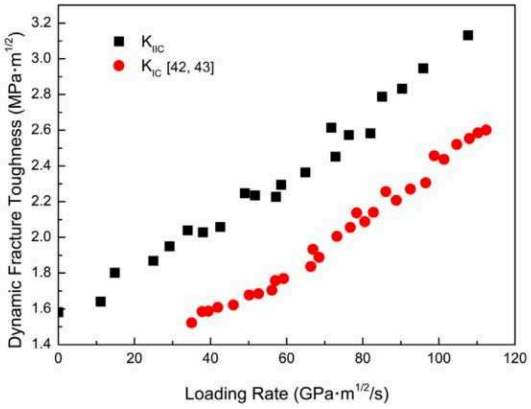

FIGURE 1.32: Mode I and Mode II fracture toughness for Fangshan marble at different levels of strain-rate (Yao et al. [2017])

1.5 Conclusion

Several experimental tests exist in the literature to improve the understanding and modeling of the confined and shear behavior of geomaterials subjected to impact as presented in the bibliographic review. Table 1.1 summarizes most of these tests.

Compression tests on concrete showed the strong influence of strain-rate that mainly results from structural effect observed in dynamic tests. Results through triaxial and quasi-oedometric compression tests showed the important influence of confinement on the deviatoric strength of concrete. The confinement applied was up to 850 MPa and the axial and volumetric deformations reach often a value around 15%. The strength of dried concrete increases with confinement but stays constant under a certain level of confinement for saturated sample. Thus, the presence of water plays a big role on the confined behavior of concrete.

Concrete shear analysis showed the importance of confinement in increasing its strength and reducing the dilatancy effect. Experiments conducted on dry and saturated concrete samples showed a higher strength with dry samples than in wet ones. Furthermore, both concrete showed a very small strain-rate sensitivity.

In previous punching-through shear test, the confinement applied is either quite small in the order of 4 MPa in Montenegro et al. [2007]'s study or applied to rocks characterized by a higher strength than concrete (Backers et al. [2002]) or applied using a passive confinement pressure (Forquin [2011b]). The values of the nominal deformation of the punch-through shear (PTS) tests in Table 1.1 were estimated from the axial displacement applied to the specimen during shearing.

Authors, Year	Type of test	Material tested	Confining Pressure (MPa)	Strain (%)	Strain rate (/s)
Burlion, 1997	Hydrostatic	Mortar E/C=0.5	400	12	Quasi-static
Buzaud, 1998	Hydrostatic	MB50	1500	10	Quasi-static
Schmidt, 2003	Hydrostatic	Concrete WES5000	500	18	Quasi-static
Buzaud, 1998	Triaxial	MB50	800	13	Quasi-static
William et al, 2005	Triaxial	Mortar FCAM	400	15	Quasi-static
Schmidt, 2003	Triaxial	Concrete WES5000	450	11	Quasi-static
Warren et al, 2004	Triaxial	Concrete 23 MPa	400	14	Quasi-static
Ackers et al, 2004	Triaxial	Concrete SAM-21	300	15	Quasi-static
Gabet, 2006	Triaxial	Concrete R30A7	650	10	Quasi-static
Burlion, 2001	QCO	Mortar E/C=0.5	600	30	Quasi-static
Gabet, 2006	QCO	Concrete R30A7	750	12	Quasi-static
Gatuingt, 1999	QCO	MB50	500	13	Quasi-static
Gatuingt, 1999	QCO	MB50	500	6	Dynamic (400/s)
Forquin, 2003	QCO	MB50	800	15	Quasi-static
Forquin et al, 2008	QCO	MB50	900	18	Dynamic (221/s)
Forquin et al, 2015	QCO	Concrete R30A7	850	14	Quasi-static
Forquin et al, 2015	QCO	Concrete R30A7	700	10	Dynamic (100/s)
Backers et al, 2002	Triaxial PTS	Granite	70	25	Quasi-static
Montenegro et al, 2013	Triaxial PTS	Concrete 49 MPa	8	5	Quasi-static
Forquin, 2013	Passive PTS	Concrete R30A7	12	3	Quasi-static
Forquin, 2013	Passive PTS	Concrete R30A7	18	6	Dynamic (60/s)

Volumetric Deformation
Axial Deformation
Estimated nominal deformation

TABLE 1.1: Summary of different tests existing in the literature for the experimental characterization of geomaterials

The aim of the present study is to perform punch-through shear tests with high levels of confinement over a wide range of strain-rates. Thus, the confined static and dynamic behavior of concrete will be investigated using a high capacity triaxial press or a pre-stressed metallic ring which allow having an almost constant confinement stress during shearing. The study includes R30A7 concrete in its dry and saturated states since it appeared that the saturation ratio plays a major role in the response of concrete. It also includes tests on high performance concrete to investigate the effect of the concrete composition on the shear behavior of concrete.

Chapter 2

Quasi-static Punching Through Shear test under high confinement

In this chapter, punch-through shear tests with high level of confinement are presented for the investigation of shear behavior of concrete. It was shown in the existing literature (Montenegro et al. [2013b], Backers et al. [2004]) that confining pressure suppresses the growth of tensile mode I cracks, consequently it is neccesary to apply a sufficient high level of confinement to limit mode I and obtain a pure mode II fracturing. In the present work, PTS tests have been conducted with a high-capacity triaxial press able to generate a high confining pressure. The test consists of cylindrical samples with two cylindrical notches in the top and bottom faces, the outer diameter of the top notch and the inner diameter of the bottom notch coincide to form a cylindrical shear ligament. In a first step, the concrete sample is subjected to a hydraulic pressure. Then in a second step, an axial load is applied to the central part of the specimen to produce shearing in the ligament.

Firstly, the hydraulic press used for the tests is introduced. New tools are designed to make the press able to apply shearing to the tested samples. Thus, numerical simulations done with FEM code (Abaqus) to study the influence of different geometries and optimize the sample's dimensions are presented. Afterwards, validation tests on PMMA and tests on wet R30A7 concrete will be shown.

2.1 Experimental setup: Triaxial press Giga

The tests have been conducted with a high-capacity triaxial press 'Giga' that originally allows loading a cylindrical concrete specimen 7 cm in diameter and 14 cm long.
Figure 2.1(a) shows a general view of the press. A cross-section of the confining cell is provided in Figure 2.1(b) . This press is able to generate a confining pressure of up to 0.85 GPa and an axial stress reaching 2.3 GPa. The concrete specimen is placed in the confining cell, and the confining fluid, diethylhexyl azelate - a non-volatile organic liquid, is injected into the cell through the upper opening. The cell is then pressurized by means of a multiplying jack. The axial force is generated from a 13 MN jack placed underneath the cell; this force is transmitted to the specimen via a piston that passes through the lower cell plug. An axial displacement sensor located on the machine is used to control the axial jack displacement, while the axial stress applied to the specimen and the pressure inside the cell are monitored by means of force and pressure sensors. The confining pressure and the axial jack displacement are controlled independently which allows different loading paths. A detailed description of the Giga press can be found in Gabet [2006] and Vu [2007].

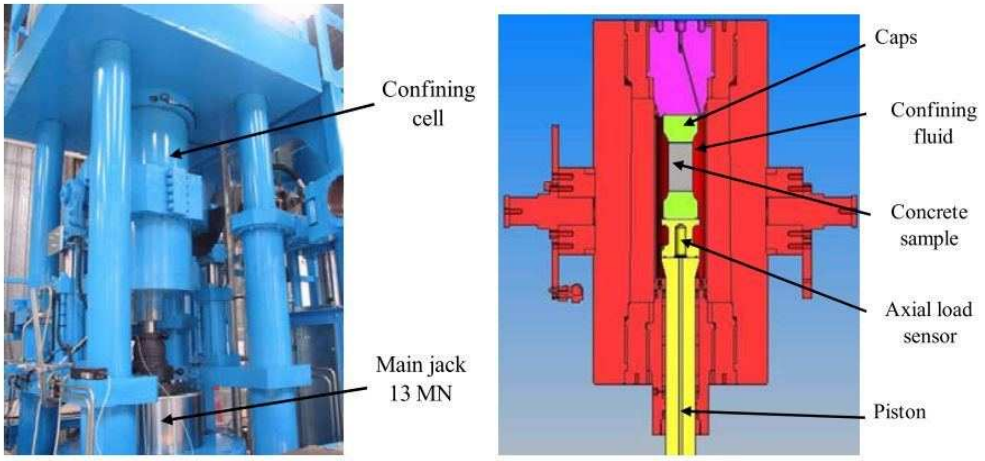

FIGURE 2.1: (a) General view of the Giga press (b) Cross section of the confining cell

2.2 Design of the test using numerical simulations

In order to determine the optimal sample geometry, numerical simulations have been conducted with the finite element code Abaqus/explicit. The test consists of a cylindrical specimen with two cylindrical notches drilled in the bottom and top surfaces. The notches were made in such way that the inner diameter of the lower notch and the outer

diameter of the upper notch coincide and make a straight cylindrical fracture surface (Figure 2.2).

The sample diameter was taken equal to 70 mm as required for the Giga press. Samples with different geometries with respect to the sample length and the ligament length and diameter have been carried out to study the influence of each parameter on the response of the sample. The Drucker-Prager model was used for concrete and 2D axisymmetric calculations were performed. In the first phase, the sample is subjected to hydrostatic pressure then an axial velocity is applied on the central part of the specimen to produce shear stresses in the ligament.

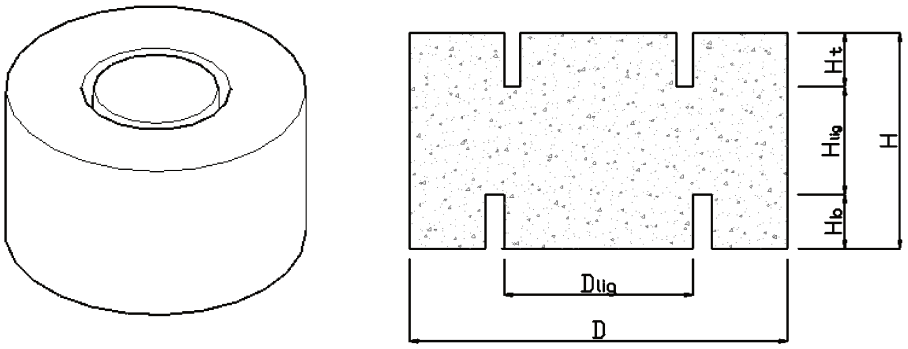

(a) (b)

FIGURE 2.2: 3D and 2D geometry for punching-through shear test specimen

2.2.1 Model description

2.2.1.1 Mesh

A 2D axisymmetric geometry was defined, the mesh shown in Figure 2.3(b) corresponds to the highlighted part of the specimen in Figure 2.3(a). Four nodes reduced integration elements (CAX4R) were used for modeling concrete sample and steel caps. The mesh has a uniform size of approximately 1 mm, the mesh sensitivity is studied in a following section.

2.2.1.2 Loading and boundary conditions

Two loading steps were created; in the first step a hydrostatic pressure is applied around the specimen. When this pressure becomes constant, a second step starts: the external upper part is restrained in displacement and a velocity is applied to the central bottom part (Figure 2.4) in order to produce shear in the ligament of the specimen.

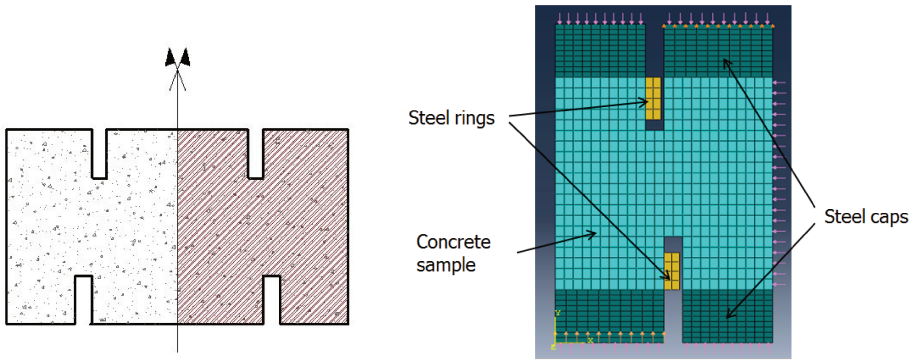

FIGURE 2.3: Finite element geometry and mesh

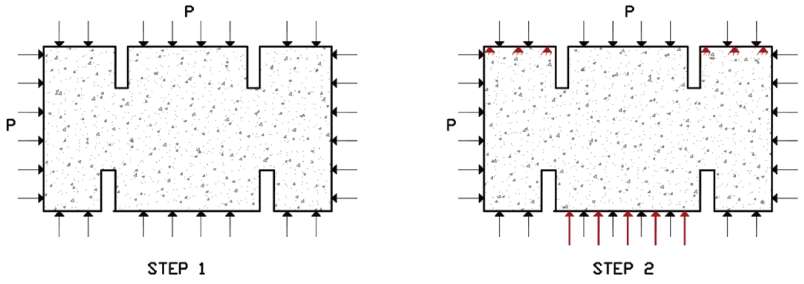

FIGURE 2.4: Loading applied to the specimen (a) Confining step (b) Shearing step

2.2.1.3 Material parameters

Steel caps were modeled assuming linear elastic behavior where the density is equal to $\gamma = 7800$ Kg/m^3, the Young modulus E=200 GPa and the poisson's ratio=0.3.

Concrete is a pressure-sensitive material that can be described using a 'Drucker-Prager' (Drucker and Prager [1952]) type of failure criterion. The material parameters for this model have been identified by characterization tests (PTS confined shear tests) results obtained for R30A7 formulation (Forquin and Sallier [2012]) and are listed in Table 2.1.

Parameters	Numerical concrete
σ_c	45 MPa
β	45°
ψ	10°

TABLE 2.1: Parameters of Drucker-Prager model used for R30A7 concrete

The linear Drucker-Prager criterion is written as:

$$F = q - Ptan\beta - c = 0 \tag{2.1}$$

where q is the equivalent Mises stress, P the hydrostatic pressure and c the cohesion of the material related to the input data as

$$c = (1 - \frac{1}{3}\tan\beta)\sigma_c \tag{2.2}$$

The hardening flow of the material is described in terms of the dilation angle ψ. With ψ=10°, a dilatancy is imposed during plastic deformation. The yield surface of the linear Drucker-Prager model is illustrated in Figure 2.5.

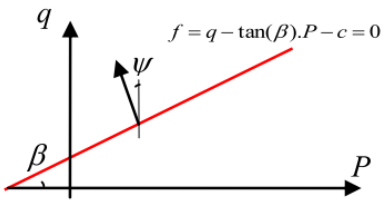

FIGURE 2.5: Linear Drucker-Prager model: Yield surface in the P-q plane (Forquin and Sallier [2012])

2.2.2 Influence of rings

Because the notches are drilled into the specimen, the top and bottom inner parts remain unconfined in the radial direction during the test. The axial stress applied on this zone being larger than the compressive strength of concrete, this zone could be damaged under compression before reaching any shear deformation. Consequently, two small steel rings were designed to prevent the radial deformation of the unconfined notch region. Figure 2.6 shows the difference in plastic strain in the sample without and with the two rings under a confining pressure of 100 MPa.

The numerical simulations clearly show that without the use of rings (Figure 2.6(a)), the deformation occurs mainly in the part where the vertical load is applied. When the rings are used (Figure 2.6(b)), the plastic strain is localized in the ligament and thus the objective of the test to produce shear stresses can be reached.

2.2.3 Mesh sensitivity

The mesh has a small influence on the shear and radial stresses and a significant effect on the shear deformation in the ligament. Figure 2.7 illustrates three sizes of mesh studied: 0.15 mm, 1.5 mm and 3 mm (with a notch width equal to 3 mm) and for these three configurations, the shear deformation in the ligament is checked (Figure 2.8). For a very

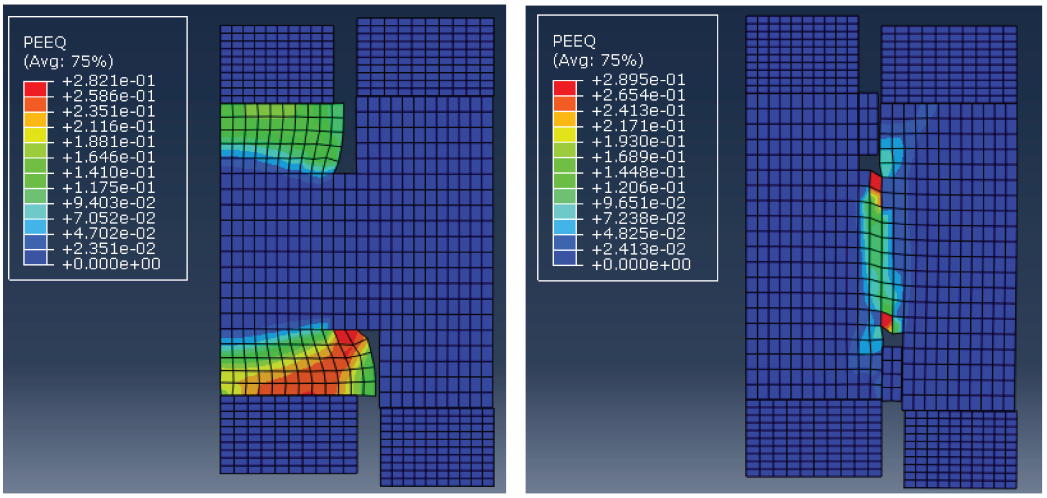

(a) (b)

FIGURE 2.6: Equivalent plastic strain after 1.3mm of displacement (a) without and (b) with rings

fine mesh, an excessive distortion of the small elements is noticed, shear deformation is localized in one range of elements and thus it is overestimated. While for a large mesh this value is smaller because a bigger surface is selected and the shear is underestimated.

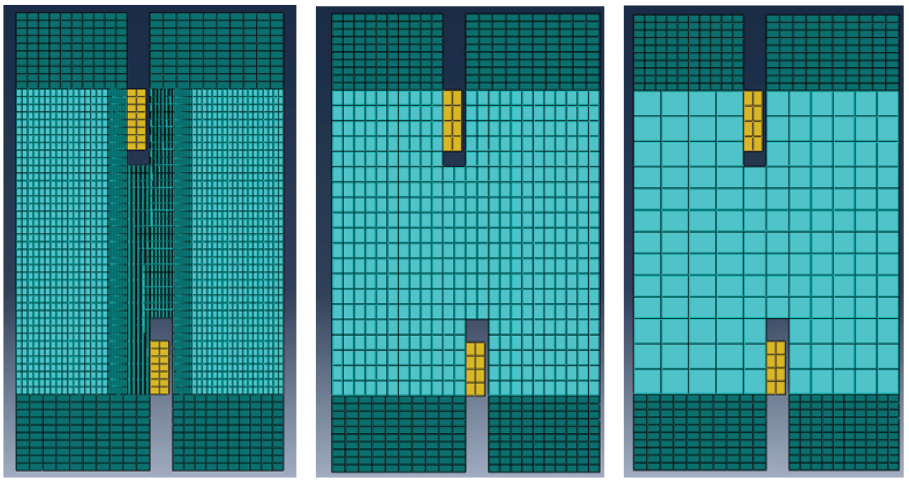

(a) (b) (c)

FIGURE 2.7: Different size of mesh studied (a) 0.15 mm (b) 1.5 mm (c) 3 mm

For the three configurations, shear deformation was calculated in the ligament and compared to the analytical solution. Sets of elements were selected and shear is averaged in these sets (Figure 2.10).

Regarding the analytical application, an element subjected to shear deformation as in Figure 2.9 is considered, one can calculate the nominal shear deformation of this element using equation (2.3):

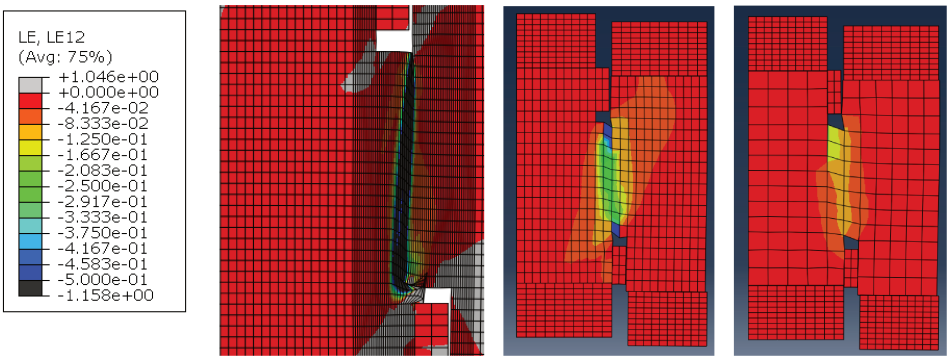

FIGURE 2.8: Shear Logarithmic strain after a displacement of 1 mm for different meshes

$$\epsilon_{xy} = \frac{1}{2}\gamma_{xy} = \frac{1}{2}(\frac{\partial u_x}{\partial y} + \frac{\partial u_y}{\partial x}) \tag{2.3}$$

Neglecting the deformation in the x direction, a nominal shear deformation of the notch can be defined as:

$$\epsilon_{xy} = \frac{U_{y(\text{imposed})}}{2e} \tag{2.4}$$

Where $U_{y(\text{imposed})}$ is the displacement applied to the central part of the specimen and e the notch width

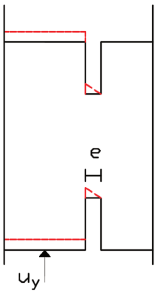

FIGURE 2.9: Shear deformation in the ligament

The shear deformation averaged in the ligament for the four configurations presented in Figure 2.10 and the nominal strain calculated according to equation (2.4) are plotted in Figure 2.11. It is observed that the deformation for the configurations (b) and (c) are the closest one to the nominal strain. In these configurations, the mesh size was taken equal to 1.5 mm and the width of the rows of the ligament was equal to the notch width e. The possible conclusion is that, roughly speaking, the shear strain is uniform along a width of length e. This is why the curves (b) and (c) are close. On the contrary, in case

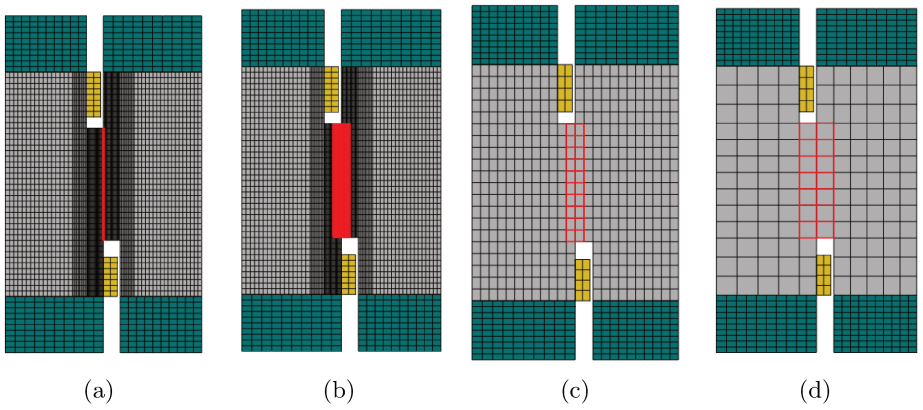

FIGURE 2.10: Different configurations with different meshes and different element sets in which shear strain is averaged and plotted in Figure 2.11.

(d), the strain is an average along 2e that's why the mean strain is smaller and in case (a), the mean strain is larger.

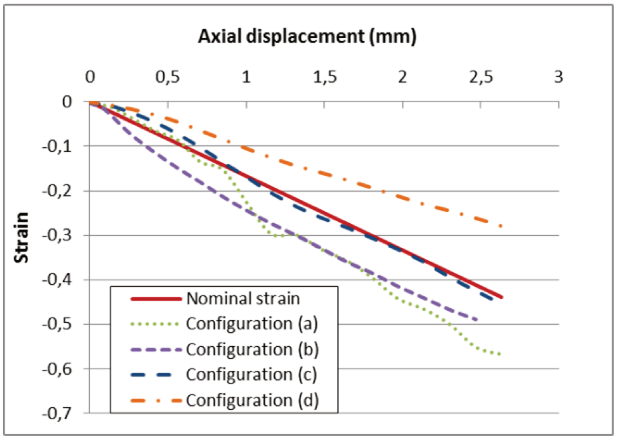

FIGURE 2.11: Shear strain values for different configurations (Figure 2.10) compared to the calculated nominal strain (equation (2.4)).

It was noticed that locally there is a mesh dependency regarding the shear deformation in the ligament in particular for mesh size equal or greater than the notch width e. But if the nominal stress is plotted as function of the nominal strain, the global response is the same for different meshes because the applied displacement is similar in the different cases. Therefore, equation (2.4) will be used to calculate the nominal strain of experimental tests.

2.2.4 Influence of sample length

Different numerical simulations were performed in order to study the influence of the sample length: the bottom notch length (H_b) and ligament notch length (H_{lig}) were both fixed to 10 mm while the upper notch length (H_t) was varied between 10, 15 and

20 mm which leads to a total sample length equal to 30, 35 and 40 mm. The results revealed that the shear and radial stress were the same within the three samples. For a higher upper notch length, higher tensile stresses were noticed near the upper ring, for this reason the upper notch should not be longer than 15 mm.

2.2.5 Influence of notch diameter and self-confinement

Simulations with different notch diameters D_{lig} ranging from 25 mm to 45 mm were performed. Due to the stiffness of the concrete sample, an orthoradial self-confinement can occur. In the literature (Forquin [2011b] and Forquin and Sallier [2013]), four radial notches at 90° were performed to avoid this self-confinement. In that case, the mean radial stress in the ligament can be deduced from the hydrostatic pressure P applied to the sample knowing the area of the lateral surface S of the specimen and the area of the fracture surface S_{lig}.

$$\sigma_{rr(\text{no self-confinement})}.S_{lig} = P.S \tag{2.5}$$

where

$$S_{lig} = \pi.D_{lig}.H_{lig} \tag{2.6}$$

and

$$S = \pi.D.H \tag{2.7}$$

If it was possible to assume none self-confinement, the above equation could be used and a value of radial stress in the ligament could be calculated and plotted in Figure 2.12 (dotted green curve). On the other hand, the true radial stress averaged in the ligament at 1.5 mm of displacement (peak of shear stress) can be calculated directly from the numerical simulations (dashed red curve) at 100 MPa of confinement. The influence of the confining pressure is discussed in section 2.5.

The ratio between the radial stress calculated from equation (2.5) and the numerical one obtained by Abaqus is plot in black in Figure 2.12. It is observed that the smaller the notch diameter is, the higher the ratio between stresses is. Thus for a small notch diameter, there is more self-confinement in the peripheral part of the concrete sample. Moreover, for a large notch diameter, a bending of the peripheral part was noticed because of the reduction of the peripheral thickness. Thus, as a compromise between both cases, the intermediate notch diameter of 35 mm was chosen.

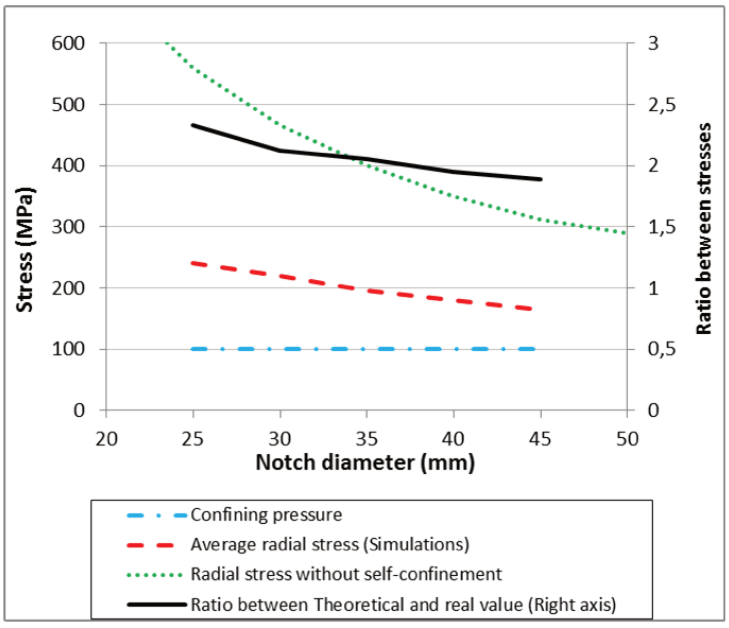

FIGURE 2.12: The radial stress given by equation (2.5) and the average true stress obtained by numerical simulations for different notch diameters after 1.5 mm of displacement

2.2.6 Influence of ligament length

To study the influence of the ligament length H_{lig}, the sample length H was fixed to 40 mm (as keeping the same sample length allows the use of the same testing set-up) and the lower notch length to 10 mm. Figure 2.13 shows the axial force applied in three different configurations: for upper notch length of 10, 15 and 20 corresponding to a shear length H_{lig} of 20, 15 and 10 mm respectively, under a confining pressure of 100 MPa.

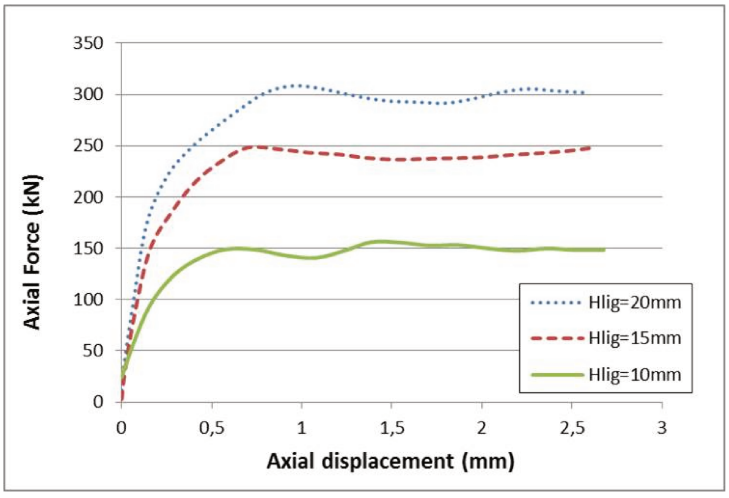

FIGURE 2.13: Axial force applied on the central part of the specimen vs axial displacement for different notches lengths. (Numerical simulations)

Many reasons influence the choice of the ligament length. One the one hand, it is necessary to choose the length which ensure a homogeneous stress field in the shear zone; numerical simulations showed that the homogeneity is more or less assured for the three cases. On the other hand, since the press capacity is quite big compared to the axial force, the signal to noise ratio is optimized by choosing a higher force and thus a higher ligament length. Furthermore, since the maximum aggregate size of the tested concrete is 8 mm, the choice of the lowest length was not considered to keep a homogeneous ligament. Thus, samples with 15 and 20 mm ligament length will be tested experimentally.

2.3 Specimen Geometry chosen

After conducting a series of numerical simulations, two final configurations of the sample were chosen to be tested experimentally. The specimens have a diameter D of 70 mm and a length H of 40 mm. The notch diameter D_{lig} was chosen equal to 35 mm and two ligament lengths H_{lig} will be tested, one of 15 mm and the other of 20 mm. The final geometry of the concrete is shown in Figure 2.14

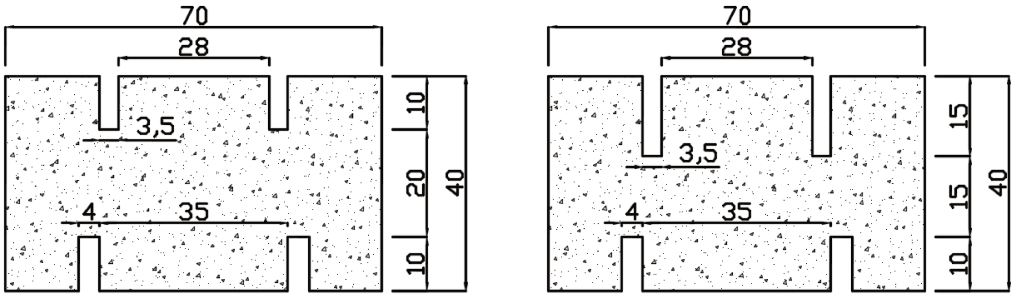

FIGURE 2.14: Geometry of the specimen tested experimentally

The width of each circular notch was finally imposed by the inner and outer diameters of the diamond drill bit. For the bottom notch (with the internal diameter equal to 35 mm), the width obtained was fixed to 4.5 mm and for the top one (with the internal diameter equal to 28 mm), the notch width obtained was 3.5 mm.

2.4 Modified triaxial cell

Special tools were designed for punching through shear test to work with the triaxial press Giga. In the initial configuration, the confining cell consists of a specimen of 70 mm and two caps of 80 mm each. This setup was replaced with a specimen of 40 mm

in length and two caps of 110 and 150 mm (Figure 2.15). A space of 20 mm was left inside the caps which allows the piston to slide and apply a displacement to the concrete specimen. Figure 2.16 illustrates a 3D sketch of the new set up. Joints are used between the caps and the piston in order to avoid the infiltration of the confining fluid. Numerical simulations were conducted to study the maximum stress the cap and the piston can sustain and thus choose the adequate material for them. Detailed technical drawings of the new setup developed can be found in Appendix A.

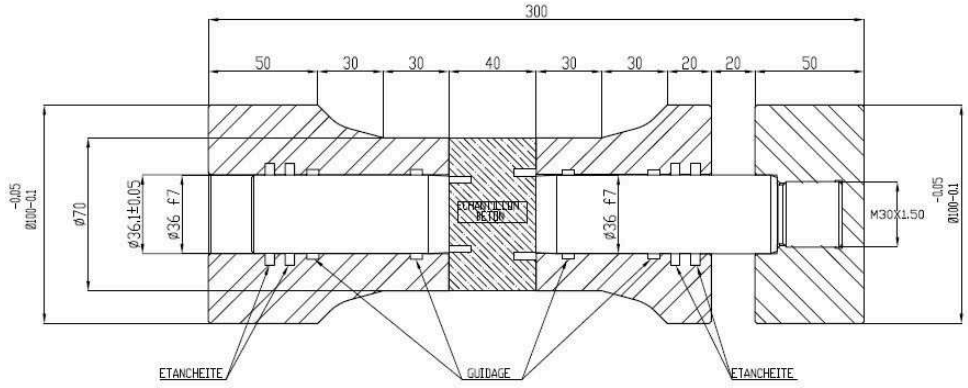

FIGURE 2.15: 2D section of the new shear test set-up

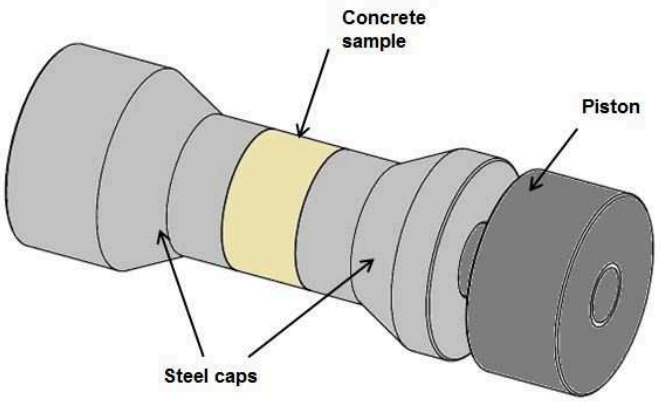

FIGURE 2.16: 3D sketch of the new shear test set-up

2.5 Stress and strain calculation

For all the tests done, first a hydrostatic loading, which consists of generating a confining pressure around the sample, is applied in a linear manner with a pressure rate of 100 MPa/minute (*i.e.* 1.67 MPa/s). When the pressure reaches the constant value required, the displacement of the piston starts with a rate of 20 μm/s.

The pressure sensor, installed close to the entrance of the confinement cell, determines the pressure within the cell with a measurement accuracy of 1% over the operating range. The force sensor, positioned between the lower loading head and the piston (cf. Figure 2.1(b)), is a metal body that deforms elastically over the machine loading range. The force transmitted by the sensor is deduced from its strain. The shear stress is then calculated from this axial force using equation (2.8).

$$\sigma_{shear} = \frac{F_{axial}}{S_{lig}} \tag{2.8}$$

with S_{lig} given in equation (2.6).

Each part of the LVDT sensor is fixed on a loading head. The shortening generated by the deformation of the caps is considered negligeable compared to the displacement of the concrete sample. Therefore, it is considered that the LVDT sensor allows to calculate directly the displacement of the central part of the specimen. The nominal strain is thus calculated using equation (2.9).

$$\epsilon_{\text{nominal}} = \frac{U_{\text{LVDT}}}{2e} \tag{2.9}$$

Moreover, the nominal strain-rate can then be deduced:

$$\dot{\epsilon}_{\text{nominal}} = \frac{V}{2e} \tag{2.10}$$

Since $V = 20\mu$m/s and $e = 4$ mm, the corresponding nominal strain rate is equal to 2.5x10^{-3} /s.

Since it is difficult to measure radial stresses in the ligament, an estimation of this stress was elaborated from the numerical simulations. The Drucker-Prager model, used for the concrete, was described in section 2.2.1.3. Different confining pressures were applied to the numerical model and for each pressure, the average of the radial stress is calculated in the ligament at 1.5 mm of vertical displacement (which corresponds to the peak of shear stresses). Three values of the dilation angle describing the flow rule has been studied (5, 10 and 15°), a variation of 10% of the true radial stress in the ligament was observed (Figure 2.17).

From the other hand, if one considers that the self confinement in the concrete sample doesn't happen, the radial stress calculated from the confining pressure multiplied by the surface ratio (equation (2.5)) is also determined.

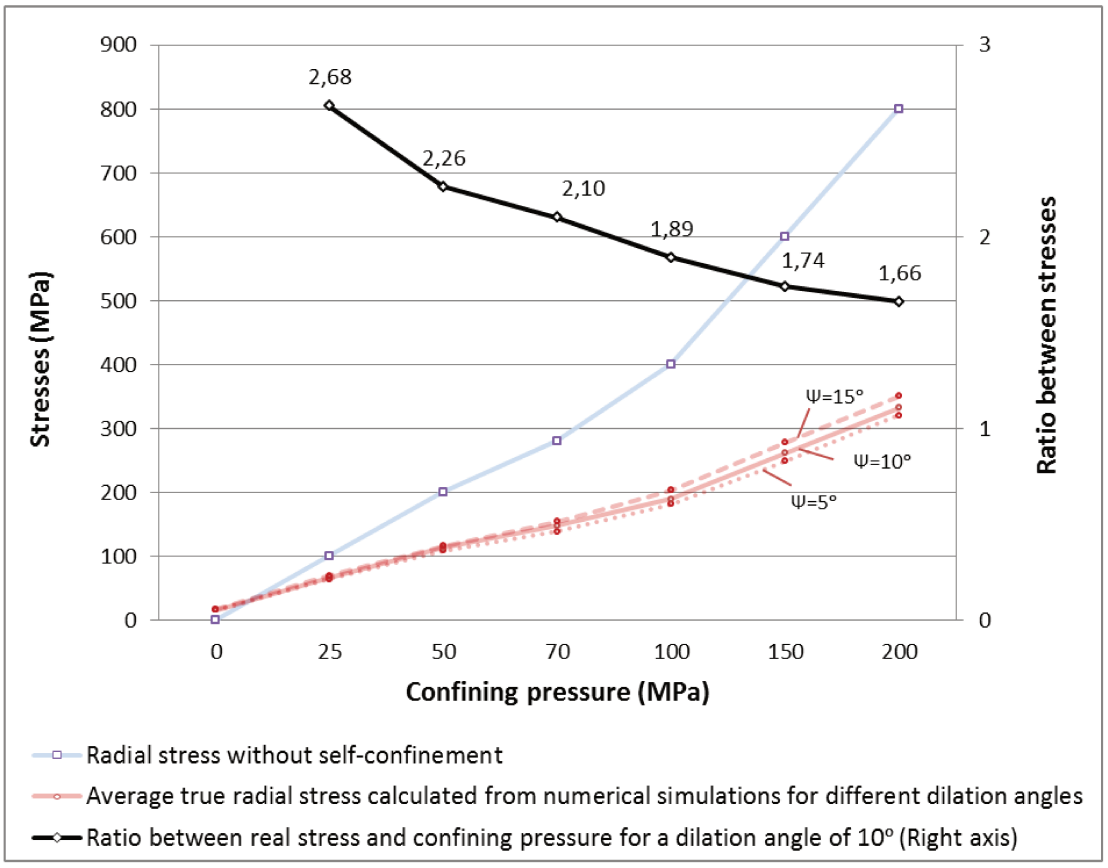

FIGURE 2.17: The radial stress given by equation (2.5) and the true average radial stress obtained by the numerical simulations for different confining pressures for a ligament length of 20 mm

The ratio between the confining pressure applied at the lateral surface of the specimen (40 mm in length) and the true radial stress calculated in the ligament of the sample (for $H_{\text{lig}} = 20\text{mm}$) after 1.5 mm is then estimated and can be used in experiments.

2.6 Concrete composition and sample preparation

2.6.1 Concrete composition

The R30A7 concrete, which will be denoted OC (ordinary concrete) in the following, is a standard concrete thoroughly studied by many authors (Piotrowska [2013], Forquin and Sallier [2013], Vu et al. [2009b], Zingg et al. [2016]). It has a 28-day compressive strength of 30 MPa and a slump of 7cm. Furthermore, High Performance Concrete (HPC) samples were generated in seeking to remain close to the R30A7 composition in terms of the granular skeleton. The capillary porosity was decreased by adding silica fumes and decreasing the W/C ratio to 0.3 thus corresponding to a uniaxial compressive

strength at 28 days f_{c28}=80 MPa. Concrete composition and mechanical properties are presented in Table 2.2.

Concrete mix proportions	OC (R30A7)	HPC
Siliceous gravel D 0.5/8 mm (kg/m^3)	1008	1008
Sand Dmax 1.8 mm (kg/m^3)	838	795.4
Cement CEM I 52.5 N PM ES CP2 (kg/m^3)	263	420
Water (kg/m^3)	169	140
Silica fumes (kg/m^3)	-	46.7
Superplasticizer (kg/m^3)	-	4.7

Mechanical properties	wet	dry	
Density (Kg/m^3)	2278	2290	2415
Compressive strength f_{c28} (MPa)	30	42	80
Porosity accessible to water	11.8		8.8
Water/cement ratio	0.64		0.3

TABLE 2.2: Composition and mechanical properties of ordinary concrete (OC) and high-strength concrete (HPC) [Vu et al. [2009b] and Zingg et al. [2016]]

2.6.2 Sample preparation

After casting concrete in the rectangular molds, cylindrical specimens are drilled then a sample of 40mm height is cut with a saw. Afterwards, the two faces of the samples are ground and circular notches are drilled to the depth needed on the top and bottom surfaces with a diamond drill bit placed in a concrete lathe (Figure 2.18).

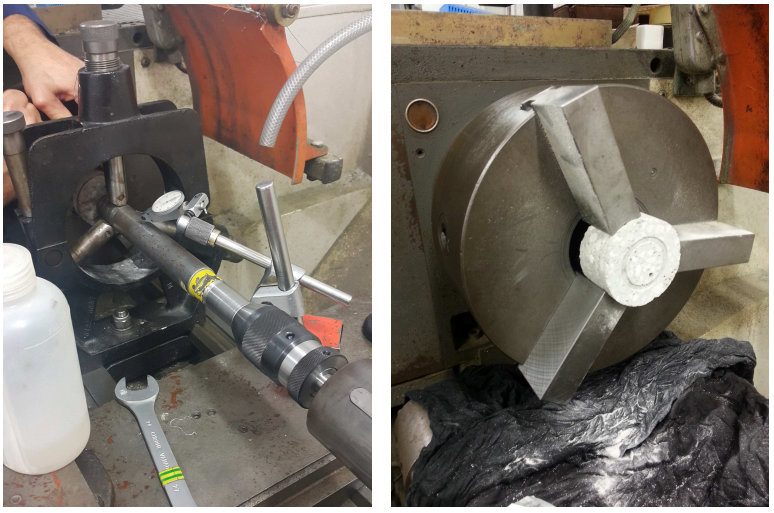

(a) (b)

FIGURE 2.18: (a) Conrete lathe used to make the notches in concrete samples (b) zoom on the sample

Steel rings were glued to the sample prior to each test (Figure 2.19): one of 29 mm inner diameter, 2.5 mm thick, 7 mm height and the other of 34 mm inner diameter, 3.5 mm

thick, 8 mm height for a notch of 10 mm (12 mm for a notch of 15 mm). The rings have a high elastic limit of approximately 1.2 GPa in order to resist to the applied axial load. The glue used is a bi-component resin named Chrysor. This step was carefully carried out to avoid any gap between concrete and steel that could otherwise lead to non desirable damage due to non-effective confinement. A deformable thick scotch is put inside the notch before inserting the ring in order to ensure that this last will not fall to the bottom of the notch.

FIGURE 2.19: Concrete sample equipped with a ring

(a) (b)

FIGURE 2.20: Membrane used for testing samples in the Giga press

The specimen is then wrapped within a multilayer protective membrane in order to prevent the confining fluid from infiltrating the sample (Figure 2.20).

2.7 Validation tests on PMMA

The polymethylmethacrylate (PMMA) is a homogeneous and non porous material that has been studied by many authors due to its testing ease, simplicity of specimen preparation, and possible field applications. In addition, it is a transparent material which makes it easier to investigate fracturing mode inside the samples. For these reasons, PMMA is a good material candidate to proceed to validation tests.

2.7.1 Brief literature review

The polymethylmethacrylate, PMMA, is a material of major interest because it is likely to be used in aeronautics, protective structures and armor systems thus it is important to evaluate its behavior under confinement to ensure a reliable performance. Many authors studied the mechanical behavior of PMMA subjected to compression under static or dynamic loadings. Rittel and Brill [2008] studied the pressure-sensitivity of PMMA at various strain rates, they confined cylindrical specimens with a tightly fit metal sleeve and subjected them to compression tests. A brittle to ductile failure mode transition appeared in the PMMA as confining pressure increases. The radial cracking and fragmentation process were observed in brittle failure, and a truncated conical plug in the ductile regime.

Forquin et al. [2012] applied the same technique developed for concrete to PMMA specimens (Forquin et al. [2008b]), these latter were enclosed in a brass or aluminum cell and then subjected to axial compression either with a normal testing machine or with the Split Hopkinson bar device. For quasi-static loading, the maximum strength is not affected by confining pressure since same results were obtained for aluminum and brass cells. An elasto-plastic behavior was observed and an inclined crack was propagating. A brittle failure occurred beyond a certain level of loading corresponding to the propagation of the crack. Under dynamic loading, an elastic-brittle behavior is observed and a mode II fracture pattern composed of one or two conical fracture surfaces are initiated from the corners of the specimen.

The outcome of the above results is that confinement in brittle polymers causes a failure mode transition from brittle to ductile which is identical to that observed in concretes or ceramics. Thus it would be interesting to study the PMMA behavior under confined mode II conditions.

2.7.2 Mechanical properties

The compressive strength of PMMA was obtained by conducting simple compression tests done on specimens 14 mm in length and 10 mm in diameter. The other mechanical properties of the PMMA are provided by the manufacturer and listed in Table 2.3.

Parameters	
Density (Kg/m^3	1190
Elastic modulus (MPa)	3300
Poisson Coefficient	0.39
Compressive strength (MPa)	105

TABLE 2.3: Mechanical properties of PMMA tested

2.7.3 Testing program

Four tests were conducted on PMMA specimens (with a ligament length of 15 mm) : the first one PTSS2 was performed with the Schenck press, a normal hydraulic press without a confinement. The 3 others were performed with the Giga press. PTSG1 was conducted with a confining pressure of 50 MPa, the test is stopped when failure occurs and the force starts decreasing. PTSG2 was conducted with the same level of confining pressure (50 MPa) but the test was stopped after 3 mm of displacement in order to check the sample state before failure. PTSG3 was carried out with 30 MPa of confinement. Table 2.4 summarizes punching-through shear tests performed on PMMA specimens.

Test name	Hydraulic press used	Description of the test
PTSS2	Schenck	P = 0 MPa
PTSG1	Giga	P = 50 MPa
PTSG2	Giga	P = 50 MPa (the test is stopped before failure)
PTSG3	Giga	P = 30 MPa

TABLE 2.4: Summary of the tests performed on PMMA specimens

2.7.4 PTS tests on PMMA

Figure 2.21 shows the stress-strain curve of four specimens with and without confinement loaded statically using a hydraulic normal press.

For the unconfined test, after the elastic part, a small softening occurs when the nominal strain reaches 40%. Afterwards, at 70% of strain, a brittle behavior is observed. When a lateral confinement is applied, a clear change in the stress-strain behavior of the material is observed. A similar trend is observed for the elastic part, however a hardening effect is observed for confined tests. For a confinement of 30 MPa, the failure occurs at 80% of

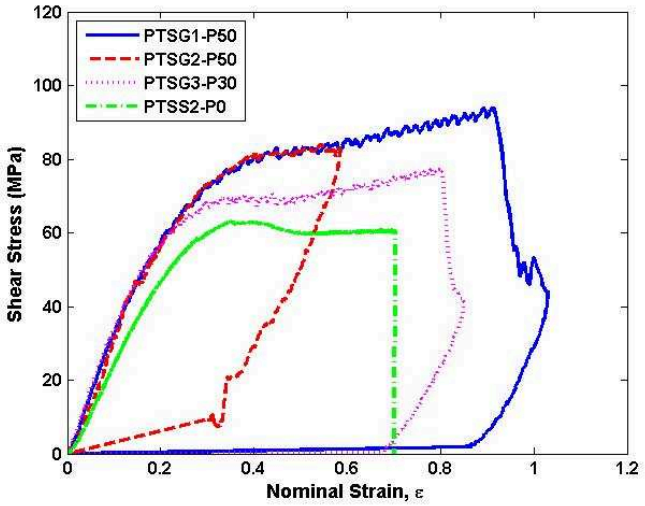

FIGURE 2.21: Results of punching-through shear tests on PMMA specimens for different confining pressure

the nominal strain, for 50 MPa it goes till 100%. Regarding the maximum shear stress, inspection of Figure 2.21 indicates that the peak stress of the material is seen to increase with the confining pressure. For a confinement of 30 MPa, a shear stress of 70 MPa was observed, while for a 50 MPa of pressure, the shear stress reaches 80 MPa at the peak.

The evolution of PMMA behavior with the confining pressure results in different damage patterns presented in Figure 2.22. For unconfined PMMA, a fragmentation of the specimen occurred, this latter was divided into different pieces (Figure 2.22(b)). For confined specimens, a mode II fracture can be noticed inside the ligament (Figure 2.22(c)), this fracture occurred at failure. It was verified by stopping the test before failure after 50% of strain (PTSG2) that no cracks were observed inside the ligament (Figure 2.22(d)).

Tests on specimens with a ligament length of 20mm were performed. Since a higher force is applied on the central part of the specimen, the unconfined compression strength of PMMA (equal to 105 MPa) was exceeded and this part swells and was damaged under compression (Figure 2.23). Consequently, this configuration was not taken into consideration.

From the above results, one can conclude that the new testing method developed was able to generate shear fracturing inside the samples tested, this mode II fracture occurred at failure. Moreover, the sample geometry with a ligament length equal to 15 mm is more preferable than the 20 mm in order to avoid the damage of the central part. Finally, the increase of confinement level in the shear ligament of the samples lead to a higher shear strength.

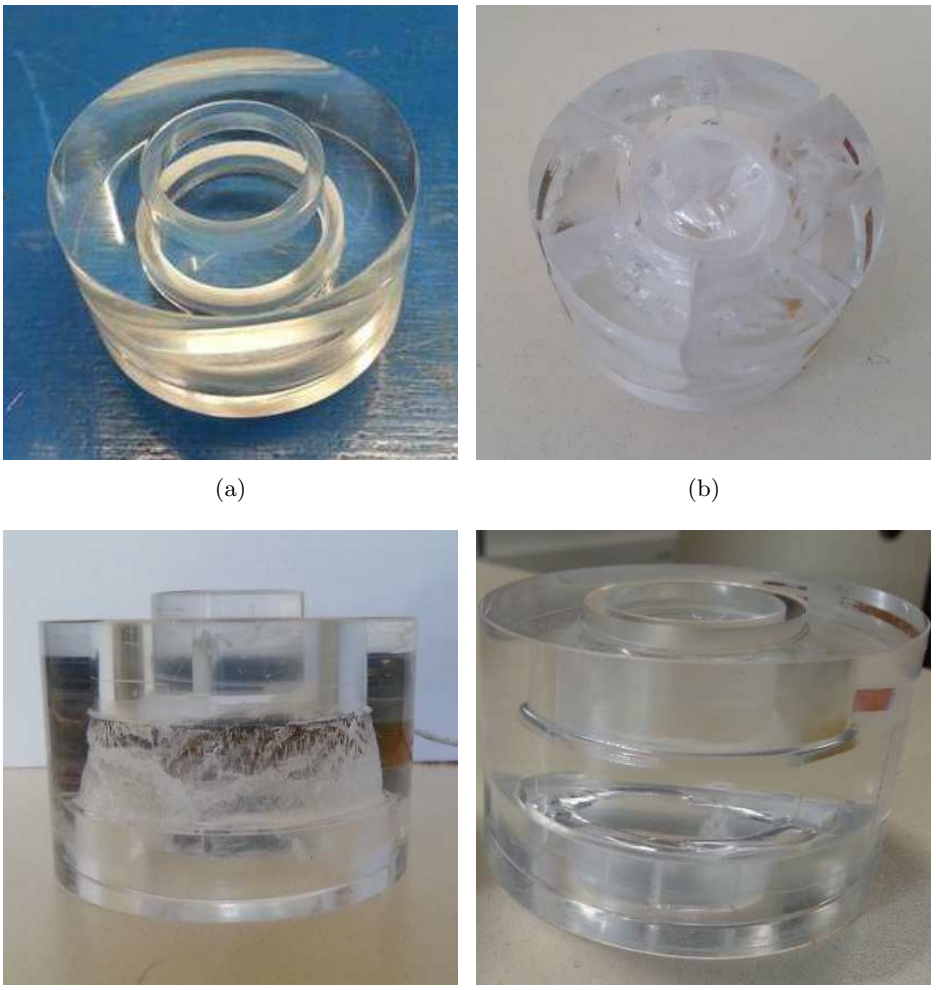

(a) (b)

(c) (d)

FIGURE 2.22: PMMA specimen (a) before testing (b) after test PTSS2 (without confinement) (c) after test PTSG1 (confining pressure P=50 MPa) (d) after test PTSG2 (P=50 MPa, specimen before failure)

FIGURE 2.23: PMMA specimen with a ligament length of 20mm, central part damaged under compression

2.8 Experimental Results on concrete

2.8.1 Testing program

Three tests were conducted on R30A7 concrete specimens and are summarized in Table 2.5. Different ligament lengths and different confinement pressures were tested to study their influence on the shear response of concrete.

Test name	Ligament length	Confining pressure
PTSG1	20 mm	50 MPa
PTSG2	15 mm	50 MPa
PTSG3	20 mm	100 MPa

TABLE 2.5: Summary of the tests performed on R30A7 concrete specimens

2.8.2 Influence of rings

Preliminary tests have been conducted on R30A7 concrete, one with the ring around the notches and the other without them. The confining pressure applied was 50 MPa. It was observed after the tests that the central part of concrete specimens confined with the rings was not damaged under compression on one hand and that the rings diameter remained constant on the other hand. These observations confirmed that the rings remained in the elastic deformation regime and allowed the confinement of the central part of the specimen. Thus, using the ring was successful and permitted to reach the objective of the test.

(a) (b)

FIGURE 2.24: Concrete specimens after PTS testing with a confining pressure of 50 MPa (a) without rings (b) with rings

2.8.3 Influence of ligament length

To study the influence of the ligament length H_{lig} on the failure stress of the punching-through shear test, the lower notch length was fixed to 10 mm and the upper length was varied between 10 and 15 mm which leads to a ligament length of 20 and 15 mm respectively (according to Figure 2.14). The confining pressure applied was equal to 100 MPa, thus the estimated radial stress in the ligament is around 190 MPa for a ligament length H_{lig} equal to 20 mm (according to Figure 2.17) and around 215 MPa for H_{lig} equal to 15 mm. The experimental results are reported on Figure 2.25.

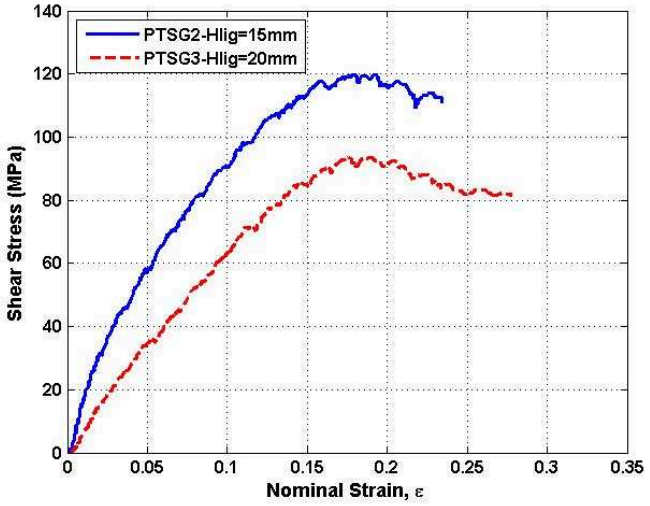

FIGURE 2.25: Results of quasi-static punching through shear tests performed on R30A7 concrete for a confining pressure of 100 MPa and different ligament lengths

Figure 2.25 shows a quasi-linear behavior then a decrease of stress after the peak. The average shear stress between the notches increases for a smaller ligament length *i.e* for a smaller shear surface. For a ligament of 15 mm in length, the stress reaches a value of 120 MPa while for a 20 mm ligament length shear stress is around 97 MPa. This can be explained by the fact that for a smaller ligament length, the radial stresses are higher and thus the shear stresses are higher. It could also be explained by the development of micro-cracks at the edges of the notches which leads to the initiation of failure in the concrete sample.

The rings used allowed the confinement of the central part and the creation of mode II fracturing inside the sample. But one of the drawback of the rings is the limitation in the displacement of the central part. Since the lower notch length is equal to 10 mm and the ring has a length of 7 mm, only 3 mm of displacement can be applied. This corresponds to a nominal deformation of about 30%.

2.8.4 Influence of confining pressure

Experiments with two different confining pressures (50 and 100 MPa) were carried out on R30A7 concrete. Samples with a ligament length of 20 mm were used. Results of these quasi-static PTS tests are reported in Figure 2.26. The radial stress estimated in the ligament after 1.5 mm of displacement is around 113 MPa for a lateral confining pressure of 50 MPa and 190 MPa for a lateral pressure of 100 MPa (cf. Figure 2.17).

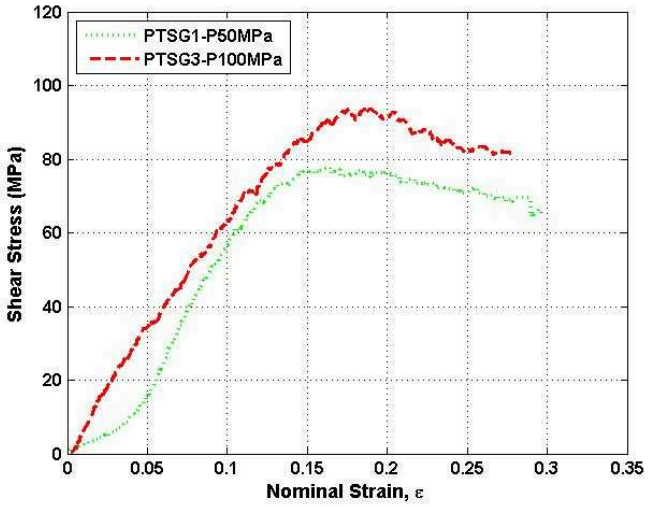

FIGURE 2.26: Results of quasi-static punching through shear test performed on R30A7 concrete for a ligament length of 20 mm at different confinement levels

A deviation in the slope of PTSG1 test was reported, this problem might occur if there is no perfect contact between the sample and the steel cap before starting the test. For the PTSG3, an initial linear behavior was followed by a strain softening at 20%.

The maximum shear stress reached for a confining pressure of 50 MPa was 78 MPa while on the other hand the specimen subjected to a confining pressure of 100 MPa exhibited higher shear stress of about 95 MPa. Thus, higher shear strength is observed for higher confinement pressure, this can be mainly due to a higher radial stresses generated in the shear ligament.

2.8.5 Post-mortem observation

The specimens subjected to punch-through shear testing are shown in Figure 2.27 and 2.28. The proposed test seems capable of producing a controlled mode II fracture as predicted in numerical simulations. From the viewpoint of post-mortem specimen observation, the lower central part was not damaged, it was punched inside the specimen

and the upper central notch was pushed outside the specimen. For the specimen subjected to 50 MPa, one radial crack was observed after the test. This could be explained that even at confinements of 50 MPa the dilatant behavior of concrete is not absolutely suppressed.

(a) (b)

FIGURE 2.27: Concrete specimen subjected to a confining pressure of 50 MPa

It was difficult to check the failure patterns inside the sample by cutting the specimen parallel to the displacement direction because of the rings glued. The cut was then done in the radial direction, a crack parallel to the axial direction is observed and most of the aggregates are debonded around the cracks (Figure 2.29). Piotrowska et al. [2014] and Poinard et al. [2012] reported that the cracks have avoided the aggregates during trixial tests performed on R30A7 concrete samples.

(a) (b)

FIGURE 2.28: Concrete specimen subjected to a confining pressure of 100 MPa

FIGURE 2.29: View from the inside of a concrete specimen subjected to a confining pressure of 100 MPa

2.9 Conclusion

A new experimental technique was proposed in order to investigate the shear behavior of concrete under high confinement subjected to quasi-static loading. The setup is based on the punching through shear test and consists in applying a confining pressure up to 100 MPa before subjecting concrete sample to shearing. A large capacity triaxial press 'Giga' has been used to apply the high level of confinement and two steel rings were glued around the unconfined part of the specimen to prevent it to be damaged under compression. Experimental tests conducted on R30A7 concrete showed that the use of the rings was advantageous and allowed orienting the crack parallel to the loading direction as demonstrated in numerical simulations. Two different ligament lengths were chosen to be studied experimentally. The same force was obtained for both tests and higher shear stresses were deduced for a smaller shear surface. This might be explained by the fact that the development of cracking on the edges of the notches is the phenomenon which leads to the initiation of failure in concrete. Different levels of confining pressure were applied to study the influence of confinement on the shear behavior of concrete. It was concluded that for higher confinement, higher force was applied to the specimen before failure and thus higher shear strength is obtained in the shear ligament. This difference confirms the pressure sensitivity of concrete under shear loading. The tests were stopped at around 3 mm of displacement, otherwise the ring would touch the internal part of the specimen. The displacement at the peak of shear stress was around 1.5 mm leading to a nominal strain around 20%. Consequently, the objective of the present work to apply a high confinement pressure and obtain a high deformation level in a concrete sample was achieved.

Chapter 3

2D static and dynamic Punching Through Shear test

The objective of this part of the study is to develop an experimental method which allows to study the behavior of concrete subjected to a certain confinement under Mode II fracture propagation in static and dynamic conditions. This should supply the development of a testing method able to generate a pre-confinement in concrete prior to testing it under shear. The first part of the chapter will focus on the numerical simulations done for dimensioning the test and in the second part, the experimental procedure and experimental results are presented.

3.1 Design of the test using numerical and analytical methods

This section gives a detailed description of the simulations done on Abaqus in order to optimize the test configuration. In parallel, some analytical calculations were conducted to compare them with the simulations. The design of the confinement cell is first presented and the optimization of the concrete sample geometry is then described.

3.1.1 Confinement procedure

As detailed in Chapter 1, in dynamic punching through shear tests existing in the literature, the confinement applied was a passive confinement (Forquin [2011a], Forquin and Sallier [2013] and Lukić and Forquin [2015]). These tests consist of inserting the concrete specimen inside a confinement ring which allows inducing a confinement pressure due

to the dilating behavior of concrete. The drawback of this method is the variation of the pressure in the shear loading phase. The originality of the present work regarding the confinement is the use of a pre-confinement applied to the specimen before testing it under shear (Figure 3.1).
A new experimental technique is proposed and consists of:
- deforming elastically an instrumented ring by applying a compressive load,
- when the ring is deformed, the concrete specimen is inserted inside,
- the gap between the confining ring and the specimen is filled with thin metal sheets to obtain the needed confinement,
- the load is released and while the ring returns back to its initial position, it applies the confinement to the concrete specimen.

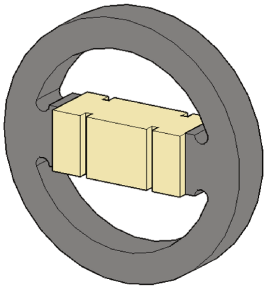

FIGURE 3.1: A schematic view of a concrete sample confined with a ring

In order to be able to compare tests conducted with the Giga press at high confinement with the tests that will be presented hereafter, it is better to choose two geometries that have approximately same ligament dimensions. The first suggested geometry for the parallelepiped concrete sample is a length of 70 mm, a width B of 40 mm, a height of 40 mm with a ligament height of 20 mm (cf. Figure 3.8). This corresponds to a shear surface equal to $S_{ligament} = 2.B.H_{lig}$= 2*40*20=1600 mm^2 close to the shear surface of the cylindrical sample equal to $S_{\text{lig}} = \pi.D_{\text{lig}}.H_{\text{lig}} = \pi$* 35* 15 = 1650 mm^2 (according to equation (2.6)).

In the following, numerical simulations are performed to choose the best dimensions and set the experimental configuration.

3.1.1.1 Design of the confinement ring

Let us consider a circular ring compressed by two equal and opposite forces acting along a diameter (Figure 3.2). Taking advantage of the two symmetry along the vertical and horizontal axis, a quarter of the geometry can be selected for the analytical study. We can then consider the quadrant as fixed at one end and loaded by a vertical load and an undetermined moment.

The stresses produced by the pure moment can be found by energy considerations assuming the quadrant as a curved beam with purely elastic linear isotropic behavior.

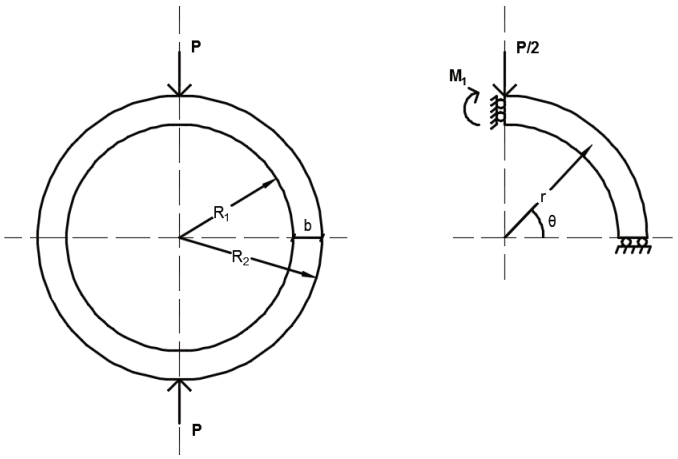

FIGURE 3.2: A circular ring and its quadrant subjected to a compressive force

Let M_1 be the moment acting at the end of the quadrant where the normal load P is also acting, R_1, R_2 and R are the internal, external and mean radius, b the width and t the thickness of the ring.

According to Timoshenko and Goodier [1951], the eccentricity e of the neutral axis in pure bending is given by:

$$e = \frac{b^2}{12R}[1 + \frac{4}{15}(\frac{b}{2R})^2] \tag{3.1}$$

For sake of simplicity and since $b \ll 2R$, equation (3.1) can be written: $e = \frac{b^2}{12R}$.

At any section θ of the quadrant, the moment M, the normal force N and the shear force V are equal to:

$$\begin{aligned} M &= M_1 - \frac{P}{2}Rcos\theta \\ N &= -\frac{P}{2}cos\theta \\ V &= \frac{P}{2}sin\theta \end{aligned} \tag{3.2}$$

The elastic energies due to the moment, normal force and shear force in the elementary volume $dS = Rd\theta$ are respectively equal to:

$$\begin{aligned} dU_1 &= \frac{M^2 dS}{2AEeR} \\ dU_2 &= (\frac{N^2}{2} - \frac{MN}{R})\frac{dS}{AE} \\ dU_3 &= \frac{\alpha\, V^2 dS}{2AG} \end{aligned} \tag{3.3}$$

where α is a constant, $A = bt$ is the area of the cross section of the ring, E its young modulus and G its modulus of rigidity (Srinath and Acharya [1953]).

The total strain energy in an element $dS = Rd\theta$ of the ring is equal to:

$$dU = [\frac{M^2}{2AEeR} + \frac{N^2}{2AE} - \frac{MN}{AER} + \frac{\alpha\ V^2}{2AG}]Rd\theta \tag{3.4}$$

By replacing the values of the moment, the normal force and the shear in the above equation, it comes that:

$$U = \int_0^{\frac{\pi}{2}} [\frac{(M_1 - \frac{P}{2}Rcos\theta)^2}{2AEeR} + \frac{(-\frac{P}{2}cos\theta)^2}{2AE} - \frac{(M_1 - \frac{P}{2}Rcos\theta)(-\frac{P}{2}cos\theta)}{AER} + \frac{\alpha\frac{P}{2}sin\theta^2}{2AG}]Rd\theta \tag{3.5}$$

According to Castigliano's theorem (Prasad et al. [2011]), the moment M_1 should be such that $dU/dM_1 = 0$, then, equation (3.5) leads to:

$$\int_0^{\frac{\pi}{2}} (\frac{M_1}{e} - \frac{PR}{2e}cos\theta + \frac{P}{2}cos\theta)Rd\theta = 0$$

$$\frac{M_1\pi}{2e} - \frac{PR}{2e} + \frac{P}{2} = 0$$

$$M_1 = \frac{P}{\pi}(R - e)$$

$$M = \frac{P}{\pi}(R - e) - \frac{P}{2}Rcos\theta \tag{3.6}$$

The normal stresses at any cross section are the sum of the stresses due to bending moment and normal force. Let σ_θ be the normal stress, σ_{θ_1} and σ_{θ_2} the bending and direct stresses component. They are equal to (Srinath and Acharya [1953]):

$$\sigma_{\theta_1} = \frac{My}{Ae(r_n - y)}$$

$$\sigma_{\theta_2} = -\frac{P}{bt} \tag{3.7}$$

r_n being the radial ordinate for the neutral axis and y being the distance of any point from the neutral axis of the ring cross section along a radius.

The total normal stress is then equal to:

$$\sigma_\theta = \frac{y}{Ae(r_n - y)}[\frac{P}{\pi}(R - e) - \frac{P}{2}Rcos\theta] - \frac{P}{bt} \tag{3.8}$$

By substitution and for $y = \frac{b}{2}$

$$\sigma_\theta \approx \frac{3PR}{tb^2}(\frac{2}{\pi} - cos\theta) - \frac{P}{bt} \tag{3.9}$$

The maximum radial stress occurs at the position where the load is applied (θ=$\pi/2$) and thus

$$\sigma_\theta \approx \frac{6PR}{\pi tb^2} \tag{3.10}$$

This equation is useful in obtaining an approximation of the hoop stresses and strains in a circular ring. For more precise values of the stress and strain distribution along the modified shape of the ring, finite element analysis has been used.

Numerical Simulations

Ring dimensions (b, t and R) were optimized by performing numerical simulations on Abaqus explicit. These simulations aim to obtain the best dimensions for the final geometry which allows the ring to handle a certain diametrical force while remaining in the elastic mode. A 2D model was used; it was drawn taking into consideration the symmetry with respect to X and Y axis. In the following simulations, the material properties used for aluminum and steel are presented in Table 3.1.

Material mechanical parameters	aluminum	Steel
Density (kg/m^3)	2700	7800
Yound Modulus (GPa)	70	200
Poisson ratio	0.3	0.3

TABLE 3.1: Mechanical properties of material used in numerical simulations

After performing several simulations, the final dimensions were chosen as: the mean radius R=57.5 mm (R_1=50mm and R_2=65 mm), the width b=15 mm and the thickness t=20 mm.

One example of the calculation done is shown in Figure 3.3. A load of 20 kN was applied to a small plate in interaction with the ring in order to avoid the concentration of stresses and a high distortion on the node where the load is applied. The Mises stress obtained in the ring are shown in Figure 3.3(b).

After calculating Huber-Mises stresses inside the ring, two types of ring will be tested, one made of aluminum and the other made of steel with a yield strength of 485 MPa and 1100 MPa respectively.

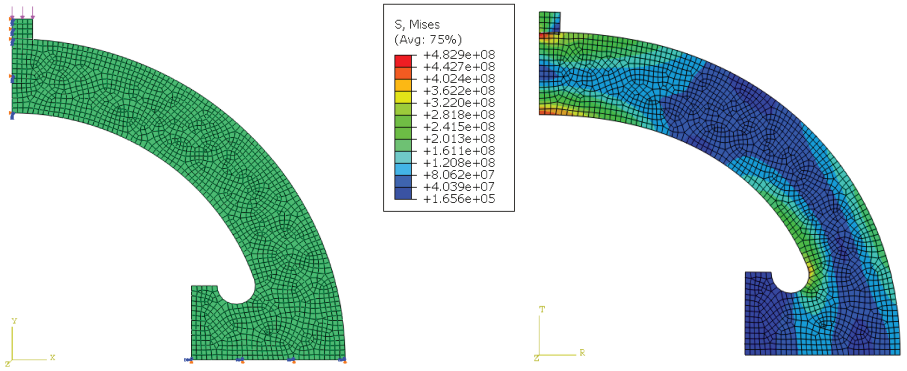

(a) (b)

FIGURE 3.3: 2D numeircal model for ring dimensioning (a) geometry and loading (b) Mises stress distribution inside the ring for a force of 20 kN

The force applied to the ring was set to 80% of the maximum force the ring can sustain. For the aluminum ring the maximum force applied is around 16 kN which produces 390 MPa of Huber-Mises stress. Regarding the steel ring, a force of 36 kN could be applied that corresponds to a maximum Mises stress of about 900 MPa.

As the ring can be considered as a measurement device, the advantage of using an aluminum ring is its small stiffness: for a specific load applied, higher deformation are obtained for the aluminum ring and thus the signal to noise ratio is better. The steel ring has higher yield strength which allows to sustain higher force, therefore one can apply higher confinement. Hence, the aluminum ring will be used for small level of confinement and the steel ring for the highest value.

Gauge positions

The guage positions are determinant to get the highest signal to noise ratio. Numerical simulation was used to determine an optimal position of different strain measurement points. A steel ring subjected to a load of 36 kN is modeled. The hoop strains on the internal and external arc of the ring as function of the angle were exported from Abaqus. The graph is plotted in Figure 3.4.

Since it is not recommended to glue the gauges at 0° or 90° for experimental considerations, the most accurate position is between 20° and 30°. The gauges are then glued at 25° approximately.

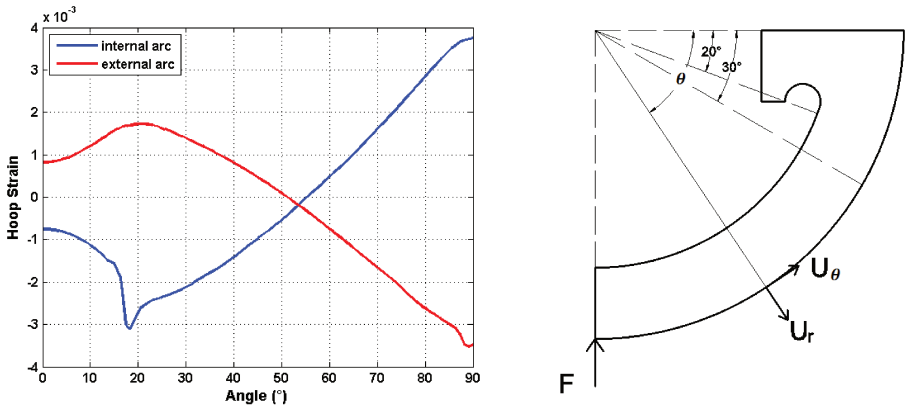

(a) (b)

FIGURE 3.4: (a) Distribution of hoop strain inside the ring (b) Gauge position

3.1.1.2 Relation between the force applied to the ring and the force transferred to concrete

The load applied to the ring is not totally transferred to concrete. Therefore it is necessary to know the relation between the force applied and the force transferred to the specimen. Three cases were studied and modeled in order to determine the rigidity of the system and thus the relation between the two loads. Each case of Figure 3.5 is detailed and then some mathematical relationships can be formulated to combine the three different cases.

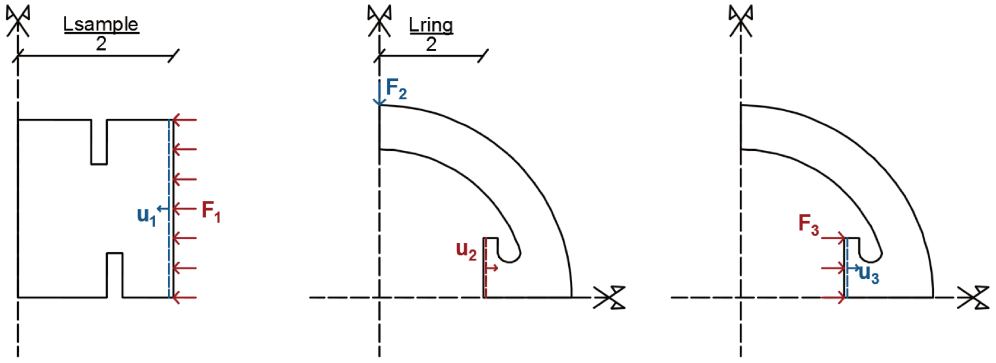

FIGURE 3.5: The rigidity of concrete or ring calculated for different cases

In the first case, a constant displacement u_1 is imposed to the concrete sample. Obtaining the resultant contact force between the concrete and the plate gives the rigidity of concrete K_1. In the second case, a concentrated force is applied on the ring and the displacement of the plate u_2 is calculated as well as the rigidity K_2 of the ring in this configuration of loading. In the third case, a displacement u_3 is imposed on the plate and the force between the ring and the plate as well as the rigidity K_3 can be determined.

Considering the first step of loading, with an applied force F_2 reaching the maximum value:

$$u_2^{max} = \frac{F_2^{max}}{K_2} \tag{3.11}$$

with

$$u_2^{max} + \frac{L_{ring}}{2} = \frac{L_{sample}}{2} \tag{3.12}$$

Now the sample is introduced and the ring and concrete are put in contact:

$$u_{final} = \frac{F_1^{final}}{K_1} = \frac{F_3^{final}}{K_3} \tag{3.13}$$

When the force applied F_2 starts to decrease and F_3 begins to increase:

$$u = u(F_2) + u(F_3) = \frac{F_2}{K_2} + \frac{F_3}{K_3} \tag{3.14}$$

When the force applied F_2 is totally released, F_2=0 :

$$F_{comp} = F_3 = K_3(u_2 - u_3) = K_3(u_2^{max} - u_3) \tag{3.15}$$

and since $F_3 = K_1\ u_1$, we have:

$$F_{comp} = K_3[\frac{F_2^{max}}{K_2} - \frac{F_{comp}}{K_1}]$$

$$F_{comp} = \frac{F_2^{max}}{K_2}[\frac{1}{\frac{1}{K_3} + \frac{1}{K_1}}]$$

$$F_{comp} = \frac{K_1K_3}{(K_1 + K_3)}\frac{F_2^{max}}{K_2} \tag{3.16}$$

Finally we can write,

$$F_{comp} = \alpha F_{applied} \tag{3.17}$$

with

$$\alpha = \frac{K_1K_3}{K_2(K_1 + K_3)} \tag{3.18}$$

If one considers that K_2 and K_3 have approximately the same values, the above relation can be written:

$$\alpha = \frac{K_1}{(K_1 + K_3)} \tag{3.19}$$

From the above relation, one may conclude that on the first hand the force transferred to concrete is smaller than the one applied on the ring and on the other hand in order to increase the value of the force transferred, the rigidity of the ring has to be small compared to the stiffness of the concrete sample in compression.

Numerical applications:

Each of the case described in Figure 3.5 was modeled using Abaqus (Figure 3.6).

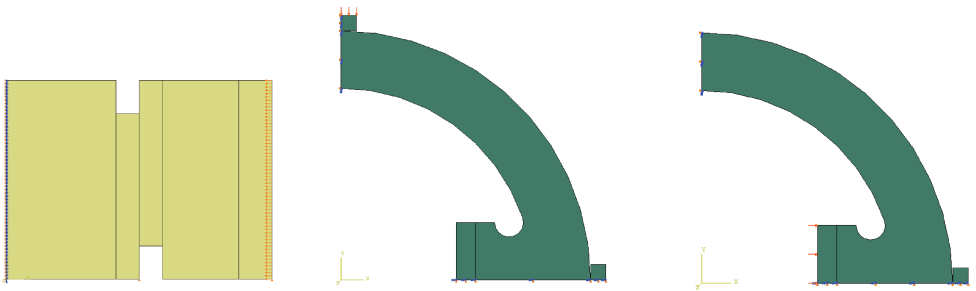

(a) (b) (c)

FIGURE 3.6: Numerical simulations done to calculate the rigidity of the concrete or the ring (Refer to Figure 3.5).

The calculations were made for both aluminum and steel rings modeled with an elasto-plastic behavior (Table 3.1). The Drucker-Prager constitutive model with hardening law was used for concrete to account for dilatant behavior of the specimen (Refer to section 2.2.1.3). The rigidity coefficient obtained for the concrete specimen is equal to K_1=519 MN/m, for the aluminum ring: K_2= 40.2 MN/m , K_3 = 37.4 MN/m which gives α_{aluminum} equal to 0.87 and for the steel ring: K_2= 111.4 MN/m , K_3 = 104 MN/m which gives α_{steel} equal to 0.77 according to equation (3.18).

Characteristics of the confining ring used

Table 3.2 represents the characteristics of the aluminum and steel rings used. The values of the yield strength of each ring is given by the manufacturer, the maximum force that could be applied and the corresponding maximum Mises stress and the force transferred to concrete are obtained from the above numerical simulations.

To verify the analytical solution, a 3D model has been implemented into Abaqus as shown in Figure 3.7. A quarter model was used by imposing two symmetry plans, X and Z planes.

The first suggested sample geometry is a parallelepiped with L=70 mm, B=40 mm and H=40 mm. These dimensions were chosen close to the dimensions of the samples tested

	aluminum	Steel
Yield Strength (MPa)	485	1100
Maximum force applied (kN)	16	36
Maximum Mises stress (MPa)	390	900
Force transfered to concrete (kN)	14	28

TABLE 3.2: Characteristics of metallic rings used

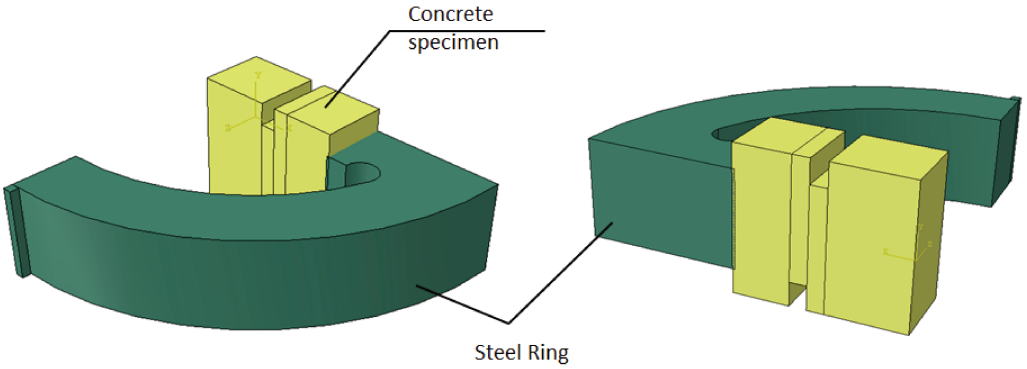

FIGURE 3.7: 3D model for concrete specimen with the ring

with the Giga press. Two notches of 10 mm have been performed in the top and bottom faces of the specimen so the ligament length is H_{lig}=20 mm. Different geometries were studied in the following section in order to obtain the optimal one which gives a more homogeneous stress inside the ligament.

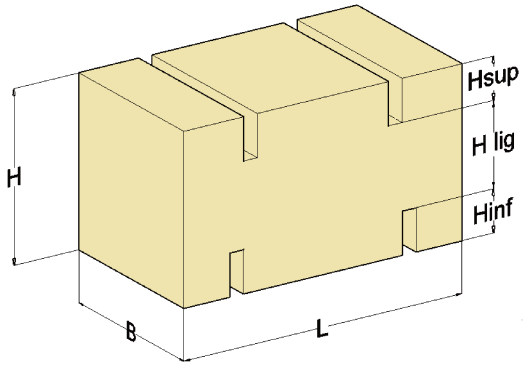

FIGURE 3.8: Dimensions of concrete specimen

Two steps were applied in the model:

- First step: The Force is applied to the ring thus a certain displacement u_2 occurs, the concrete is translated with the same value of u_2 but is not in contact with the ring.

- Second step: The force applied to the ring is released, and an interaction law between the ring and the sample is defined to create the contact.

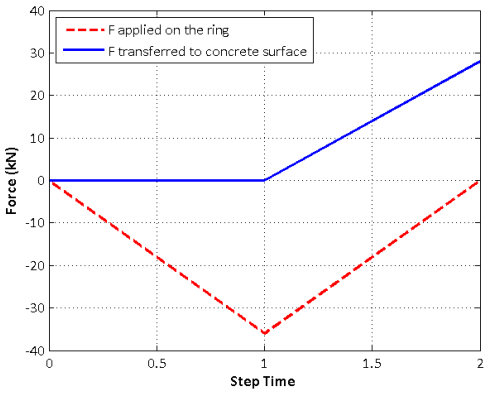

FIGURE 3.9: Results obtained numerically on Abaqus showing the values of the force applied on a steel ring and the compression force transmitted to the concrete sample

The force applied on the ring and the one obtained in the contact between the concrete and the ring during the two time steps are shown in Figure 3.9. We can see that in the first step, a force of 36 kN is applied and the force in the concrete is equal to zero. At the end of the second step, when the force applied is totally released a force of 28 kN is transferred to concrete.

3.1.1.3 Homogeneity of stresses in the ligament

In this section, different geometries of concrete sample were studied in order to obtain a better homogeneity inside the ligament after applying the confinement to the sample. A brief description of each case studied is presented in Table 3.3. A force of 36 kN is applied on a steel ring and the confinement stresses in the sample at the end of loading for the different cases are presented in Figure 3.11.

	L	B	H	H_{lig}	H_{sup}	H_{inf}
Case a	70	40	40	20	10	10
Case b	70	40	30	20	5	5
Case c	70	30	40	20	10	10
Case d	70	30	30	20	5	5

TABLE 3.3: Different geometries studied

Only one quarter of the sample is modeled as shown in Figure 3.10, the ring and the plate have been hidden from the graphs for better display of the stresses distribution on the surface of the concrete specimen.

Furthermore, the confinement stresses along the path drawn in Figure 3.12 for the different cases are presented in Figure 3.13 and Figure 3.14.

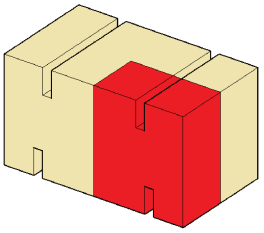

FIGURE 3.10: The quarter sample modeled and shown in Figure 3.11

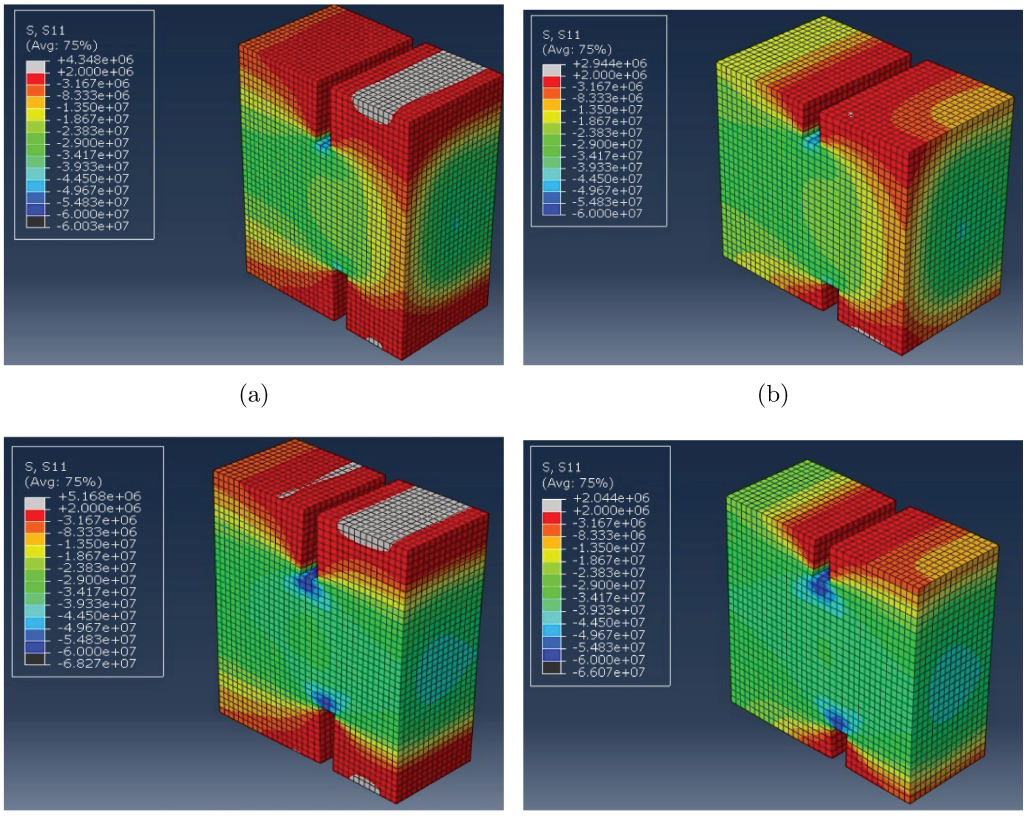

FIGURE 3.11: Distribution of confinement stresses in the concrete sample for different geometries studied detailed in Table 3.3 ($H_{contact}$=H_{lig})

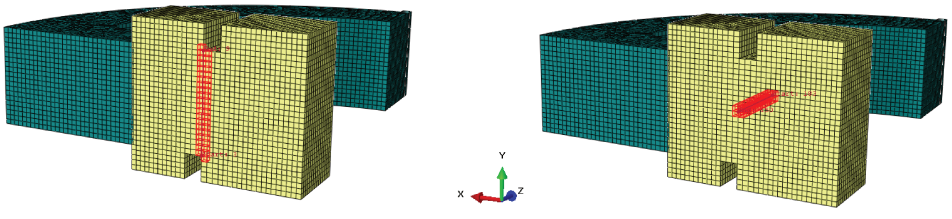

FIGURE 3.12: Path of nodes used to plot the confinement and shear stresses for different geometries (a) Path Y (b) Path Z

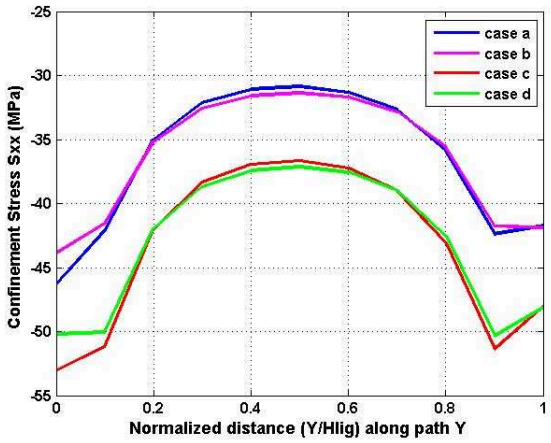

FIGURE 3.13: Variation of the confinement stress σ_{xx} along the path Y (cf. Figure 3.12) as function of its normalized distance for different cases studied as detailed in Table 3.3.

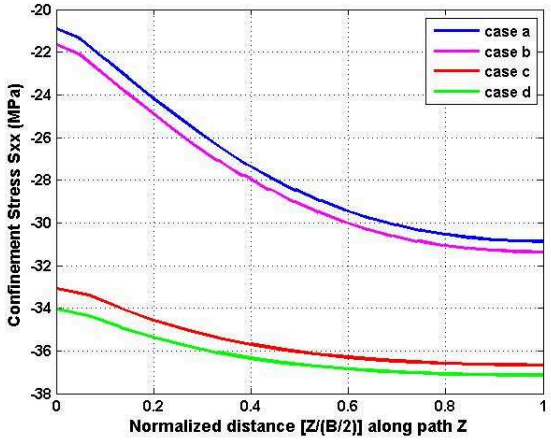

FIGURE 3.14: Variation of the confinement stress σ_{xx} along the path Z (cf. Figure 3.12) as function of its normalized distance for different cases studied as detailed in Table 3.3.

As shown in Figure 3.14, for the cases c and d where the width (B) of concrete is equal to 30 mm, the variation of confinement stress along the ligament is approximately 3 MPa (8%) whereas for the cases where the width is equal to 40 mm, the confinement varies from 21 MPa at the surface of the specimen to 31 MPa inside the sample (29%).

One can conclude that in order to obtain a better homogeneity of confinement stress in the concrete sample, the width B of concrete should be equal to 30 mm, the height equal to 30 mm with a ligament height equal to 20 mm. This ligament length is equal to the contact length between the ring and the concrete sample ($H_{contact}$=H_{lig}). One should also note that for smaller ligament section, higher stresses for the same applied load are obtained. Hence, a width and a height equal to 30 mm are more desirable in terms of stress homogeneity and amplitude.

3.1.1.4 Final Punching-Through Shear test configuration

To summarize, different geometries of the ring and of the concrete sample were simulated in order to choose the optimal dimensions. The final geometry chosen for the ring is shown in Figure 3.15 and the one for the concrete sample in Figure 3.16

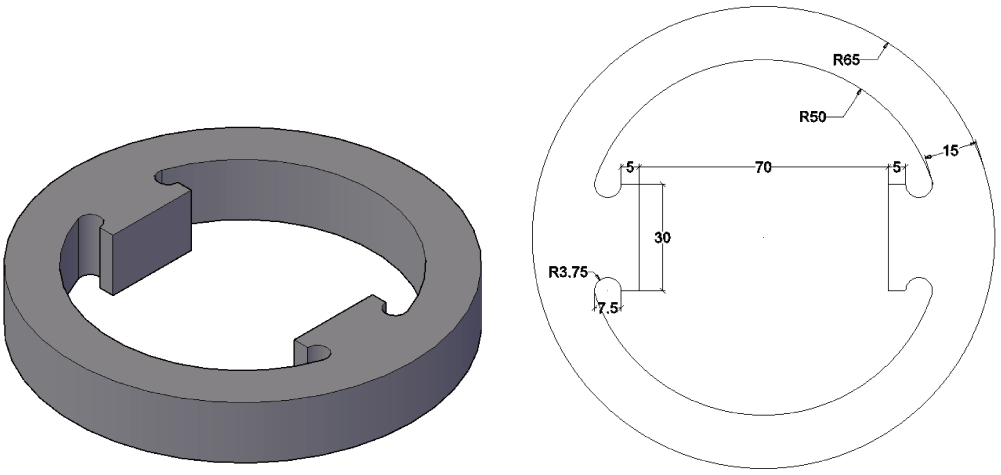

(a) (b)

FIGURE 3.15: Ring geometry and dimensions (in mm)

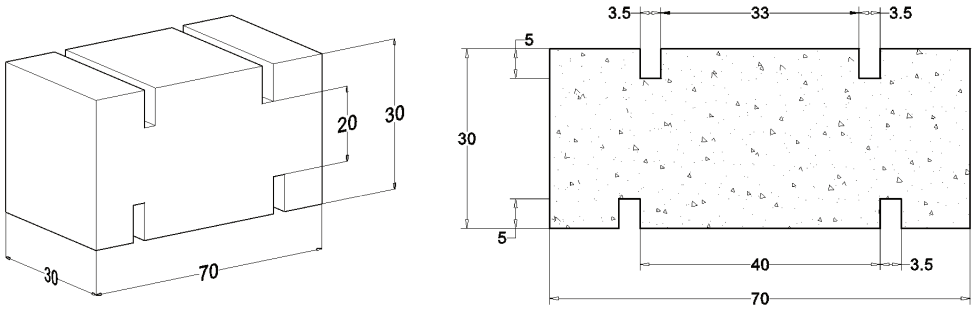

(a) (b)

FIGURE 3.16: Concrete sample geometry and dimensions (in mm)

3.1.2 Simulations of static shear testing

In this section, quasi-static punching through shear test was modeled with Abaqus. The same geometry and materials used in the above sections are applied. The loading in the first two steps was also similar to previous calculations. A new step of loading was added in which the displacement of the outer bottom part of the specimen is fixed in the Y direction and a velocity is applied to the central upper part in the same direction. The applied loading is shown in Figure 3.17

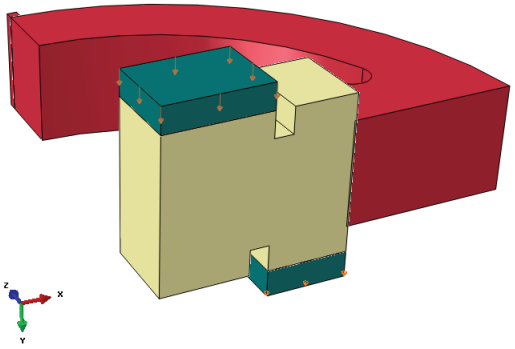

FIGURE 3.17: Loading applied in the static shear loading step

These 3D computations allowed checking the homogeneity of the stress field in the shear zone. The average shear stress in the ligament of concrete is around 35 MPa.

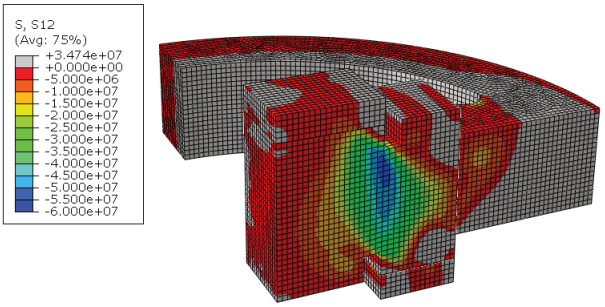

FIGURE 3.18: Shear stresses inside concrete sample under static shear loading after 0.5 mm of displacement

The shear and confinement stresses at the peak of shear stress (0.5 mm of displacement) along the two paths (shown in Figure 3.12) are plotted in Figure 3.19. The shear stress varies from 35 MPa to 55 MPa along the path Y and from 18 MPa to 48 MPa along path Z with an average of 38 MPa in the total shear surface.

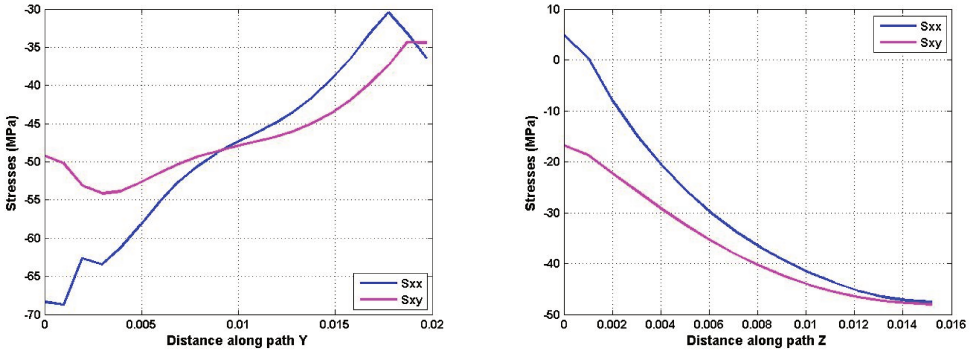

(a) (b)

FIGURE 3.19: Shear and confinement stresses in the ligament after 0.5 mm of displacement along the two paths defined in Figure 3.12

3.1.3 Simulations of dynamic shear testing

Dynamic shear tests were simulated using Abaqus/Explicit in order to verify the dynamic stress equilibrium in the concrete specimen.

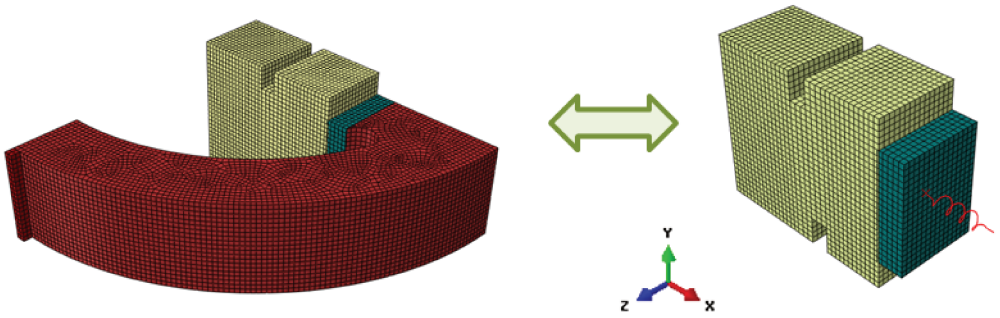

FIGURE 3.20: Mesh used in the case of a ring or a spring

Before simulating shear testing and in order to reduce the calculation time in dynamic simulations, the ring was modeled as a spring. The plate is modeled as a rigid body; the reference point of the plate is in the center of mass of the plate. This reference point is fixed in all directions except the x axis to assure the translation of the plate. To this plate is assigned a spring of a stiffness equal to the one of the ring. The second end of the spring is restrained in all directions.

In the first step of calculation, the spring is pre-confined by applying a uniform pressure on the plate with the aim to attain the same value of plate displacement reached when the ring is subjected to a certain loading. In the second step, the force applied on the plate is released and an interaction between the plate and concrete sample is created. We should note that, in the initial step (similar to the case of the ring), the concrete should be translated for the same value of displacement so that in the beginning of the second step, the concrete and the plate are in contact.

Same loading conditions were applied and it was deduced that the same contact forces and same displacements were obtained when replacing the ring by a spring. The calculation time was significantly reduced and some differences between the two calculations are listed in table below.

The mesh of the dynamic PTS setup is shown in Fihure 3.21(a) and the dimensions of the different elements presented in the simulation are presented in Table 3.5.

Because it is difficult to simulate the pulse shaper, an incident pulse obtained with previous experiments (Lukić and Forquin [2015]) was applied to the front face of the

	Ring	Spring
Number of elements	52400	16801
Number of nodes	59473	19554
Number of increments	118716	28743
Stable time increment	$5.89*10^{-8}$	$2.43*10^{-7}$

TABLE 3.4: Difference between calculations made with a ring and a spring

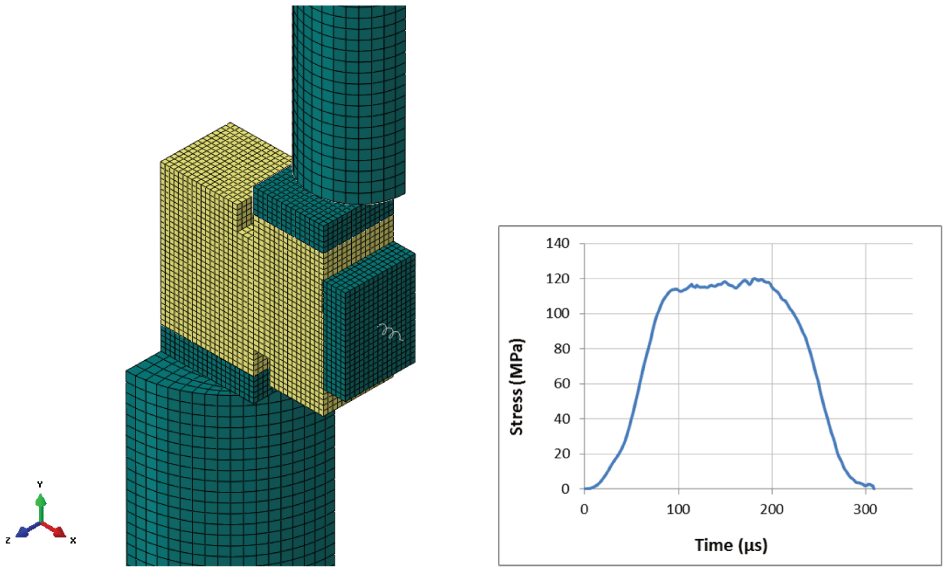

(a) (b)

FIGURE 3.21: (a) Numerical 3D mesh for dynamic PTS setup (b) Incident pulse applied to the input bar in dynamic numerical simulations

	X	Y	Z
Input Bar	R=22.5	1500	R=22.5
Intermediate input plate	20	5	15
Concrete Specimen	35	30	15
Confinement plate	5	20	15
Intermediate output plate	15	5	15
Output Bar	D=20	1000	R=10

TABLE 3.5: Dimensions of the different parts of the 3D dynamic PTS model (according to frame orientation given in Figure 3.21).

incident bar. This pulse was obtained with a projectile launched at 17.7 m/s (which generates a stress of 120 MPa) and with a pulse shaping technique. It is characterized by a long rising time to reduce unwanted inertial effects and correct the mechanical balance of the specimen (Figure 3.21(b)).

The shear stresses deduced from the input and output forces on the contact between the concrete sample and the bars as well as the average shear stress obtained in the ligament of the sample are compared in Figure 3.22. It is observed that the shear stress deduced from both input and output forces are fairly close indicating that the

mechanical equilibrium of the sample was met up to the peak load. Moreover, the shear stress obtained by processing the contact forces is very close to the true stress obtained from the shear ligament.

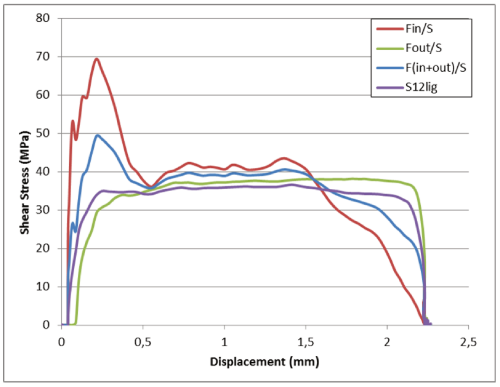

FIGURE 3.22: Comparison of the stresses deduced at the specimen/bars interfaces with the stress calculated in the ligament

In conclusion, these numerical simulations were used to improve the test processing and to validate the experimental setup. They demonstrated the need of using a pulse shaper system between the impactor and the incident bar. The inertial effects are reduced and the specimen is assumed to be in equilibrium and hence the shear stress is calculated by averaging the input and output forces.

3.2 Experimental method

3.2.1 Sample preparation

Concrete is casted in parallelepiped molds with batch volumes of 13.5 L. The block, upon removal from the mold 24 h after casting, is stored for 28 days in a saturated environment within plastic bags immersed in water, so as to insulate the concrete both physically and thermally.

Rectangular blocks are cut out of the large blocks, their surface are ground in order to ensure a homogeneous distribution of stresses during loading. The defect in parallelism of two samples faces should be less than 0.05 mm. The blocks are then cut to obtain the required rectangular sample with the saw machine. Afterwards, notches are drilled with precision in order to obtain the final Punch-Through shear test specimen. All these steps are done with water to prevent specimens and tools from overheating. The machining process is shown in Figure 3.23. After machining, wet samples are replaced in water and dry specimens are oven dried at 60°C.

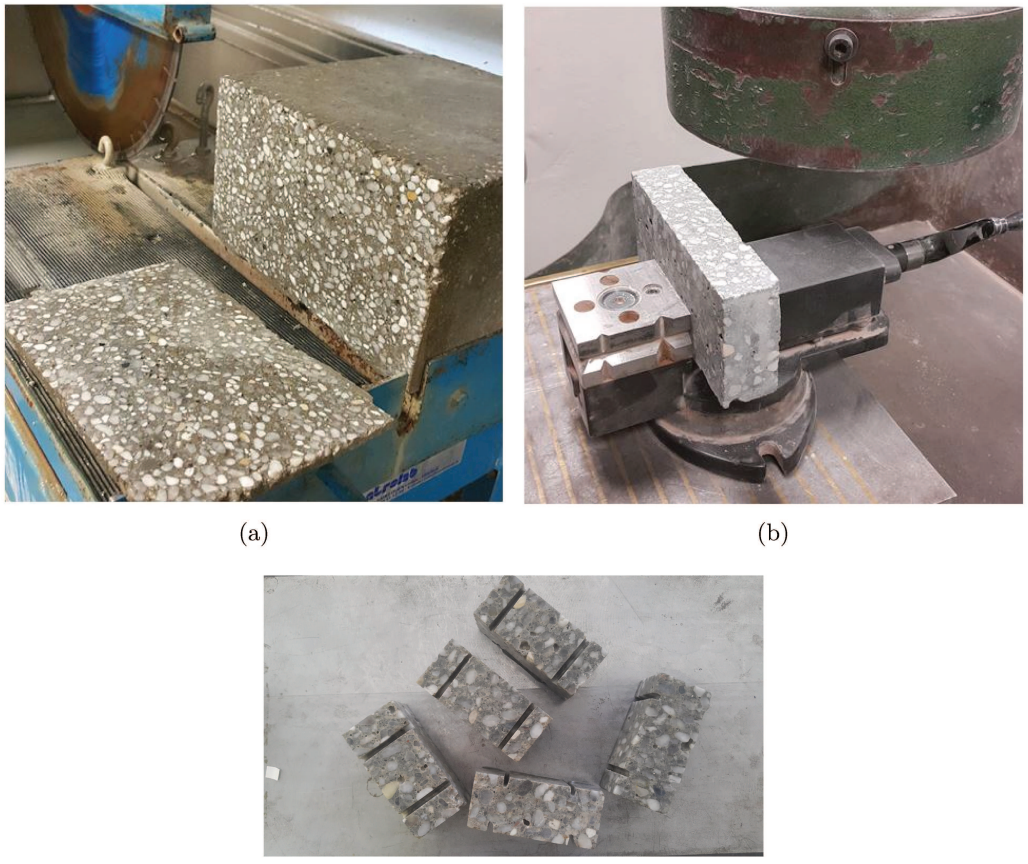

(a) (b)

(c)

FIGURE 3.23: Procedure for preparation of concrete samples

3.2.2 Signal measurement

The signal measurement chain is based on the following elements:

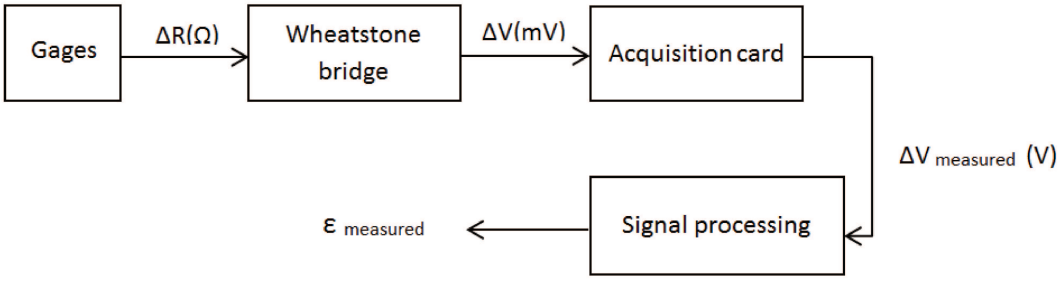

FIGURE 3.24: Signal measurement technique

3.2.3 Strain gauges configuration

Two types of strain gauge configurations were used: quarter-bridge for the ring gauges and full-bridge for the bars. These configurations are based on the concept of a Wheatstone bridge. A description of the Wheatstone bridge as well as the relation between the voltage measured and the gauge deformation are detailed in Appendix B.

3.2.3.1 Quarter-bridge configuration

An expression for the strain gauge as a function of the measured voltage in a quarter bridge configuration is given by:

$$\varepsilon = \frac{4}{K.G.V_{EX}} \Delta V_{measured} \tag{3.20}$$

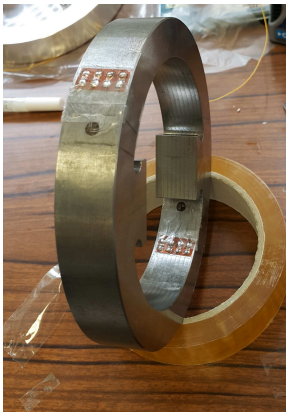

FIGURE 3.25: The aluminum ring instrumented with the gauges

Four gauges in a quarter-bridge configuration were glued on the rings in order to measure the hoop strain during tests. The gauges used for the aluminum ring are the FCA-1-23, gauges of 1 mm length and which has a temperature compensation of 23. The ones used for the steel are the FCA-2-17 with 2 mm length and a compensation factor of 17. For this gauges, an amplifier gain G=2000 and an excitation voltage of 1V are used.

3.2.3.2 Full-bridge configuration

The gauges used on the Hopkinson bars are used in sets, consisting of a transverse gauge and a longitudinal gauge. At a measuring point there are two sets of diametrically opposed gauges which are mounted as a Full Wheatstone bridge.

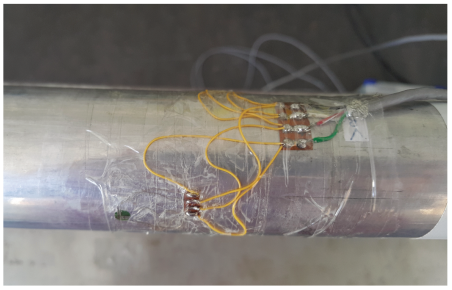

(a)

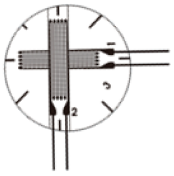

Set of two gages

(b)

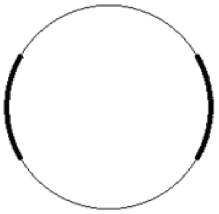

Sets diametrically opposed

(c)

FIGURE 3.26: Layout of gauges on the bars

The relation between the voltage measured and the strain gauge deformation is the following:

$$\varepsilon = [\frac{2}{V_{EX}.k.G.(1+\nu)}].\Delta V_{measured} \tag{3.21}$$

3.2.4 Calibration of the ring's gauges

The Schenck press was used to apply the confinement to the specimens. It is a hydraulic press able to generate a displacement with a velocity smaller than 20 mm/s. This press has a very precise force sensor and is also equipped with a displacement sensor installed in the axial jack which allows controlling the loading during a test. The desired applied force being calculated numerically, the tests are driven with imposed force. The gauge deformation occurs due to two major forces and thus has to be calibrated and a relation between the gauge deformation with the applied force F1 and the transmitted force F2 should be concluded (Figure 3.27(a)).

In order to proceed to the calibration, two different setups were studied. They consist of applying certain forces F1 and F2 in two different directions as shown in Figure 3.27(a) and in measuring the deformation of the gauges as function of the force applied.

Numerical simulations were done to study the deformation of the ring when applying the force F_2 from inside (Figure 3.27(b)) or from outside the ring (Figure 3.27(c)) and it was

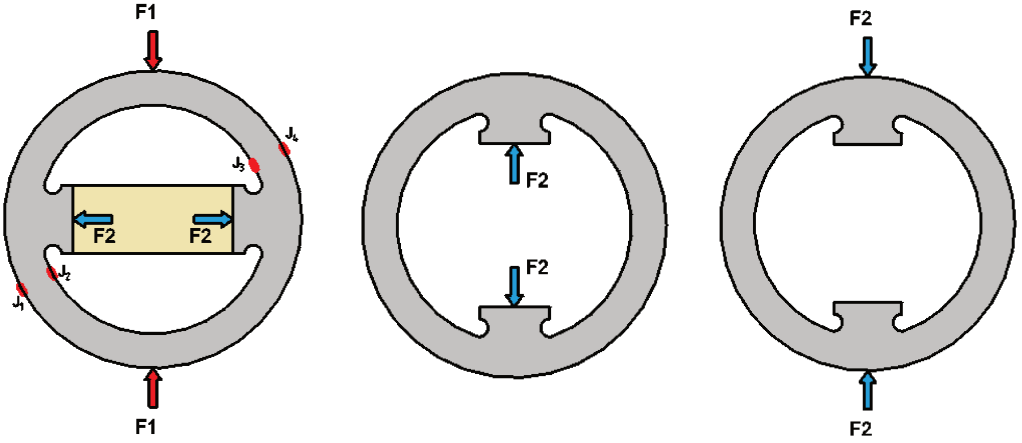

(a) (b) (c)

FIGURE 3.27: A scheme representing the ring, the position of the gauges and the forces applied to calibrate the gauges

concluded that wherever the force F_2 is applied we obtain the same gauge deformations. Therefore, in our experiments and for the sake of simplicity, the force F_2 was applied from outside the ring (Figure 3.28(b)).

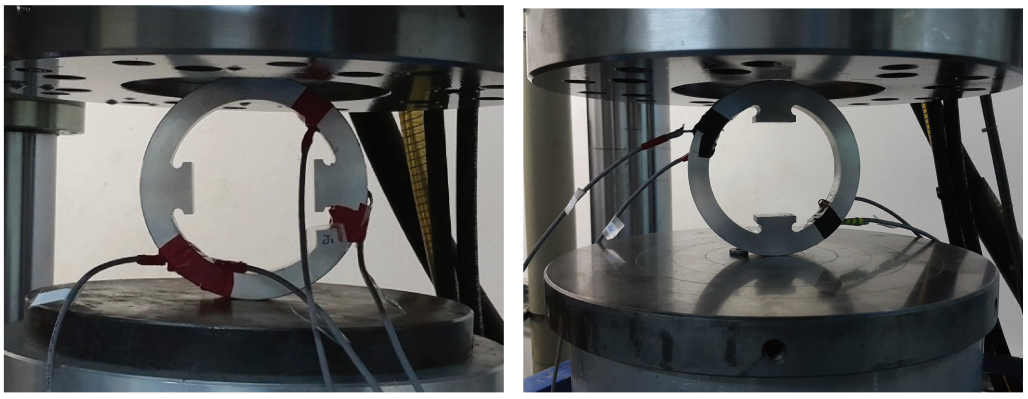

(a) (b)

FIGURE 3.28: The configurations of the forces applied for the calibration of the gauges (a)F1 applied (b)F2 applied

For each gauge glued on the ring, the graphs representing each force F_1 and F_2 as function of the gauge deformation are plotted in Figure 3.29 and the slope of the curve is calculated so the final relation for each gauge is established as in this following equation:

$$\varepsilon_{Ji} = \alpha_{Ji} F_1 + \beta_{Ji} F_2 \tag{3.22}$$

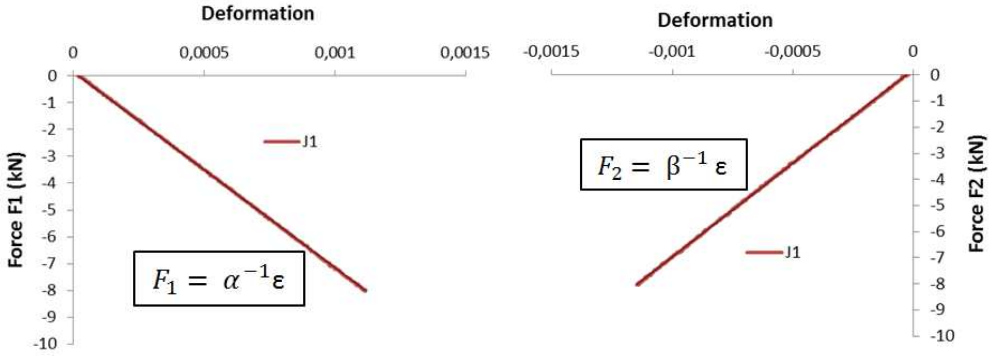

(a) (b)

FIGURE 3.29: Deformation of the ring (measured by the gauge J_1) as function of the applied force

For each of the two rings and the four gauges, the coefficients α and β are calculated and shown in Table 3.6.

	aluminum	Steel
α_{J1}	-0.000138	-0.0000451
α_{J2}	0.000212	0.000071
α_{J3}	0.000208	0.000021
α_{J4}	-0.000057	-0.0000477

	aluminum	Steel
β_{J1}	0.000139	0.000047
β_{J2}	-0.00014	-0.000048
β_{J3}	-0.00014	-0.000014
β_{J4}	0.00006	0.000051

TABLE 3.6: Coefficients of each gauge used to calculate the confinement pressure

3.2.5 Confinement of concrete

As mentioned in section 3.1.1, the confinement consists of pre-stressing a metallic ring by applying a compressive load. The concrete specimen is then inserted inside the ring and the load is released, so a confinement is applied to the concrete sample. Steel sheets are incorporated between the ring and the concrete sample in order to fill the gap between them and thus obtain different levels of confinement.
The relation between the force and gauges deformation being known, one can calculate the compression force transferred to concrete by checking the deformation of the gauges at the end of the unloading phase. For instance, if a certain level of confinement is required, the corresponding deformation can be calculated ($\varepsilon_{Ji} = \beta_{Ji}\ F_2$, β_{Ji} being known).

Aan example of 11 kN of compression force (8 MPa of confinement) applied with an aluminum ring is plotted in Figure 3.31(a)

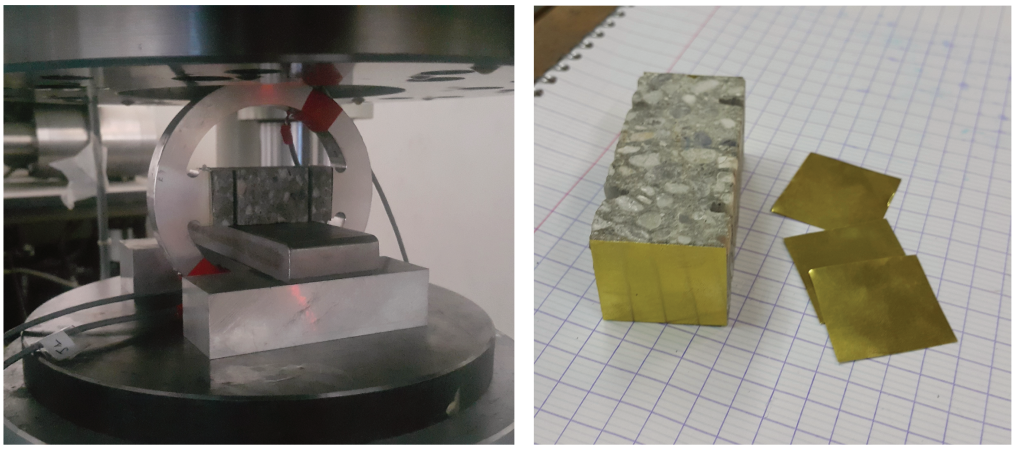

(a) (b)

FIGURE 3.30: Procedure of confinement (a) Method used (b) Steel sheets glued

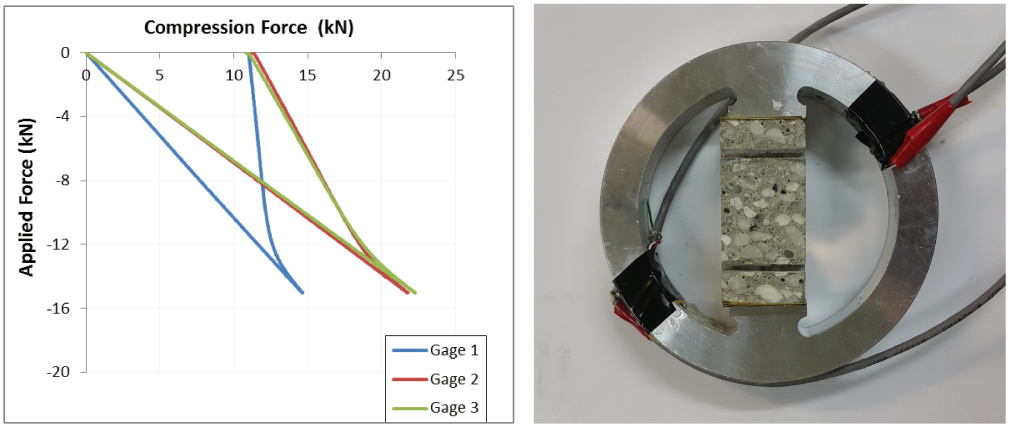

(a) (b)

FIGURE 3.31: (a) The evolution of the forces for a confinement of 11 kN (b) A concrete specimen confined with the ring

3.3 Static tests

3.3.1 Experimental procedure

Quasi-static shear tests were done with the Schenck press and were controlled in displacement with a velocity of 0.003 mm/s. The nominal strain rate is calculated using equation (2.10) with e (the notch width) is equal to 3.5 mm. This corresponds to a nominal strain rate approximately equal to $5x10^{-4}$ /s.

A compression cylinder was used to apply the axial loading and intermediate rectangular supports were used between the specimen and the plate of the press allowing the vertical displacement of the central part. The specimen was instrumented with an LVDT to

measure the axial displacement of the central part. The schematic representation of quasi-static shear tests is shown in Figure 3.32.

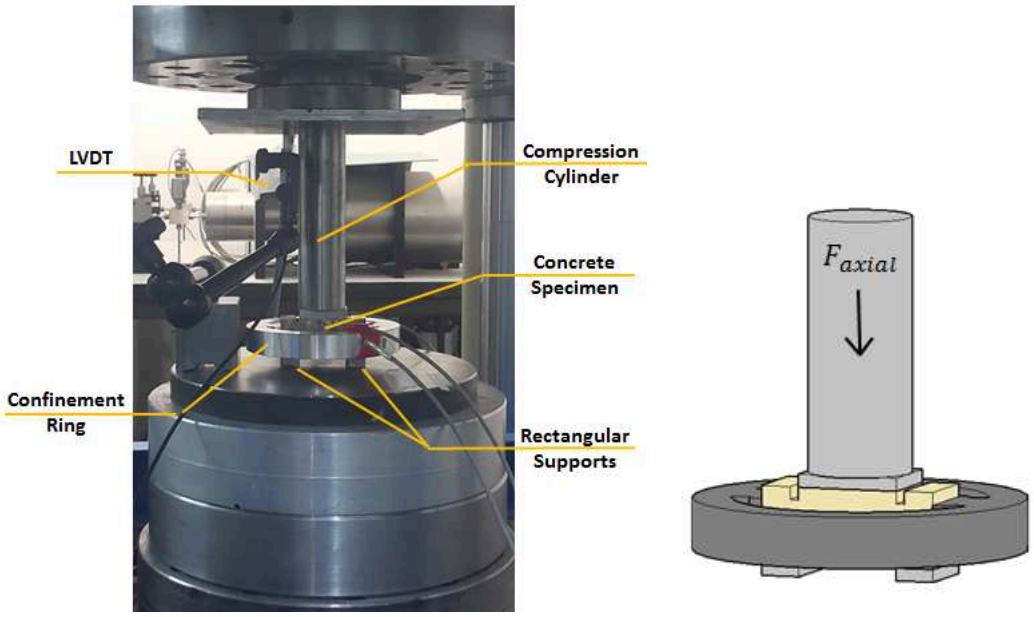

(a) (b)

FIGURE 3.32: Schematic representation of the static Punch-through shear tests

3.3.2 Determination of radial and shear stresses

During the tests, concrete exerts a certain force on the ring which deforms; this deformation is measured by the gauges. Using the processing technique described in section 3.2.5, one can deduce the variation of radial stresses during the test.

On the other hand, shear stresses are calculated by dividing the axial force measured by the press by the shear surface.

$$\sigma_{shear} = \frac{F_{axial}}{S_{ligament}} \tag{3.23}$$

where

$$S_{ligament} = 2.B.H_{lig} \tag{3.24}$$

3.3.3 Quasi-static tests results

Table 3.7 summarizes all static shear tests performed in this study and which will be discussed in the following sections. The table includes the name of each test, the type of the ring used to apply the confinement and the type of material tested. In addition, it

includes the strain-rate calculated from equation (2.10), the level of confinement pressure at the peak of the shear stress as well as the peak shear stress in the ligament. The composition of the concrete tested is presented in section 2.6.1.

Test Name	Ring used	Concrete Sample	Strain rate (/s)	Confinement stress (MPa)	Shear stress (MPa)
ShearStat01	Alu	R30A7	$5x10^{-4}$	19	24
ShearStat02	Alu	Wet R30A7	$5x10^{-4}$	14	18
ShearStat03	Steel	Dry R30A7	$5x10^{-4}$	25	33
ShearStat04	Steel	Wet BHP	$5x10^{-4}$	42	55
ShearStat05	Steel	Wet R30A7	$5x10^{-4}$	20	22
ShearStat06	Steel	Dry R30A7	$5x10^{-4}$	25	33
ShearStat07	Steel	Wet BHP	$5x10^{-4}$	44	65
ShearStat08	Steel	Wet R30A7	$5x10^{-4}$	18	18
ShearStat09	Alu	Wet R30A7	$5x10^{-4}$	11	19
ShearStat10	Alu	Dry R30A7	$5x10^{-4}$	12	25
ShearStat11	Alu	Wet BHP	$5x10^{-4}$	14	37
ShearStat12	Alu	Wet BHP	$5x10^{-4}$	20	42
ShearStat13	Alu	Dry R30A7	$5x10^{-4}$	16	21
ShearStat14	Alu	Wet R30A7	$5x10^{-4}$	15	19

TABLE 3.7: Summary of the different quasi-static shear tests performed

3.3.3.1 Repeatability of tests

Some tests were performed twice to check the repeatability. For both tests, a good agreement between the two sets of results was noticed. Figure 3.33 shows two tests done on the same concrete with the same confining level. Same shear strength and mean confining stress were obtained for both tests in particular until the peak shear stress was reached.

3.3.3.2 Influence of confinement

To study the influence of confinement, experiments were carried out with both confining ring, aluminum and steel. A comparison of shear tests performed with dry samples is presented in Figure 3.34.

For the static shear test done with an aluminum ring, the confinement stress is approximately equal to 9 MPa at the beginning of the test and increases to reach 14 MPa at the peak of the shear stress. With the steel ring, the initial confinement is around 20 MPa and increases up to 25 MPa. For these different confining stresses, we can notice a

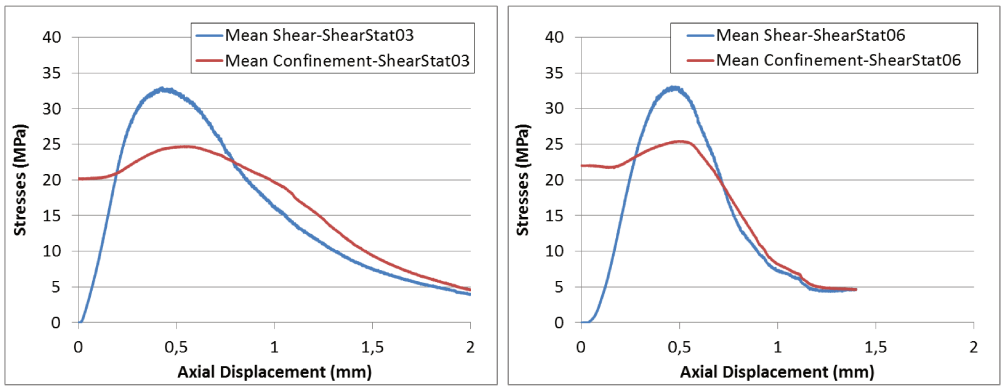

(a) (b)

FIGURE 3.33: Results of quasi-static shear tests performed on dry R30A7 concrete with a steel ring at the same confining level (a)Shearstat03 (b)Shearstat06

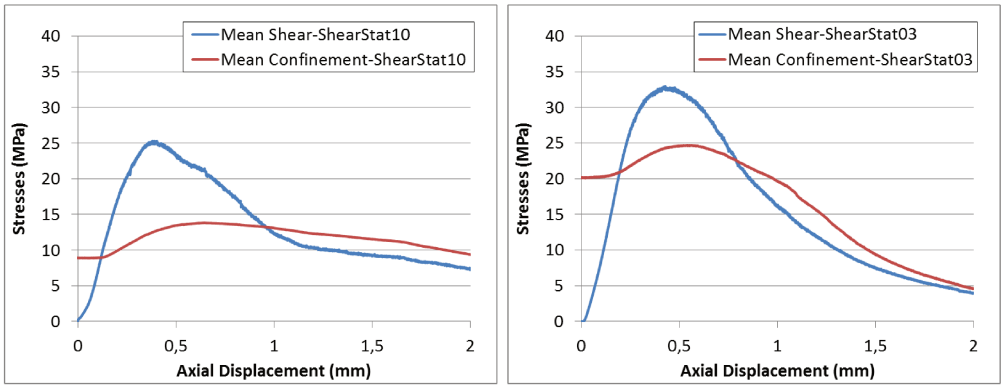

(a) (b)

FIGURE 3.34: Results of quasi-static shear tests performed on dry R30A7concrete with (a) aluminum and (b) steel confining cells

difference in shear strength, *i.e.* 25 MPa for the aluminum ring and 33 MPa for the steel one. Therefore by changing the stiffness of the ring and thus the confinement in concrete, we can notice the variation of shear stress and conclude that concrete is pressure sensitive under shear loading.

3.3.3.3 Influence of moisture content

To study the influence of moisture contents, experimental results obtained with dry and wet specimens in quasi-static loading with an aluminum alloy confining ring are reported on Figure 3.35.

For approximately the same confinement level, the maximum shear stress reached in wet specimen was 19 MPa while on the other hand, the dry sample exhibited higher shear strength of about 25 MPa.

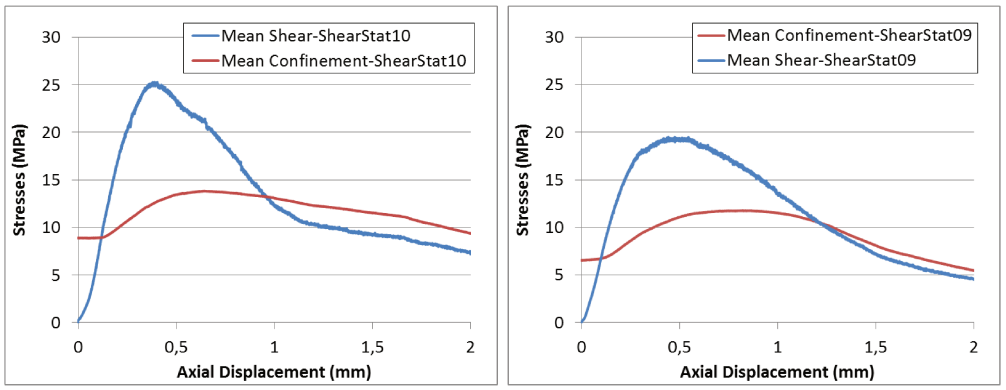

(a) (b)

FIGURE 3.35: Results of quasi-static shear tests performed with an aluminum ring on (a) dry and (b) wet R30A7 concrete specimens

3.3.3.4 Influence of concrete composition

Experimental tests were done with ordinary concrete R30A7 and high preformance concrete HPC to study the influence of concrete composition. Results of quasi-static tests with an aluminum alloy confining ring are reported on Figure 3.36.

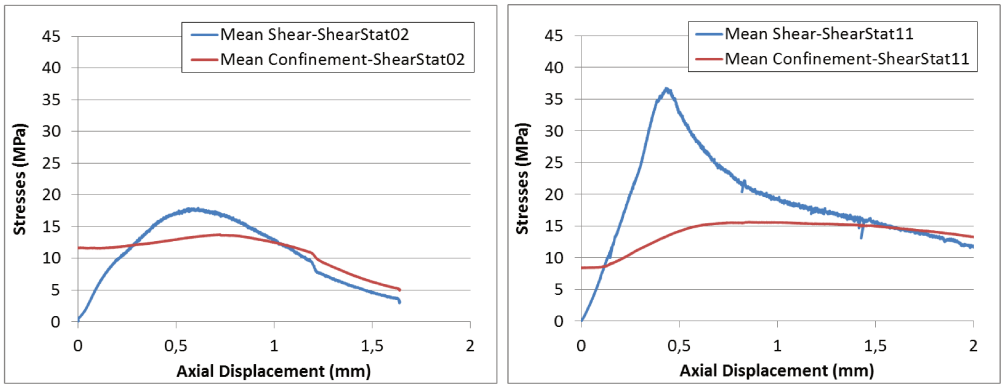

(a) (b)

FIGURE 3.36: Results of quasi-static shear tests performed with an aluminum ring on (a) OC and (b) HPC

In the two tests, the confinement stress reached around 15 MPa at the peak of shear stress. If we compare shear stresses for both concretes, we can notice a level of 18 MPa for the ordinary concrete and double stress (around 36 MPa) for the high performance concrete. This difference can be explained by the decrease in porosity in HPC which leads to higher density and therefore to an increase in shear strength.

3.3.3.5 Post-mortem observation

Videos and pictures were taken during the static testing in order to follow the development of visible surface cracks. The propagation of crack will be presented for the test called 'shearstat06' at different stages of loading (Figure 3.38).

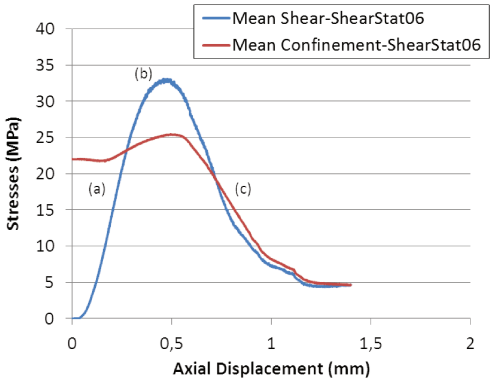

(a)

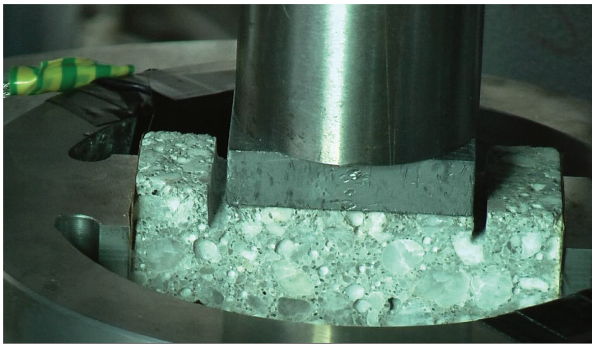

(b)

FIGURE 3.37: (a) Location of pictures taken for 'Shearstat06' test (b) View of the sample before testing

It was noticed that there is a main planar shear fracture that connects the two notches from each side of the specimen, this fracture corresponds to the expected Mode II fracture which was initiated at the peak of loading (Figure 3.38(b)).

Moreover, notches made in this test configuration introduce stress concentrations in the sample where crack growth will initiate. So, in parallel to mode II fracture, wing cracks were created (Figure 3.38(c)) at the inner notch of the loaded part of the specimen. These cracks were not observed before the peak and seem to appear after the peak. Since only the surface of the sample can be seen, it is difficult to know if these cracks were initiated before or after the peak in the core of concrete. Watkins [1983] and Backers et al. [2002] stated that these cracks initiate before the peak but stop and don't influence the principle mode II fracturing.

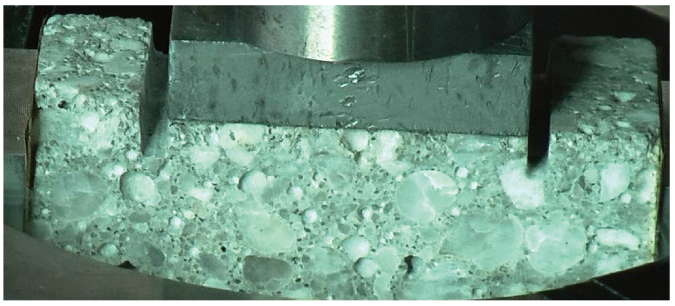

(a)

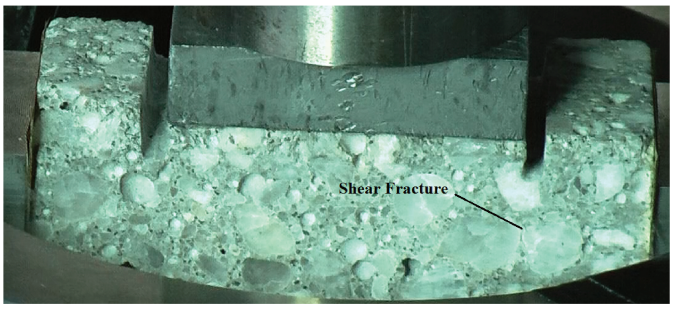

(b)

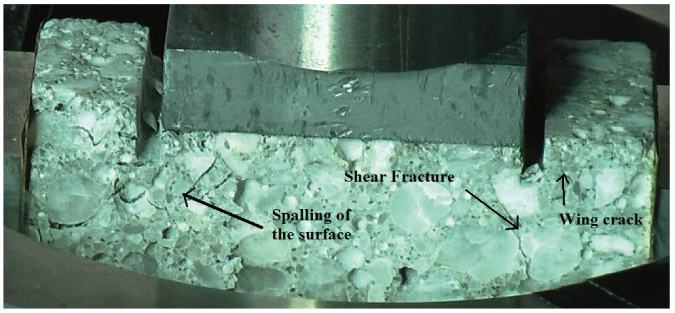

(c)

FIGURE 3.38: Fracturing on the surface of a concrete sample (Shearstat06) at different stages of static loading (Figure 3.37(a)).

Furthermore, since the test has a rectangular rather than cylindrical geometry and biaxial rather than triaxial loading, the front and the back of the sample are not confined, surface spalling parallel to the free surface occurs because of dilatancy effect and thus some fragmentation of the concrete happens near the surface of the sample.

On the other hand, it can be seen that the cracks produced inside the sample tend to circumvent the siliceous aggregates as it was noticed in unconfined compression tests and triaxial tests in Piotrowska et al. [2014].

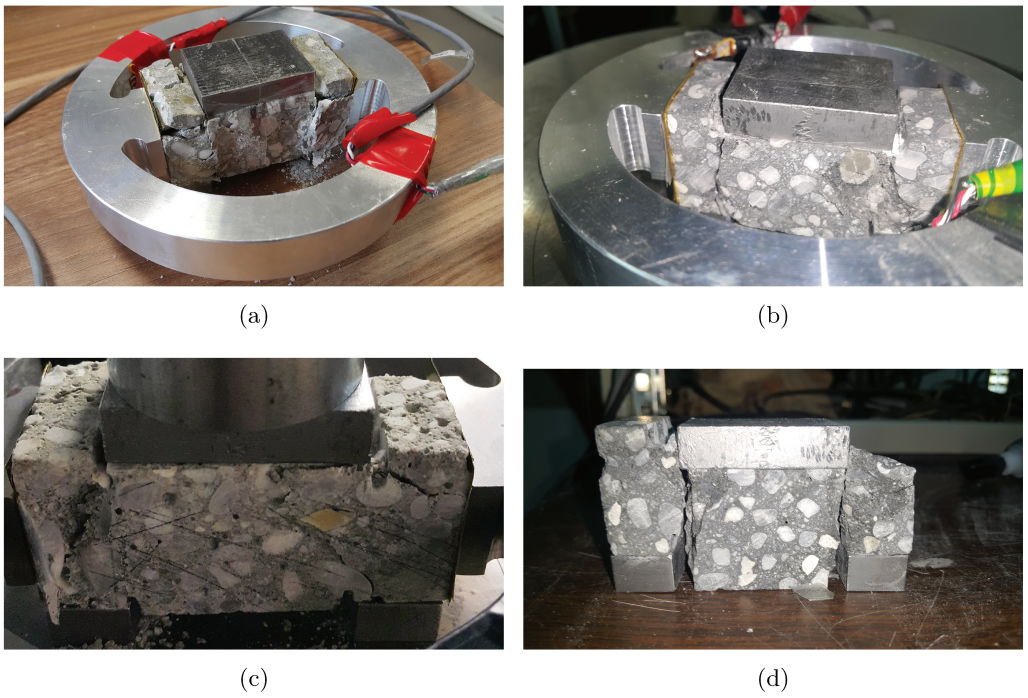

(a) (b)

(c) (d)

FIGURE 3.39: Crack pattern for different static tests (a) Shearstat01 (b) Shearstat11 (c) Shearstat06 (d) Shearstat12

3.4 Dynamic tests

3.4.1 Split Hopkinson Pressure Bar Technique

The dynamic loading is applied to the specimen through Split Hopkinson bar apparatus. It is composed of a striker bar of 480 mm in length and 45 mm in diameter, an incident bar of 1500 mm in length and 45 mm in diameter made of high-strength aluminum alloy and two output bars of 1200 mm in length and 20 mm in diameter. The cylindrical input and output bars are instrumented with strain-gauges which allow to obtain reliable records of the stress pulses. A pulse shaper technique is used in order to get a force balance in the specimen. A thin disk of lead is attached on the impact end of the incident bar and generates an incident wave characterized by a slightly longer rising time. The experimental setup is schematically shown in Figure 3.40.

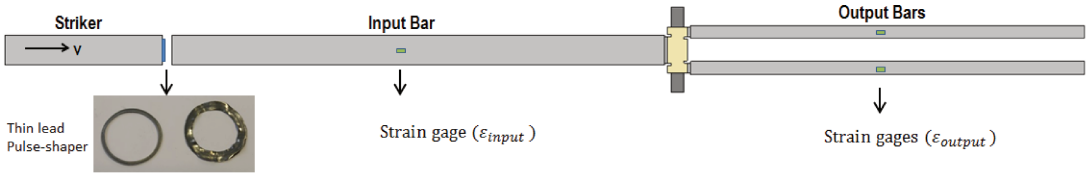

FIGURE 3.40: Schematic representation of the SPHB system for dynamic Punch-through shear tests

Based on the strains measured in the bars and according to the one dimensional wave theory, forces and particles velocities at the bar/specimen interfaces can be calculated.

3.4.2 Processing technique

The forces and particles velocities at the specimen faces are calculated by shifting the waves to the contact surfaces assuming that no wave dispersion occurs in slender elastic bars. If $\varepsilon_{\text{incident}}$, $\varepsilon_{\text{reflected}}$ and $\varepsilon_{\text{transmitted}}$ represent the shifted incident, reflected and transmitted waves respectively, the forces and velocities at the contact surfaces can be calculated as follows:

$$F_{input} = -S_{input} E_{bar} (\varepsilon_{incident} + \varepsilon_{reflected}) \tag{3.25}$$

$$F_{output} = -S_{output} E_{bar} \varepsilon_{transmitted} \tag{3.26}$$

$$V_{input} = -C_{bar} (\varepsilon_{incident} - \varepsilon_{reflected}) \tag{3.27}$$

$$V_{output} = -C_{bar} \varepsilon_{transmitted} \tag{3.28}$$

$\varepsilon_{\text{incident}}$, $\varepsilon_{\text{transmitted}}$ being negative and $\varepsilon_{\text{reflected}}$ being positive, the shear stress in the ligament is obtained by averaging the input and output forces divided by the section of the ligament:

$$\sigma_{shear} = \frac{F_{input} + F_{output}}{2.S_{ligament}} \tag{3.29}$$

The axial displacement is then deduced by integrating the axial velocity obtained as follows:

$$V_{axial} = V_{input} - V_{output} \tag{3.30}$$

This processing technique was applied to a series of dynamic experiments performed on different types of concrete specimens. Experimental results are presented hereafter.

3.4.3 Pulse-shaper technique

The use of a pulse shaper technique increases the rising time of the incident wave and reduces the inertial effects which can lead to a force equilibrium at both sides of the concrete sample and a more constant strain-rate during loading. Thus, a thin lead pulse-shaper with the geometry shown in Figure 3.41 is mounted on the impact end of the incident bar. It has an internal diameter of 36 mm and an external of 42 mm with a thickness of 0.8 mm. This system made possible to considerably lengthen the rising

time without significantly modifying the total duration of the incident pulse. For these reasons, the following experimental tests could be analyzed by considering equation (3.29).

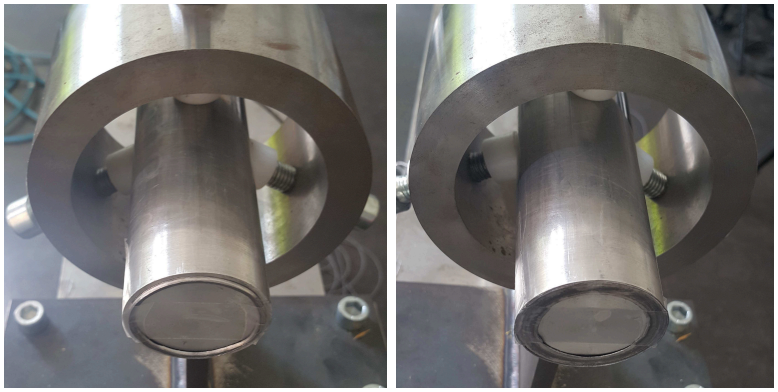

(a) (b)

FIGURE 3.41: Thin disk of lead used as pulse shaper between the projectile and the incident bar (a) Before dynamic testing and (b) After dynamic testing

3.4.4 Dynamic tests results

Test Name	Ring used	Concrete sample	Projectile velocity (m/s)	Srain rate (/s)	Confinement stress (MPa)	Shear stress (MPa)
ShearDyn01	aluminum	Wet R30A7	-	-	-	-
ShearDyn02	aluminum	Wet R30A7	-	-	-	-
ShearDyn03	aluminum	Wet R30A7	9.45	30.7	15	33
ShearDyn04	aluminum	Wet R30A7	9.37	27.1	16	30
ShearDyn05	aluminum	Wet R30A7	8.9	30.9	16	31
ShearDyn06	aluminum	Dry R30A7	8.75	46.5	18	37
ShearDyn07	aluminum	Dry R30A7	8.4	28.7	15	30
ShearDyn08	aluminum	Wet HPC	9.2	65.7	18	60
ShearDyn09	aluminum	Wet HPC	8.75	48.4	10	44
ShearDyn10	aluminum	Wet R30A7	8.5	44.5	10	32
ShearDyn11	Steel	Dry R30A7	9.2	49	27	45
ShearDyn12	Steel	Wet R30A7	8.95	41.8	25	38
ShearDyn13	Steel	Wet HPC	9.1	81.7	40	70
ShearDyn14	Steel	Dry R30A7	8.7	42.5	25	36
ShearDyn15	Steel	Wet HPC	9.4	85.1	36	68

TABLE 3.8: Characteristics of dynamic shear tests done

In total, fifteen tests were done with the Hopkinson bar device. Thirteen were successful: five of them were done on wet R30A7, four were conducted on dry R30A7 and four conducted on High Performance Concrete HPC.

The description of each test is detailed in the Table 3.8. It includes the name of the test, the type of ring used to apply the confinement, the type of concrete tested, the impact velocity measured from the speed barriers, the strain rate in the shear zone, the level of confinement pressure at the peak of the shear stress as well as the shear stress calculated from the average of the input and output forces. The experimental setup used for dynamic tests is presented in Figure 3.42.

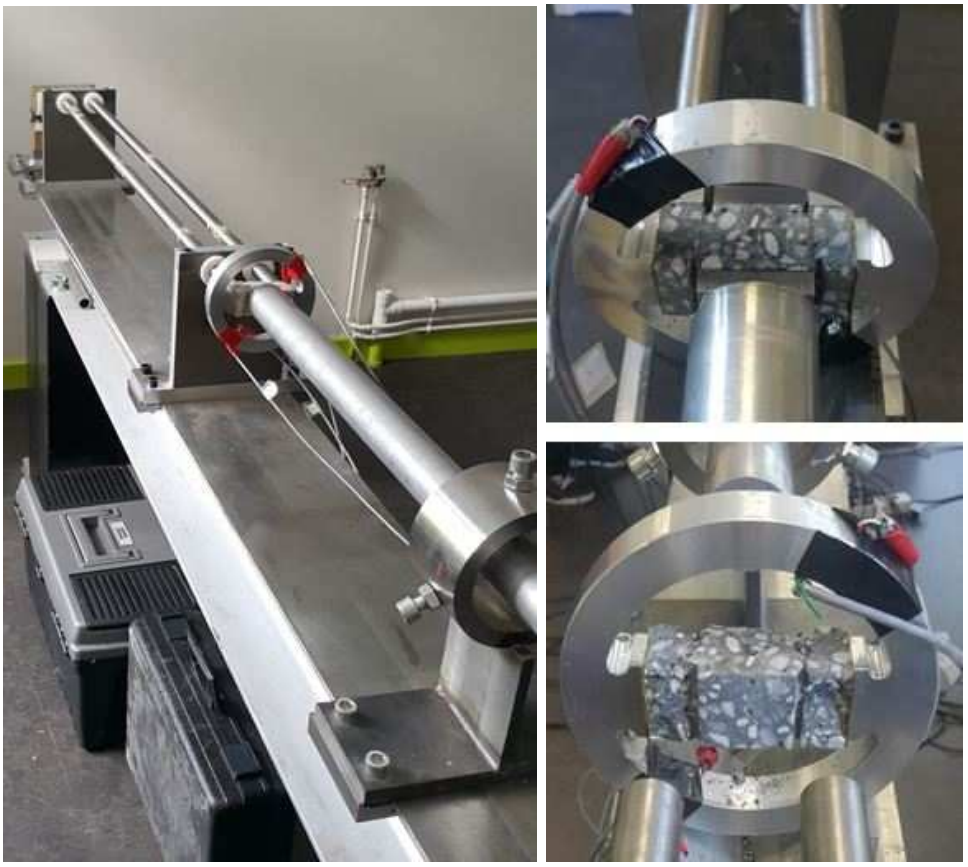

(a) (b)

FIGURE 3.42: Experimental device used for dynamic shear tests (a) General view of the setup (b) zoom on a concrete sample with the confinement ring before and after testing

3.4.4.1 Typical dynamic test results

Two gauges are glued on the input bar, one on the quarter length and the other on the mid length and on the other hand one gauge is glued in the middle of each output bar. The strain signals measured in the Hopkinson bars for a typical test and the shifted

forces deduced at both ends of the sample are shown in Figure 3.43. It was observed that the signals measured on each of the output bars are similar. The output forces which depend mainly on the parallelism of the sample were approximately similar for all the tests performed. The total output force was then obtained by adding the two forces extracted from these two signals (left and right bar).

The incident force was extracted from the strain signal of the gauge glued at one quarter of the input bar (at this distance there is no interference between the incident and reflected wave inside the bar) while the reflected one was taken from the one glued at mid length of the bar. The input force is then deduced by subtracting these two signals. As shown in Figure 3.43, the dynamic forces on both ends of the specimen are almost identical during the dynamic loading period (F_{input}=F_{output}) to the exception of the first 60 μs of applied loading. Moreover, signals registered by the gauges glued on the confinement cell were very similar (cf. Figure 3.44).

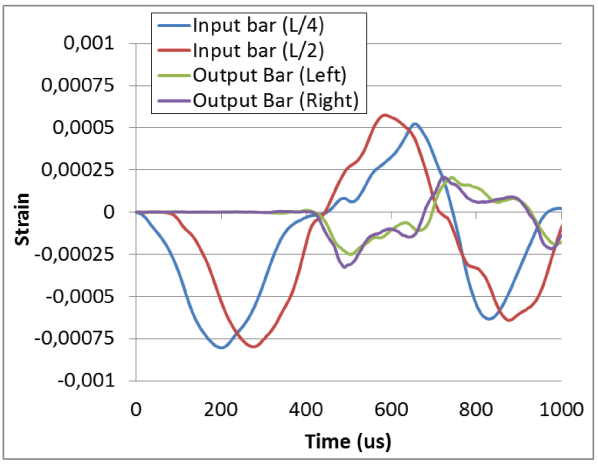

FIGURE 3.43: Typical signals recorded by strain gauges glued on the bars

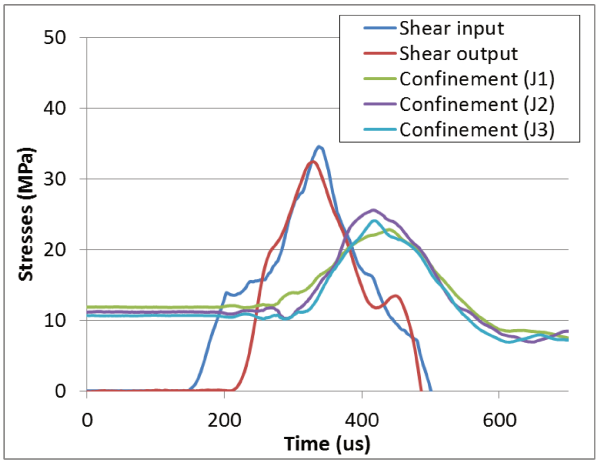

FIGURE 3.44: Typical stresses obtained in the ligament of the concrete the sample

The strain rate of dynamic tests is calculated from the elastic shear deformation which is the slope of the output stress divided by the concrete shear modulus. For example, it is equal to 30.7 /s for ShearDyn03 as represented in Figure 3.45. For each of the dynamic punching-through shear test, the loading rate was determined using this method.

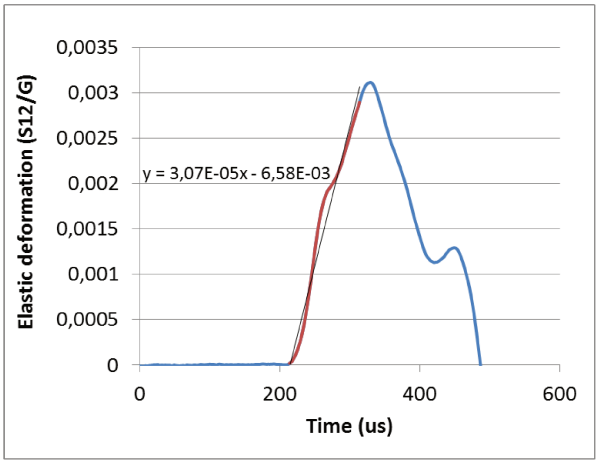

FIGURE 3.45: Typical elastic shear deformation curve for determining the strain-rate of dynamic tests

3.4.4.2 Repeatability of tests

As done in static tests, some tests were repeated twice in order to study the repeatability of the method used. By comparing the two tests Sheardyn13 and Sheardyn15, which are made on the same concrete (HPC) and with approximately same level of confinement, we can notice that the same level of shear stress was obtained (70 MPa) at a strain rate of around 80/s. The confinement starts to increase at the peak level of shear stress, from around 36 MPa to 60 MPa. (Figure 3.46)

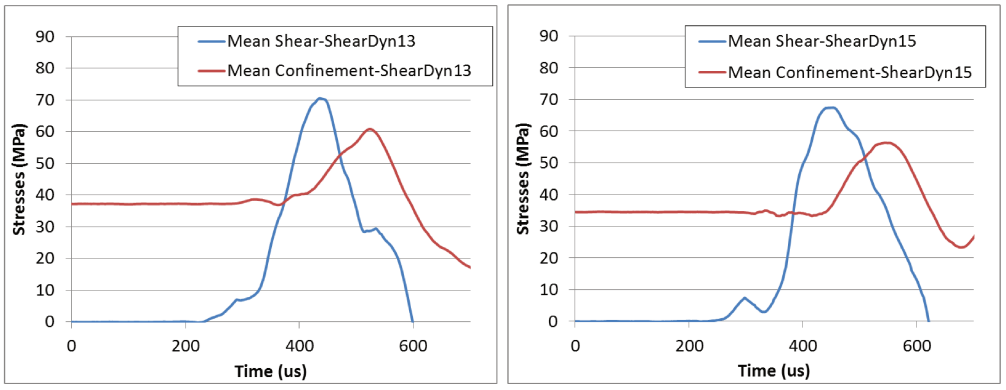

(a) (b)

FIGURE 3.46: Results of dynamic shear tests performed on high performance concrete specimens with steel confining cells (a) ShearDyn13 (b)Sheardyn15

3.4.4.3 Influence of confinement

To study the influence of confinement, tests were done with both confining rings, aluminum and steel. A comparison of shear tests performed with dry samples is presented in Figure 3.47.

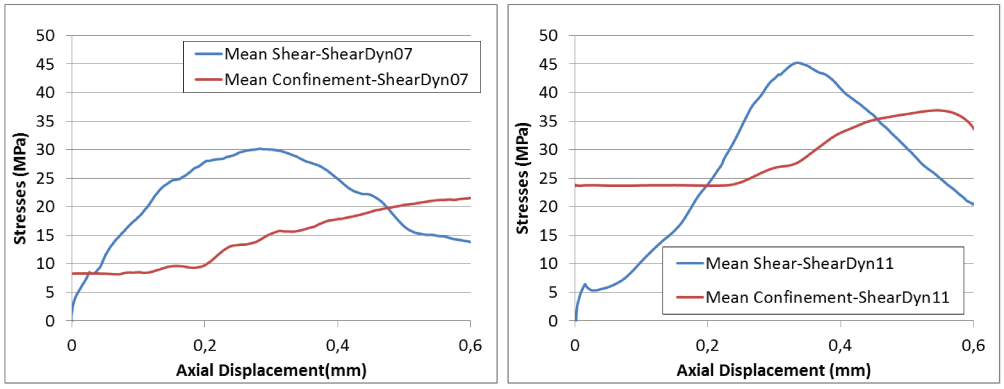

(a) (b)

FIGURE 3.47: Results of dynamic shear tests performed on dry specimens with (a) aluminum and (b) steel confining cells

As observed in static tests, when the confinement level increases, there is an increase of the shear strength of concrete. For 15 MPa of confinement at the peak of shear stress, concrete exhibited 30 MPa of shear strength while for a 27 MPa of confinement, shear strength reached higher value (45 MPa).

3.4.4.4 Influence of moisture content

A series of experiments has been conducted considering different moisture content.

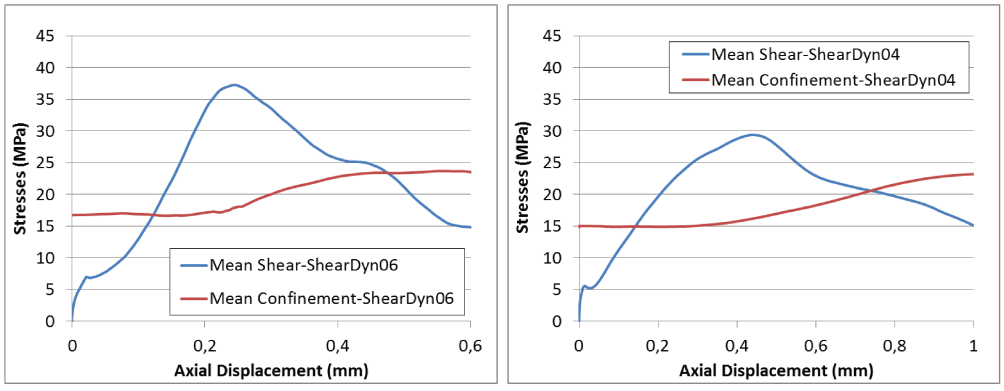

(a) (b)

FIGURE 3.48: Results of dynamic shear tests performed with an aluminum ring on (a) dry and (b) wet specimens

Experimental results obtained with dry and wet specimens in quasi-static loading with an aluminum alloy confining ring are reported on Figure 3.48. There is a slight difference in shear strength level for wet and dry specimens. The shear strength of wet samples (28 MPa) is lower than the one of dry ones (37 MPa).

3.4.4.5 Influence of concrete composition

The influence of concrete composition was studied by performing the same test at the same level of confinement on two different types of concrete. Experimental results obtained with ordinary concrete R30A7 and HPC specimens in quasi-static loading with an aluminum alloy confining ring are reported on Figure 3.49.

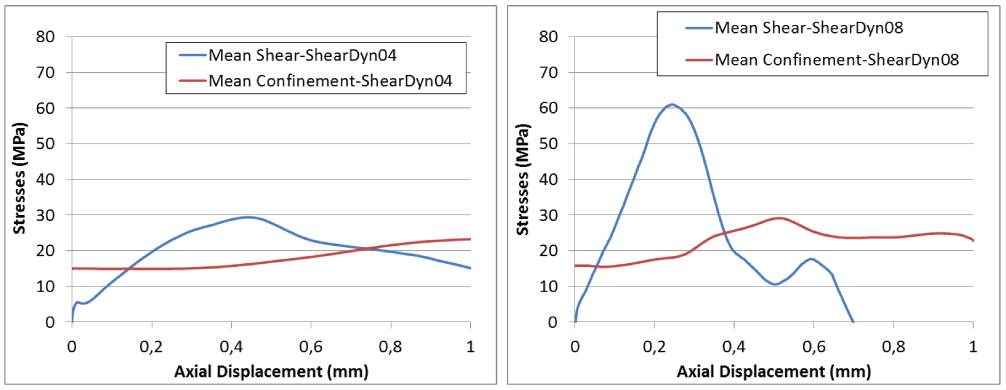

(a) (b)

FIGURE 3.49: Results of dynamic shear tests performed with an aluminum ring on (a) OC and (b) HPC

The experimental data indicate a maximum shear stress of 28 MPa in the ordinary concrete specimen while on the other hand the high performance concrete sample showed a markedly higher shear stress of about 60 MPa. A relatively similar confinement stress at the peak shear stress of about 18 MPa and 20 MPa respectively is observed in both tests.

3.4.4.6 Post-mortem observation

Similar cracking patterns were observed in both quasi-static and dynamic experiments. The main fracture plane is clearly noticeable in the pictures of Figure 3.50, it propagates almost perfectly straight connecting the two notches. But small micro-cracks inside the sample are not clearly visible and need to be investigated with X-ray micro tomography scan.

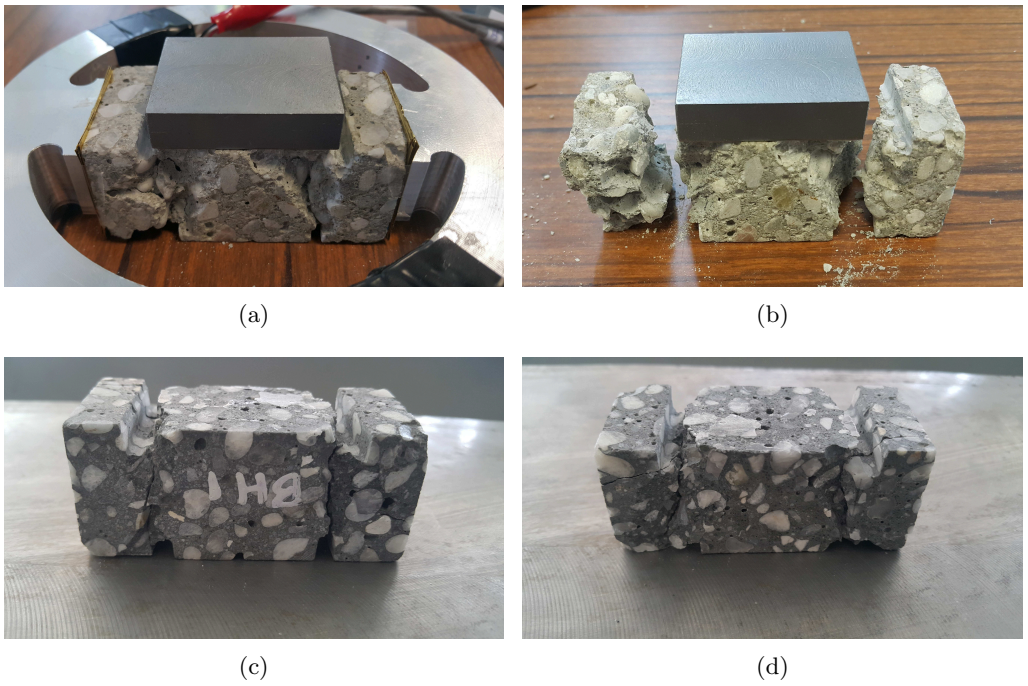

(a) (b)

(c) (d)

FIGURE 3.50: Crack pattern for different dynamic tests (a-b) Sheardyn06 (c-d) Sheardyn08

A high performance concrete, which was tested under dynamic loading (Sheardyn08), was scanned after the test. The multi-scale X-ray tomograph manufactured by RX solutions company was used at 150 kV and 140 μA. The exposure time is 0.5 s. An average of 6 images is used to obtain 1440 radiographies leading to a scanning time equal to one hour. The CT images have a resolution of 29 μm, it is obtained by zooming as much as possible to ensure that half the specimen is scanned. This resolution is sufficient to analyze the fracture pattern and modes. Figure 3.51 represents four cross-sections spaced of 10 mm. The vertical shear surface (mode II) inside the ligament is clearly visible at different locations inside the concrete sample which means that the fracture occurs throughout the volume. In addition, a wing crack that starts to propagate from the bottom notch of the sample toward the middle edge of the specimen can be observed. This crack is a tensile crack which was observed in the studies carried by Backers et al. [2004] and Yao et al. [2017] on rocks and by Lukić and Forquin [2015] on ultra-high performance concrete. These sub-critical cracks are expected to initiate before the peak (Watkins [1983]), they moves out of the induced shear zone and stops and their influence on the mode II fracture is negligible (Backers and Stephansson [2012]).

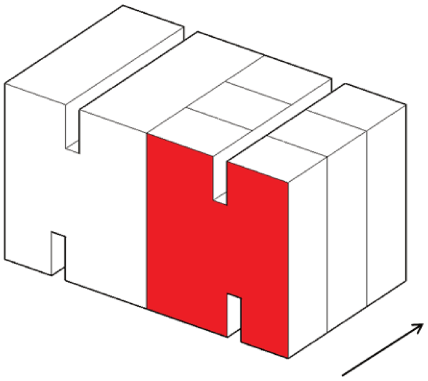

(a)

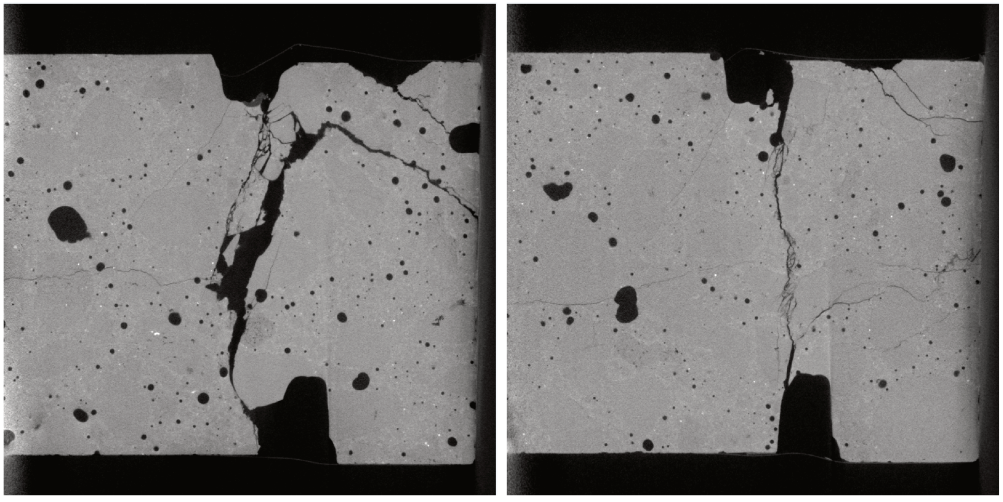

(b) (c)

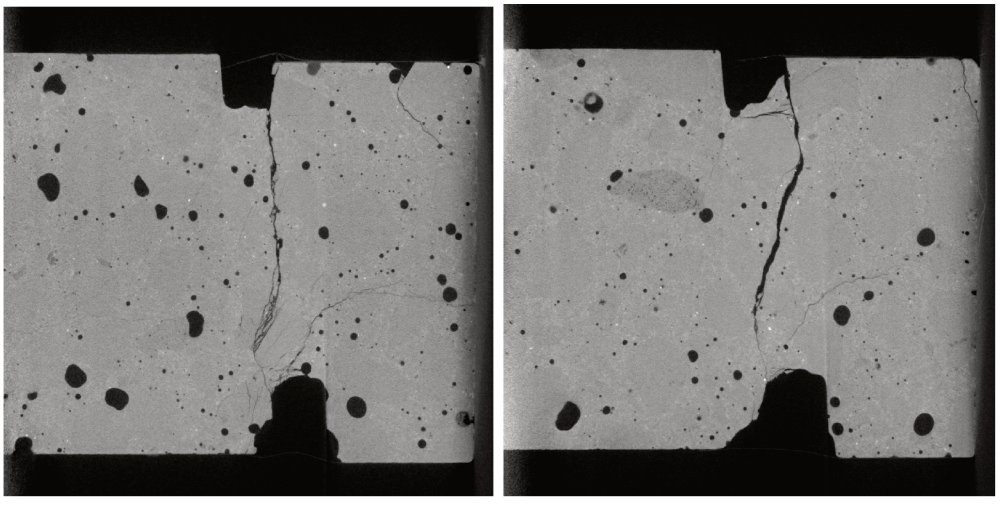

(d) (e)

FIGURE 3.51: CT scans done on BHP specimen tested under dynamic loading (Sheardyn08)

3.5 Discussion

A first comparison between previous results shows that for static tests, the peak of confinement stresses occurs roughly at the peak of shear stresses and both stresses start to decrease simultaneously (as in Figure 3.33 for example). Contrarily, for dynamic tests, the radial stress starts to increase after the peak of shear stress (as in Figure 3.46).

As mentionned before, a series of tests have been performed on different types of concrete with different levels of confinement in static and dynamic conditions, a summary of all these tests will be presented hereafter from Figure 3.52 to Figure 3.55.

Figure 3.52, Figure 3.53 and Figure 3.54 illustrate the shear strength of concrete as function of the confinement stress (at the peak of shear stress) for both sets of tests, static and dynamic for wet R30A7, dry R30A7 and HPC respectively.

For each of this test, the confinement level and shear stress in the ligament as well as the strain rate are given in Table 3.7 or Table 3.8.

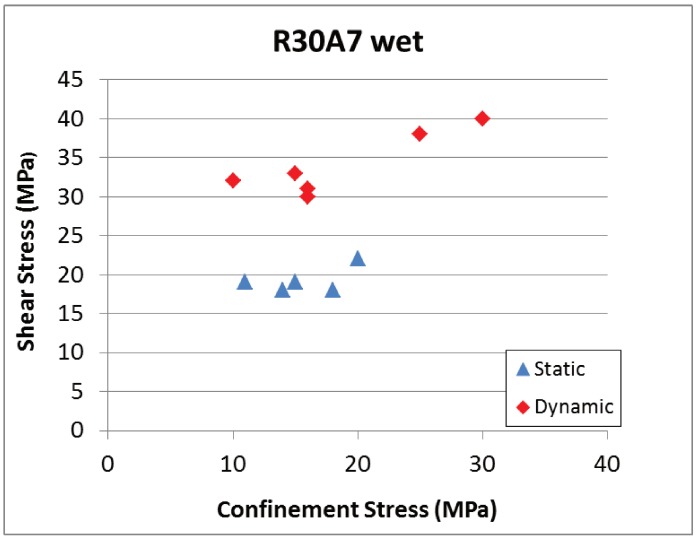

FIGURE 3.52: Quasi-static and dynamic shear tests done on wet R30A7

On the one hand, at the same loading rate, it is clear that the shear strength increases with the confining level. This trend was easy to be noticed for dynamic tests in wet R30A7. For a confinement stress of 10 MPa, the shear stress obtained was around 32 MPa whereas it reached a level of 40 MPa for a confinement of 30 MPa. Same trend was noticed for dry R30A7 and HPC. For dry R30A7 concrete, in static conditions, the maximim shear stress reached was 25 MPa for a confinement level of 12 MPa whereas a confinement of 25 MPa leads to 33 MPa of shear stress. In dynamic conditions, dry concrete shows an increase of shear strength from 30 MPa to 45 MPa at 15 MPa and 27 MPa of confinement stress respectively.

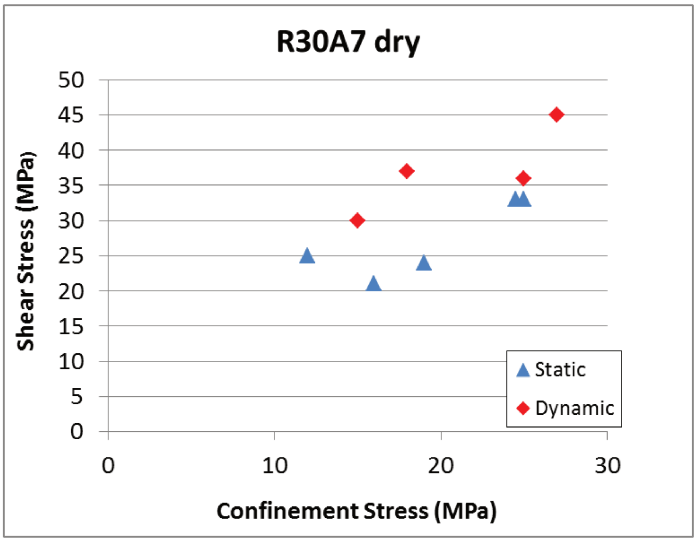

FIGURE 3.53: Quasi-static and dynamic shear tests done on dry R30A7

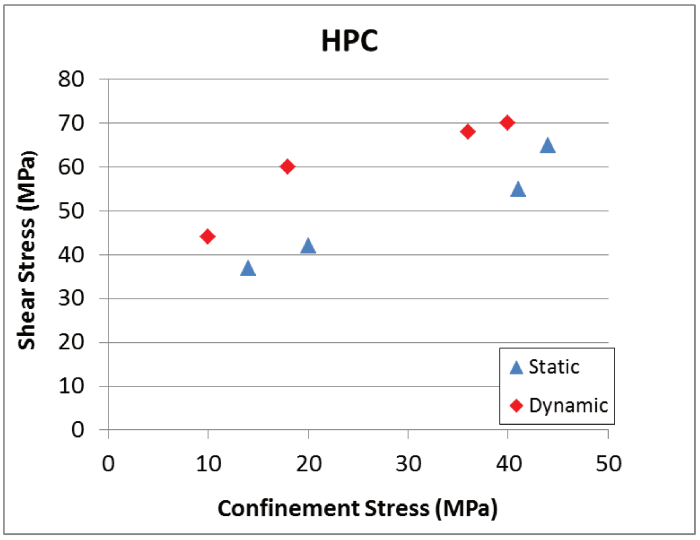

FIGURE 3.54: Quasi-static and dynamic shear tests done on HPC

Under quasi-static conditions, a shear strength of 40 MPa was obtained for a specimen of HPC subjected to 12 MPa of confinement and a strength of 63 MPa for a confinement level of 45 MPa. Moreover, as in quasi static conditions, high performance concrete showed higher shear strength for higher confinement under dynamic conditions. For example, the shear strength increases from 43 to 70 MPa for a mean confinement of 10 and 40 MPa respectively.

Hence, shear tests results presented with corresponding confinement stresses showed a tendency of increasing shear strength with confining level for the three sets of concrete.

On the other hand, for the same level of confining pressure, the shear stress is higher in dynamic tests than in static ones. This result is clear for wet R30A7 concrete where

the shear strength is around 20 MPa in static tests and around 35 MPa in dynamic ones (Figure 3.52).

For dry R30A7, for a confinement level of 16 MPa for example, the shear strength which exhibited the concrete specimen in quasi-static conditions is around 21 MPa while it reached 30 MPa in dynamic conditions (Figure 3.53).

For high performance concrete, for a 20 MPa of confinement, the static shear strength is 40 MPa while the dynamic strength is around 60 MPa (Figure 3.54) and this increase was observed for different level of confinement.

Therefore, it was concluded that for the three sets of concrete, there is a strain-rate sensitivity in the studied range of strain-rate for the same confining level.

In order to see more easily the influence of confinement and strain rate on concrete, the shear stress was plot as a function of strain rate for the three types of concrete. The size of the points plotted for each test depends on the level of confinement at the peak of the shear stress.

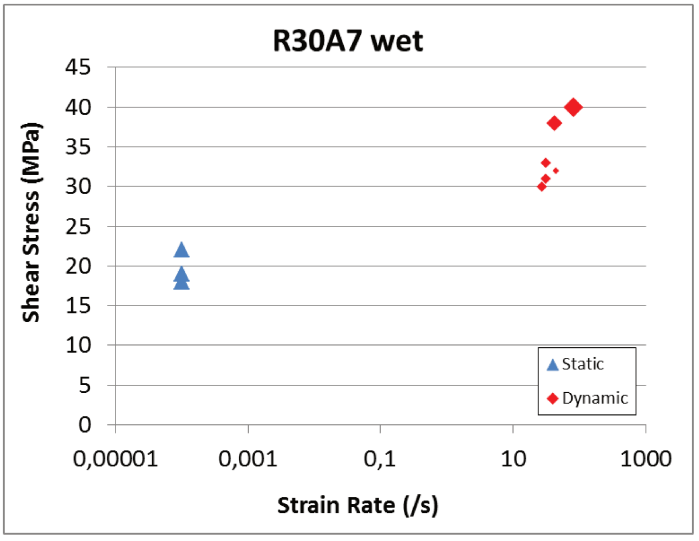

FIGURE 3.55: Quasi-static and dynamic shear tests done on wet R30A7

Even though there is a small scatter in the test results, these figures indicate that the shear strength in concrete depends on the confining pressure and the loading rate applied.

An empirical formula based on the above experimental data has been established for each type of concrete studied. This relation is formulated by fitting curve test data and

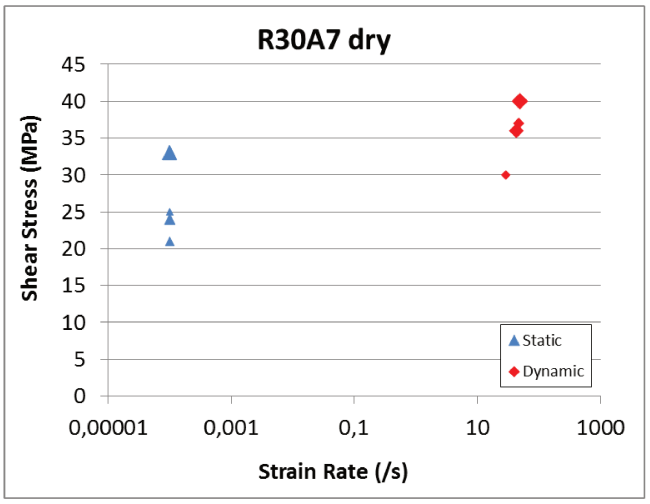

FIGURE 3.56: Quasi-static and dynamic shear tests done on dry R30A7

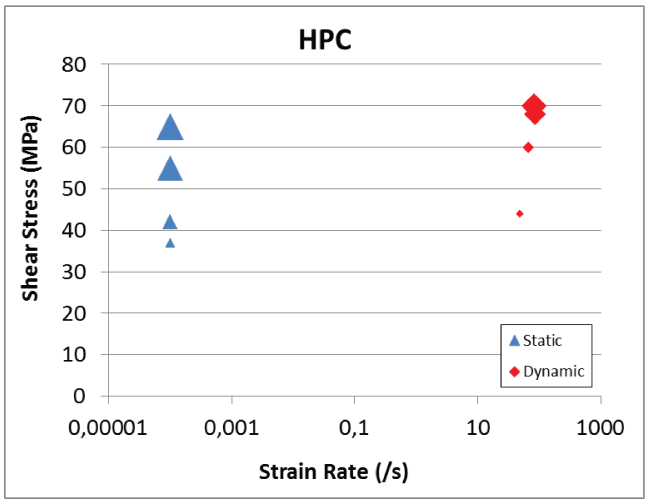

FIGURE 3.57: Quasi-static and dynamic shear tests done on HPC

predicts the shear strength of concrete as function of the confinement level σ_{n} in the ligament and the strain rate of the test.

$$\sigma_{shear} = 29.36 + 0.686\frac{\sigma_{\mathrm{n}}}{\sigma_{\mathrm{ref}}} + 0.189\frac{\dot{\varepsilon}}{\dot{\varepsilon}_{\mathrm{ref}}} \qquad R^2 = 0.92 \qquad \text{for Wet HPC} \qquad (3.31a)$$

$$\sigma_{shear} = 13.78 + 0.359\frac{\sigma_{\mathrm{n}}}{\sigma_{\mathrm{ref}}} + 0.371\frac{\dot{\varepsilon}}{\dot{\varepsilon}_{\mathrm{ref}}} \qquad R^2 = 0.967 \qquad \text{for Wet R30A7} \qquad (3.31b)$$

$$\sigma_{shear} = 12.79 + 0.743\frac{\sigma_{\mathrm{n}}}{\sigma_{\mathrm{ref}}} + 0.203\frac{\dot{\varepsilon}}{\dot{\varepsilon}_{\mathrm{ref}}} \qquad R^2 = 0.86 \qquad \text{for Dry R30A7} \qquad (3.31c)$$

where $\sigma_{\mathrm{n}} = 1$ MPa and $\dot{\varepsilon} = 1/s$

A possible prospect of this work would be to explore the strain-rate sensitivity of concrete shear strength at intermediate strain-rate

Chapter 4

Conclusion

In this chapter, results presented in previous chapters will be compared and discussed in a general frame. Then final conclusions of this work will be drawn and research perspectives will be discussed

4.1 General discussion

Results obtained on wet and dry R30A7 concrete samples confined with the Giga press or with the pre-stressed ring are compared with previous punching-through shear tests done with a passive confinement (Forquin [2011a,b], Forquin and Sallier [2013]). Shear stresses as function of confinement stresses in the ligament are plotted in Figure 4.1.

An increase of shear strength with an increase of confining pressure is considerably reported. This increase of strength was also markedly observed in others experiments on concrete samples like in triaxial tests and quasi-oedometric compression tests. This observation confirms the influence of confinement in increasing the strength of concrete. It should be noted that it is difficult to measure the confinement in the ligament of PTS samples performed with the Giga press due to a possible self-confinement of the sample. Thus confining stresses were calculated from numerical simulations conducted with the Drucker-Prager model.

Moreover, results obtained in this study and those obtained in the literature over a wide range of strain-rates are gathered in Figure 4.2. One the one hand, it is shown that the shear strength of dry concrete samples is higher than that of wet ones for each of the tests done whatever the loading rate. One the other hand, there is a trend of increasing strength with strain-rates for the different sets of concrete in the studied range

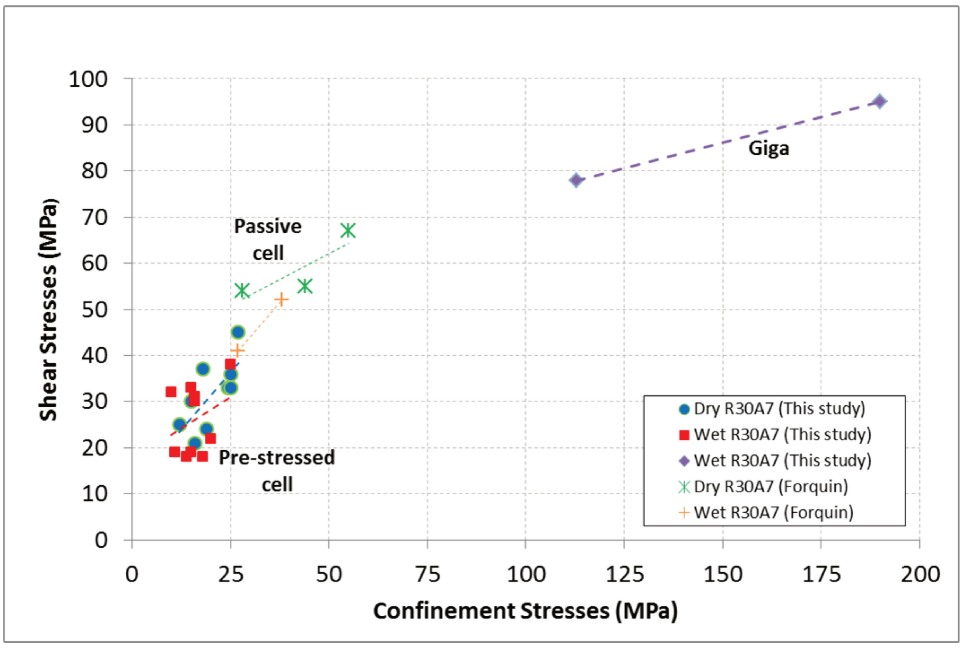

FIGURE 4.1: Results of shear strength with respect to confinement level in the ligament compared to the literature data

of strain-rate. It should be noted that the level of shear strength is not only influenced by the strain-rate but also by the confinement. This is why higher shear strength were obtained with the Giga press (results in purple) and with the passive confinement (results in orange and green) than for tests done at almost same strain-rate with the pre-stressed loading cell.

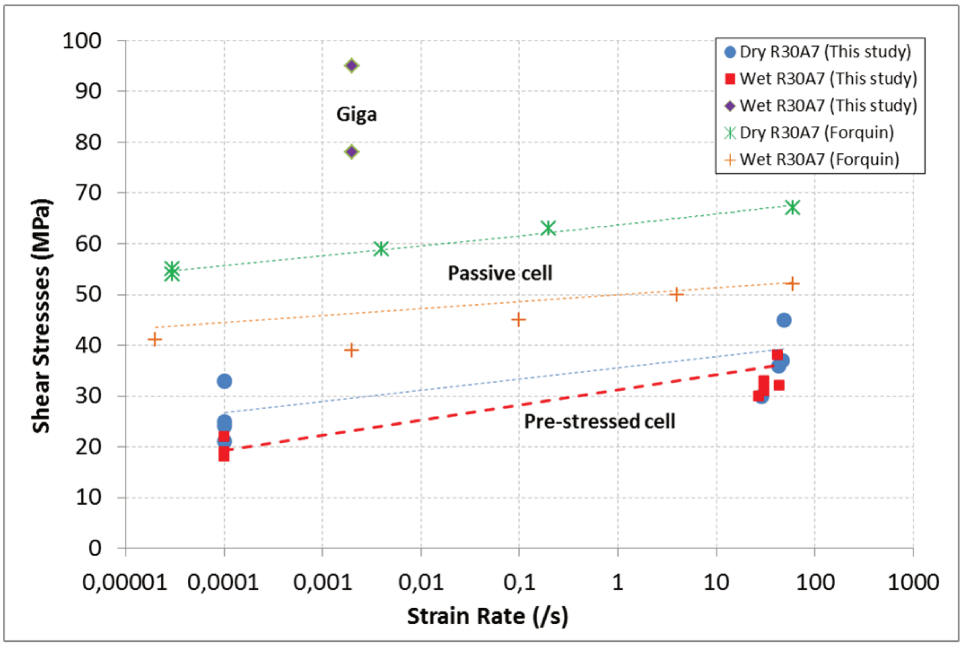

FIGURE 4.2: Shear strength with respect to strain rate for different concrete samples in different studies

In order to compare the order of magnitude of the increase of strain-rate in the tests performed with the pre-stressed ring regarding others experiments, the ratio of dynamic strength on static strength is calculated (Table 4.1 and Table 4.2) and plotted in Figure 4.3 and Figure 4.4 for wet and dry R30A7 samples respectively.

	Wet R30A7			
	Traction/Spalling	QOC/TXT (At 400 MPa)	PTS passive (At ~40 MPa)	This study (At 15 MPa)
Authors, Year	Erzar, 2010	Forquin et al, 2015/ Vu et al, 2009	Forquin and Sallier, 2013	-
Static strength (MPa)	2.6	~200*	40	20
Dynamic strength (MPa)	12	~200**	55	33
Dynamic/Static Strength	4.6	~1	1.38	1.65

TABLE 4.1: Results obtained on wet R30A7 concrete samples compared to data in the literature (*Quasi static triaxial test done by Vu et al. [2009b], **Dynamic Quasi-oedometric test done by Forquin et al. [2015a]

Values of the static and dynamic strength for R30A7 concrete sample subjected to quasi-static tensile tests or dynamic spalling test were taken from Erzar [2010]. It was observed that at high strain rates, a strong increase of tensile strength is observed for both kinds of concrete (wet and dry) and that the tensile strength of wet concrete is higher than the dry one. This difference might be explained by the so-called Stefan effect activated in tension; due to its viscosity, free water contained in wet specimens slightly improves its dynamic strength (Erzar and Forquin [2011]).

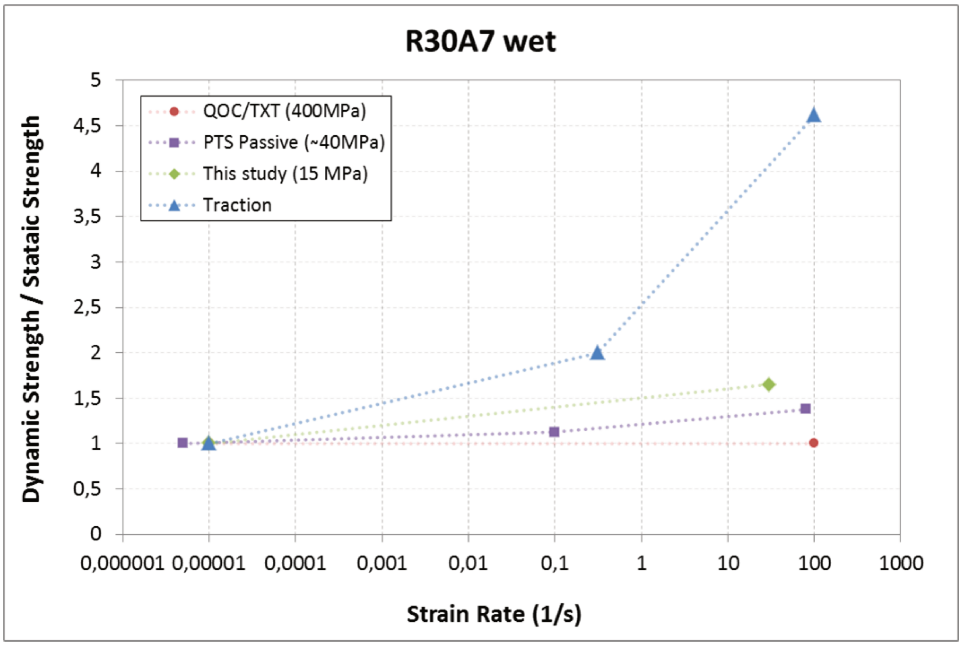

FIGURE 4.3: Relative increase of strength with respect to strain rate for wet R30A7 concrete subjected to different types of loading

Values of deviatoric strength for static and dynamic quasi-oedometric compression (QOC) tests were taken from Forquin et al. [2015a]. The dynamic QOC tests performed on

R30A7 concrete can be considered as non-drained because they are performed at high velocity and water can not escape pores. As quasi-oedometric quasi-static tests are performed on R30A7 concrete were made in not-well controlled draining conditions (Forquin et al. [2015a]), the static value for wet R30A7 samples was taken from a non-drained triaxial test made by Vu et al. [2009b] where membranes were used around the sample in order to prevent water to evacuate from the sample during the test.

PTS passive test was done by Forquin [2011a] and Forquin and Sallier [2013] with a passive confinement cell. During static tests a radial stress about 30 MPa was observed in both dry and wet tests, where as a radial stress about 40-50 MPa is observed during dynamic tests. These two tests were chosen because there is not data at the same level of confinement.

	Dry R30A7			
	Traction/Spalling	QOC (At 400 MPa)	PTS passive (At ~40 MPa)	This study (At 15 MPa)
Authors, Year	Erzar, 2010	Forquin et al, 2015	Forquin and Sallier, 2013	-
Static strength (MPa)	2.4	300	53	20
Dynamic strength (MPa)	10	370	75	30
Dynamic / Static Strength	4.17	1.23	1.42	1.5

TABLE 4.2: Results obtained on dry R30A7 concrete samples compared to data in the literature

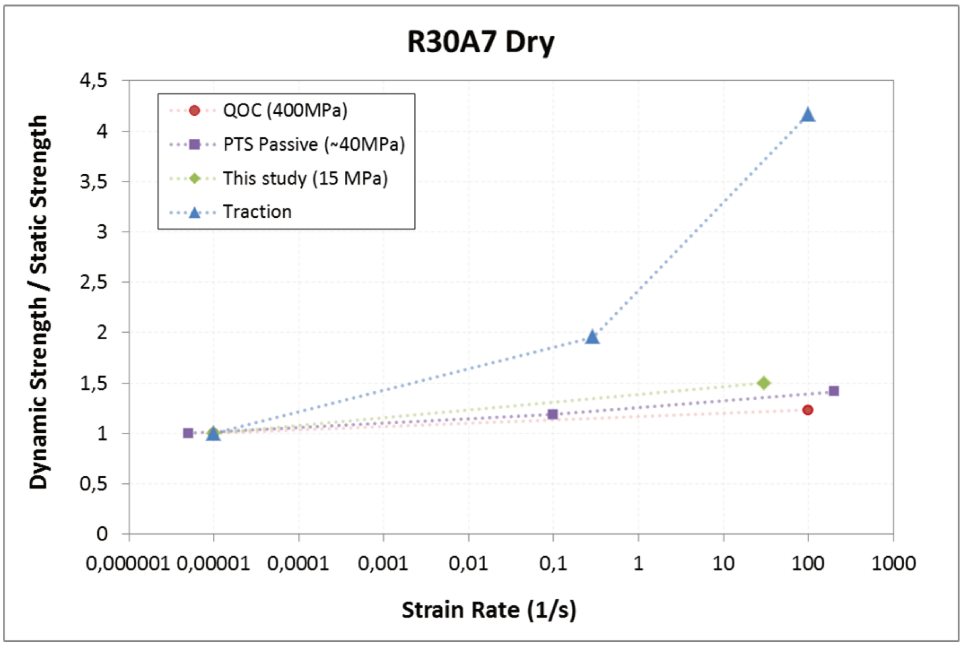

FIGURE 4.4: Relative increase of strength with respect to strain rate for dry R30A7 concrete subjected to different types of loading

The obtained results showed a strong influence of strain rate under tensile loading whereas a smaller sensitivity is noted during punch-through shear tests and a limited sensitivity is noted during quasi-oedometric compression tests for both sets of concretes

(dry and wet). This observation can be explained by the influence of confinement: the lower the confinement, the higher the sensitivity of concrete strength to strain-rate. Consequently, it is concluded on the one hand, that the confinement has a major effect on the shear behavior of concrete. On the other hand, the strain-rate sensitivity is small compared to traction or unconfined compression tests.

4.2 Conclusion and perspectives

The security of concrete structures used in many applications such as nuclear containments, bunkers or dams is of considerable concern since these structures can be exposed to various extreme loadings during which different compressive, tensile and shear modes might be observed. Various experimental methods have been used to explore the behavior of concrete under different types of loading over a wide range of strain rates. It was shown in the literature that concrete exhibits an increase of strength under confinement (triaxial and quasi-oedometric compression tests) and dynamic loadings (spalling tests). However, in contrast to tensile behavior, the shear behavior of concrete under compression and dynamic loadings has not been carefully studied at a constant confining level.

The aim of the present work is to investigate the quasi-static and dynamic shear behavior of concrete under confined conditions. In previous experiments, concrete samples were either subjected to a small level of confinement (Montenegro et al. [2007]) or higher level of confinement with a passive metallic ring (Forquin [2011b]). In the last method, a change of confinement level occurs during the tests and constitutes a major drawback of this technique. Two methods have been developed to apply confinement to samples before testing them under shear. The first one is based on applying a hydrostatic pressure using a high capacity press and the second one consists of pre-confining the concrete sample using a pre-stressed metallic cell.

In the first chapter of this manuscript, a bibliographic review summarizing the different techniques existing in the literature and which describes the behavior of concrete when subjected to compression or shear at different strain rates is presented. Dynamic simple compression tests showed an increase of strength with strain rate, this increase being mainly structural as it is due to an artificial lateral pressure induced by inertial effects that prevent the sample expansion. Moreover, regarding the material behavior under compression, it was shown that brittle materials are very sensitive to lateral pressure. An increase of strength with confinement and a transition from quasi-brittle to ductile behavior is revealed. The behavior of concrete under compression is also dependent on the saturation ratio. At high levels of confinement, the presence of water has a

major importance: the shear strength of saturated concrete is limited to a maximum value whatever the confining pressure. Sample confined with a passive cell and subjected to dynamic loadings showed a small sensibility to strain-rates. This observation is in contrast to what it is observed in dynamic uniaxial compression tests. This can be explained by the fact that the radial confinement seems to cancel the effect of the radial inertia of the material. Furthermore, static and dynamic experiments conducted considering different water saturation ratios showed a strong influence on the confined behavior of concrete. By reducing the level of effective stress applied to the concrete skeleton, the pore pressure strongly influences the dynamic behavior of confined concrete. Besides, quasi static and dynamic punch-through shear tests done on dry and wet concrete showed a small strain rate sensitivity. It was concluded that the Stephan effect which is supposed to explain the strain rate sensitivity of wet concrete in tension is inoperative under shear loading.

Chapter two describes the new experimental technique developed to study the behavior of concrete subjected to high level of confinement. This method consists of applying a high level of hydrostatic pressure to a concrete sample prior to the application of the shear loading. The specimens consists of cylindrical samples with coaxial cylindrical notches on the top and bottom faces leaving a cylindrical ligament. Two steel rings were glued around the cylindrical notches in order to prevent this zone to be damaged under compression. The high capacity triaxial press Giga has been used to apply a confinement up to 100 MPa. It was shown that the confinement has a major influence on the shear behavior of concrete. An increase of shear strength was noticed for higher confinement level.

In chapter three, the method based on the pre-stressing of the concrete sample is investigated. It consists in inserting a concrete specimen into a pre-stressed metallic ring. When the loading is released, confining stresses are transferred to the ligament of the concrete sample. Then, a vertical displacement is applied to the central part of the sample to produce shear deformation in the ligament. Two types of metallic ring were used (aluminum and steel) in order to study the influence of confinement: higher shear strength was reported with higher confinement which confirms pressure sensitivity of concrete. Dynamic tests performed with the Split Hopkinson Bar technique were performed to analyze the effect of strain-rate on the confined shear behavior of concrete. It was found that at the same level of confinement, concrete samples subjected to dynamic loadings exhibited higher shear strength than the one subjected to static loadings. Moreover, both dried and saturated samples have been tested: dry samples exhibited higher shear strength. In addition, tests on high performance concrete were conducted: the shear strength of high strength concrete strongly exceeds the one of the ordinary concrete.

In this chapter, the results obtained in both methods are discussed and compared with data existing in the literature. By plotting the ratio of dynamic strength to static strength, it was found that, whereas the strain rate has a strong influence on the tensile strength of concrete, this influence decreases with the level of confinement and appeared quite limited under highly confined compression tests.

Finally, the perspectives for this study are first to complete experimental tests done with the Giga press. Tests with different confinement levels and different saturation ratios could be performed to verify the influence of free water on the shear behavior of concrete under very high confinement level.

Furthermore, tests on concretes mixed with different aggregates composition could be considered to study their effect on the concrete shear behavior. It is also interesting to conduct experimental tests with the pre-stressed cell at intermediate strain-rate to investigate the strain-rate sensitivity of concrete shear strength over different ranges of strain-rate. Moreover, micro-tomography could be used during quasi-static testing in order to examine 3D damage evolution and failure mechanism.

On the other hand, since it is difficult to understand all the mechanical phenomena happening inside concrete with the macroscopic modeling, it is necessary to simulate the real microstucture of concrete and analyze the effects of each constituent on the macroscopic response. This is why performing mesoscopic numerical simulations in which the behavior of cement paste and aggregates is differentiated is very important. It would be necessary to use a model capable of simulating numerically the crack propagation in mode II in aggregates and in cement paste. The model must be identified and validated by experiments. In addition, the model should be capable of taking into account the microstructural parameters of the material (free water content, characteristic size of the mesostructure, resistance of the aggregates). The calculations will highlight the influence of the mesostructure on the confined shear behavior of concrete. A preliminary model and results are presented in Appendix C.

Résumé en francais

Introduction

Le béton est le matériau le plus utilisé en génie civil. Au cours de leur durée de vie, les structures en béton armé peuvent être soumises à différentes types de sollicitations qui peuvent être provoquées intentionnellement ou accidentellement comme les impacts ou les séismes. Par exemple, lors de la pénétration d'un projectile dans une dalle en béton, différents modes de rupture peuvent être générés: en particulier pendant la phase de pénétration de l'impacteur, des contraintes de cisaillement et de compression tri-axiale peuvent être observées à l'intérieur de la cible. De plus, due aux effets inertiels, le confinement atteint dans le béton peut être assez important en fonction de la vitesse d'impact et des caractéristiques de la cible et du projectile (Bailly et al. [1996]). D'autre part, dans le cas d'un séisme, si les poteaux en béton armé ne sont pas suffisamment renforcés transversalement, une rupture en cisaillement se produit. D'où la nécessité d'étudier le comportement du béton soumis à une sollicitation de cisaillement confiné.

D'après l'étude bibliographique, des essais de compression tri-axiale ont été réalisés depuis plusieurs décennies sur le béton (Schmidt et al. [2009], Warren et al. [2004]). L'échantillon de béton est soumis à une pression hydrostatique dans un premier temps puis une contrainte axiale est appliquée. Il a été observé qu'une augmentation du confinement augmente la contrainte déviatorique maximale atteinte et le comportement du béton tend vers un comportement plus ductile. Une étude (Gabet et al. [2008]) sur des éprouvettes en 'béton réel' a permis d'appliquer une pression allant jusqu'à 0,85 GPa et une déformation volumique maximale d'environ 12% a été atteinte dans l'échantillon. Cependant, les essais tri-axiaux sont difficiles à réaliser dans des conditions dynamiques, ces difficultés sont liés à l'application d'un confinement à l'aide d'un fluide sous haute pression et à l'application d'un confinement axial avant le chargement dynamique. Une autre méthode a été utilisée pour caractériser le comportement confiné du béton sur une large gamme de vitesse de déformation : l'essai de compression quasi-oedométrique. Cette méthode a été proposée par Bazant et al. [1986], Burlion [1997] et Gatuingt [1999] et entièrement revisitée par Forquin et al. [2007] dans des conditions statiques et par

Forquin [2003], Forquin et al. [2008c], Forquin et al. [2010] et Piotrowska and Forquin [2015] dans des conditions dynamiques (SHPB). Une pression maximale de 800 MPa a été atteinte avec une déformation volumique de 15%.

Puisque la rupture en cisaillement en mode II a également été observée dans les essais d'impact, il est important de comprendre le comportement du béton sous un tel chargement (Forquin et al. [2008c], Forquin et al. [2010] et Lukić and Forquin [2015]). L'essai 'Punch Through Shear' est l'une des techniques qui existent dans la littérature pour étudier le comportement en cisaillement du béton dans lequel des déformations élevées sont atteintes à l'intérieur d'un échantillon de béton. Ces essais ont été menés sur du béton à faible pression (environ 8 MPa) (Montenegro et al. [2007]) ou sur des roches à des pressions hydrostatiques allant jusqu'à 70 MPa (Backers [2004]). De plus, la technique de test de cisaillement 'Punch Through Shear' a été développée et réalisée dans des conditions statiques et dynamiques avec une cellule passive. Durant cet essai, les contraintes radiales varient et dépendent du comportement du matériau testé (Forquin [2011b]), ce qui constitue un inconvénient majeur de la méthode.

L'objectif du travail de cette thèse est de combler les lacunes des tests existants dans la littérature pour étudier le comportement du béton soumis à des pressions de confinement relativement élevées (de quelques dizaines à quelques centaines de MPa) à des niveaux de déformation élevés et sur une large gamme de vitesses de déformation. Pour cela, deux nouvelles méthodes expérimentales dérivées du 'Punch Through Shear test' ont été développées pour caractériser le comportement en cisaillement confiné du béton sous chargement statique et dynamique.

Le premier test est un test de cisaillement 'Punch Through Shear' tri-axial qui consiste à appliquer dans une première phase une pression hydrostatique à un niveau prédéterminé. Dans une deuxième phase, la pression de confinement étant maintenue constante, une force axiale est appliquée sur la partie centrale de l'échantillon pour produire un cisaillement dans le ligament. La deuxième méthode expérimentale consiste à confiner l'échantillon de béton avec une cellule métallique précontrainte avant d'appliquer la charge de cisaillement. Des simulations numériques réalisées pour la conception de chaque test sont décrites puis les procédures de test et les différents résultats sont présentés.

Test de cisaillement triaxial

Dans le chapitre deux, des essais quasi statiques effectués en appliquant une pression hydrostatique puis un cisaillement à l'échantillon de béton sont présentés. Ces tests sont réalisés avec la presse Giga dont les enclumes ont été modifiées afin de pouvoir

appliquer le chargement de cisaillement sur des échantillons de béton. Des simulations numériques ont été conduites pour dimensionner le test et choisir les dimensions optimales de l'échantillon testé. Le modèle 'Drucker-Prager" qui prend en compte la dilatance du béton et qui prévoit l'augmentation des contraintes de cisaillement avec le confinement a été utilisé pour modéliser l'éprouvette en béton. En choisissant les paramètres du modèle déjà calibré sur des essais de cisaillement avec confinement passif (Forquin [2011b]), les contraintes radiales ont été estimées à partir de la pression de confinement appliquée. Un diamètre de 70 mm, une hauteur de 40 mm ont été choisis pour l'échantillon avec un diamètre de 35 mm et une hauteur de 15 ou 20 mm pour les entailles. Afin d'obtenir une surface de rupture cylindrique et non tronconique, le diamètre intérieur de l'entaille circulaire inférieure coïncide avec le diamètre extérieur de l'entaille circulaire supérieure.

Les tests sont réalisés sur le R30A7, un béton ordinaire dont les plus gros granulats sont de 8 mm. Des bagues de confinement ont été collées sur les extrémités de la partie centrale de l'échantillon pour éviter son endommagement sous compression et par suite son effondrement durant l'essai. L'influence de la hauteur de l'entaille a été étudiée en testant les deux hauteurs d'entaille 15 et 20 mm et il a été observé que les contraintes de cisaillement diminuent avec la hauteur d'entaille. Cela peut s'expliquer par le fait que les contraintes radiales sont plus élevées pour une plus petite surface de cisaillement d'une part ou par le fait que le développement de micro-fissures sur le fond des entailles mène à la rupture de l'échantillon. En plus, deux niveaux de confinement ont été testés et une augmentation des contraintes de cisaillement avec la pression de confinement appliquée a été observée. Une pression de confinement de l'ordre de 100 MPa a pu être appliquée et une déformation de l'ordre de 30% a été estimée dans l'échantillon.

Test de cisaillement avec cellule de confinement

Dans le troisième chapitre, une nouvelle technique est présentée : une cellule métallique précontraint l'échantillon de béton appliquant ainsi une pression de confinement active. Cette cellule métallique est déformée élastiquement pour pouvoir y insérer un échantillon prismatique. Le retour élastique de l'anneau durant la phase de décharge applique alors une pression de confinement sur l'échantillon. La cellule est instrumentée avec des jauges de déformation qui permettent de calculer les niveaux de contraintes de confinement au cours de l'essai de cisaillement. Une fois le confinement appliqué, un déplacement est imposé sur la partie centrale de l'échantillon pour produire une déformation de cisaillement dans le béton. Une presse hydraulique (Schenck) est utilisée pour effectuer des essais de cisaillement statique et un dispositif de barres de Hopkinson a été utilisé pour réaliser des essais dynamiques avec une barre en entrée et deux barres en sortie. Une série de simulations numériques a été menée afin de dimensionner les essais et par

suite trouver les dimensions optimales des cellules de confinement, de l'échantillon de béton et des barres de Hopkinson.

Deux cellules de confinement métalliques ont été utilisées (en acier ou en aluminium) dans le but de mettre en évidence l'influence du niveau de pression de confinement : une contrainte maximale de cisaillement plus élevée a été rapportée avec un confinement plus élevé, ce qui confirme la sensibilité à la pression du béton sur toute la plage de déformation considérée ($1e^{-4}$/s - 100/s).

Des échantillons de béton R30A7 secs et humides ont été testés pour étudier l'influence de la teneur en eau. Les échantillons humides sont placés dans l'eau et les échantillons secs sont séchés au four à 60°C jusqu'à stabilisation de leur masse. Les échantillons secs présentent une résistance au cisaillement plus élevée que les échantillons humides sur la plage de vitesses de déformation considérée.

Un béton haute performance (HPC) a également été étudié et les résultats ont été comparés à ceux obtenus avec le béton ordinaire pour mettre en évidence l'influence de la composition du béton sur sa résistance au cisaillement. La résistance au cisaillement du béton haute performance dépasse fortement celle du béton ordinaire.

Finalement, la comparaison des essais statiques et dynamiques des trois types de béton a permis de conclure qu'il y a une augmentation de la résistance avec la vitesse sur la plage de vitesses de déformation explorée.

D'après les vidéos pris durant les essais statiques, on a pu remarquer une surface de rupture de cisaillement droite reliant les deux entailles de chaque côté de l'éprouvette. Cette rupture correspond à une rupture en mode II initiée aux alentours du pic de chargement. De même, une analyse par tomographie a été faite sur un échantillon testé sous chargement dynamique pour examiner le plan de rupture à l'intérieur de l'échantillon. Il a été observé que la surface de rupture en cisaillement est verticale à travers tout le volume de l'éprouvette.

Conclusions

Dans le dernier chapitre, les résultats obtenus avec la presse Giga et ceux obtenus avec la cellule de confinement sont comparés avec les résultats des essais conduits par Forquin [2011b] et Forquin and Sallier [2013] avec une cellule de confinement passif. Puis des conclusions finales sont tirées et des perspectives sont proposées.

Les essais ont permis d'aboutir aux conclusions suivantes. D'une part, une augmentation de la résistance au cisaillement avec une augmentation de la pression de confinement est rapportée pour tous les essais de cisaillement réalisés. Une telle augmentation de

résistance a également été observée dans d'autres expériences comme pour des essais triaxiaux (Vu et al. [2009b]). Les résultats obtenus dans le cas présent confirment l'influence du confinement sur l'augmentation de la résistance du béton. D'autre part, en traçant la résistance au cisaillement en fonction de la vitesse de déformation, une augmentation de cette résistance avec la vitesse de déformation apparaît pour les différents types de béton dans la gamme de vitesses de déformation étudiée. De plus, la résistance au cisaillement des échantillons de béton sec est supérieure à celle des échantillons humides quel que soit la vitesse de déformation.

Afin de comparer l'ordre de grandeur de l'augmentation de la résistance avec la vitesse de déformation, le rapport de la résistance dynamique sur la résistance statique est calculé puis comparé aux rapports obtenus pour des essais de traction (conduits par Erzar [2010]), des essais quasi-oedométriques (Forquin et al. [2015a] and Vu et al. [2009b]) et des essais de cisaillement avec confinement passif (Forquin [2011a] and Forquin and Sallier [2013]). Ces résultats montrent une influence significative de la vitesse de déformation quand le béton est soumis à de la traction alors qu'une sensibilité modérée est notée lors des essais de cisaillement et une sensibilité limitée est observée lors des essais de compression quasi-oedométrique et cela pour les deux bétons (secs et humides). Cette observation peut s'expliquer par l'influence du confinement : plus le confinement est faible, plus la sensibilité du béton à la vitesse de déformation est élevée.

Par conséquent, il est conclu d'une part, que le confinement a un effet majeur sur le comportement au cisaillement du béton et que la résistance du béton sec est plus élevée que le béton humide. D'autre part, la sensibilité à la vitesse de déformation est faible par rapport à celle observée sous chargement de traction.

Appendix A

Technical drawings of the new setup of the Giga press

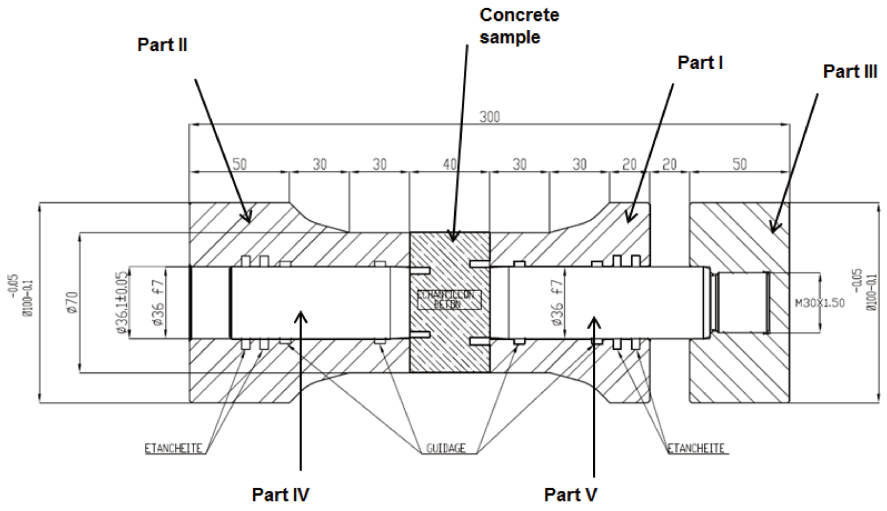

FIGURE A.1: PTS assembly

MATIERE :
- 42CrMo4 Prétraité -Rm=1100-1200MPa + Chrome 25µ sur tiges
- 30 CrNiMo 8 Prétraité - Rm= 1100-1200MPa

ENCLUME DE CISAILLEMENT POUR ESSAIS BETON DANS CAISSON HYPERBARE A 1500 BAR

B	Changement Matière			18/06/2015	YD
A	Creation du plan			09/06/2015	YD
Rev	Modification			Date	Approuvé par
Ref	Qté	Nom de l'ensemble : ENSEMBLE			No. d'affaire : 15001626
Dessiné par -		Vérifié par YD	Approuvé par - date	N° plan client : -	Date : 09/06/2015 / Echelle 1/2
D.P.O 67 Boulevard de la mer 17340 Chatelaillon Plage Tel : 05 16 07 07 08 Fax: 05 46 56 17 13 Mail : dpo@dpo-hydraulique.com Site : www.dpo-hydraulique.com				ESSAI-GIGA	
				N° de plan : 1626-000	Feuille No. 1/1

Ce plan est la propriété exclusive de la société DPO. Il ne peut en aucun cas être utilisé ou reproduit sans son autorisation.

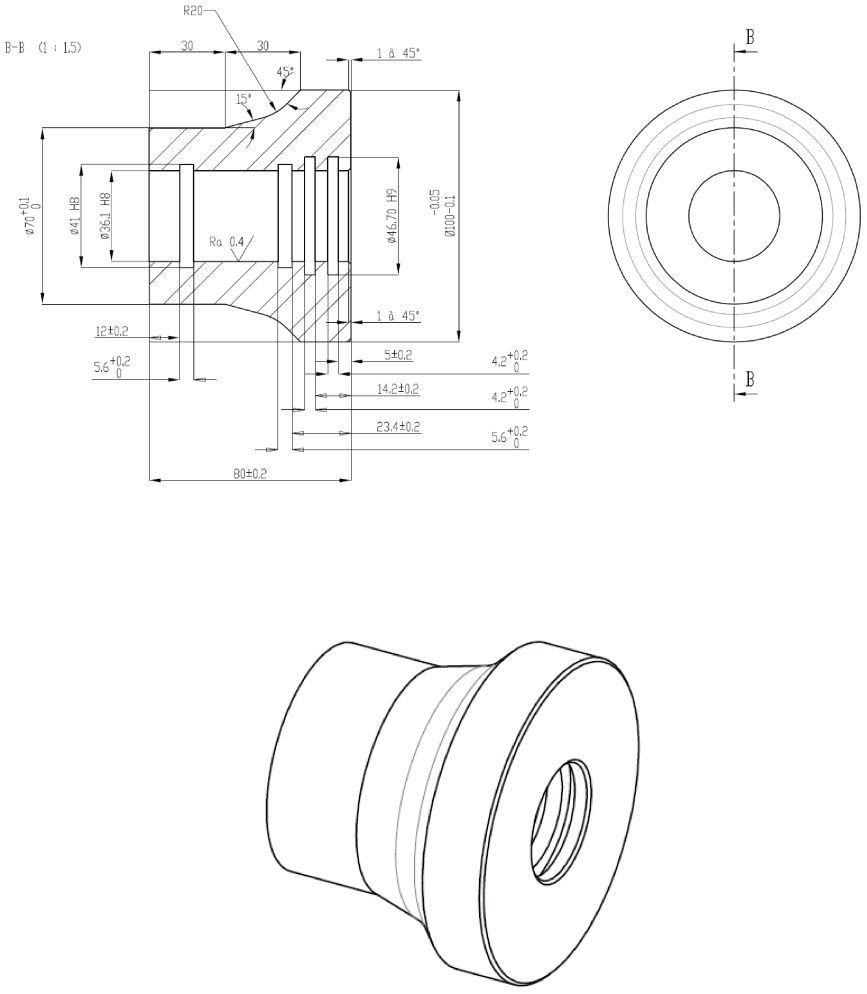

Figure A.2: PTS assembly - Part I

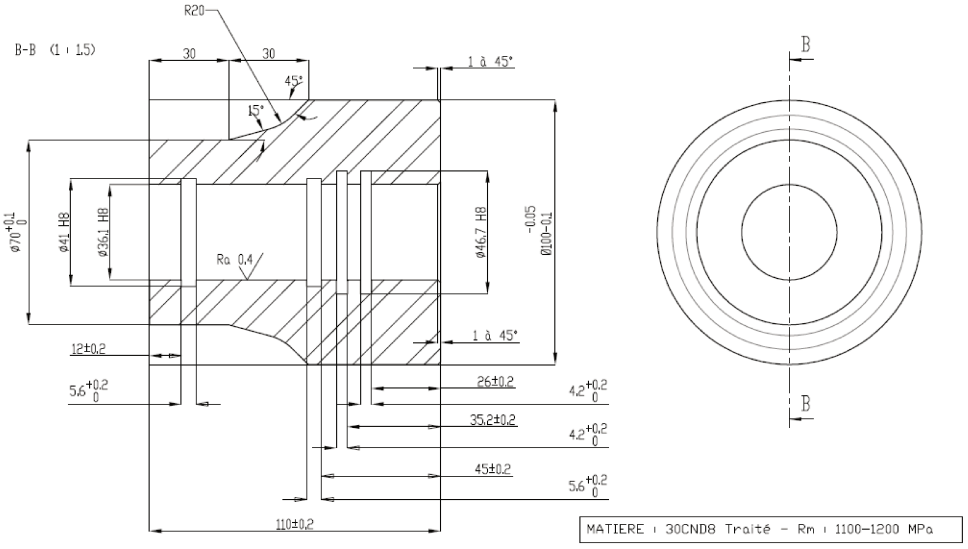

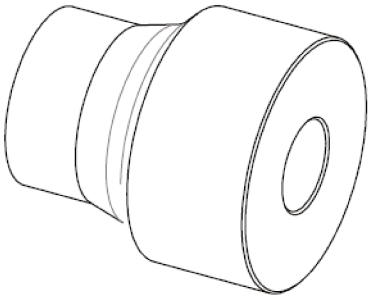

FIGURE A.3: PTS assembly - Part II

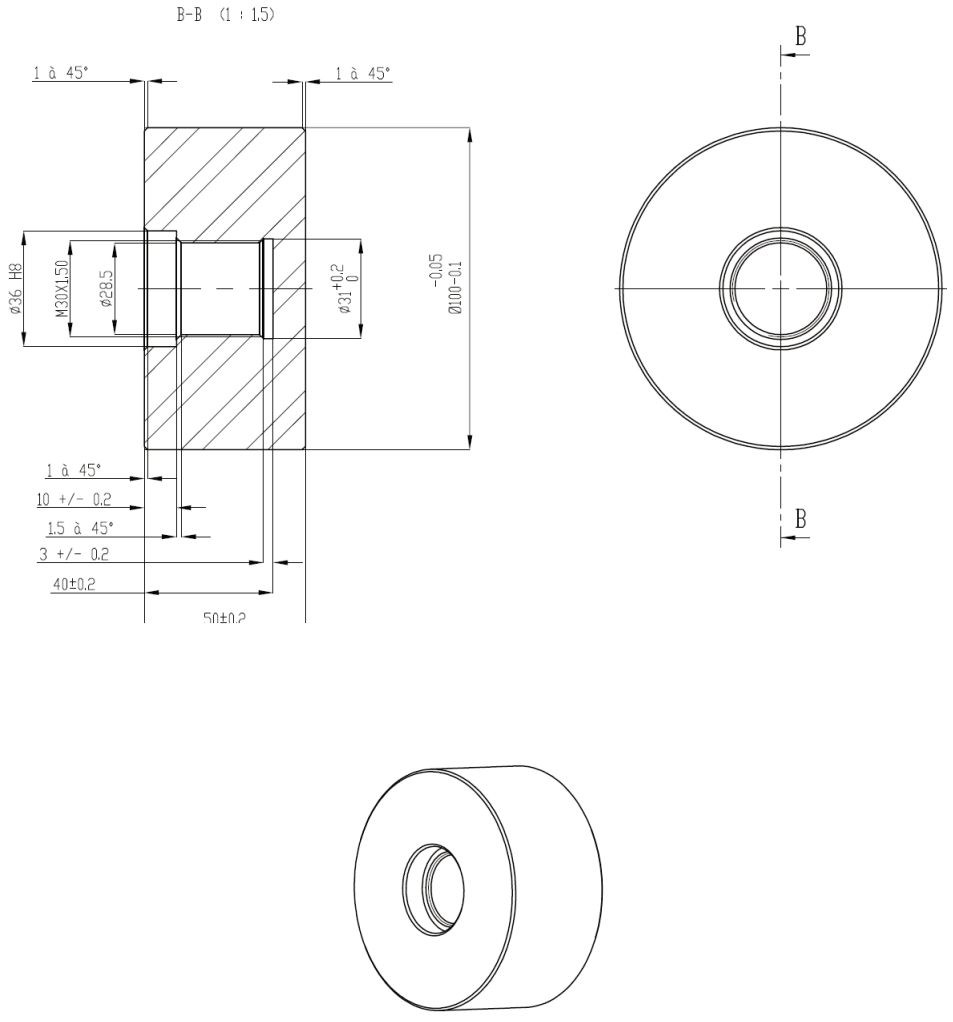

FIGURE A.4: PTS assembly - Part III

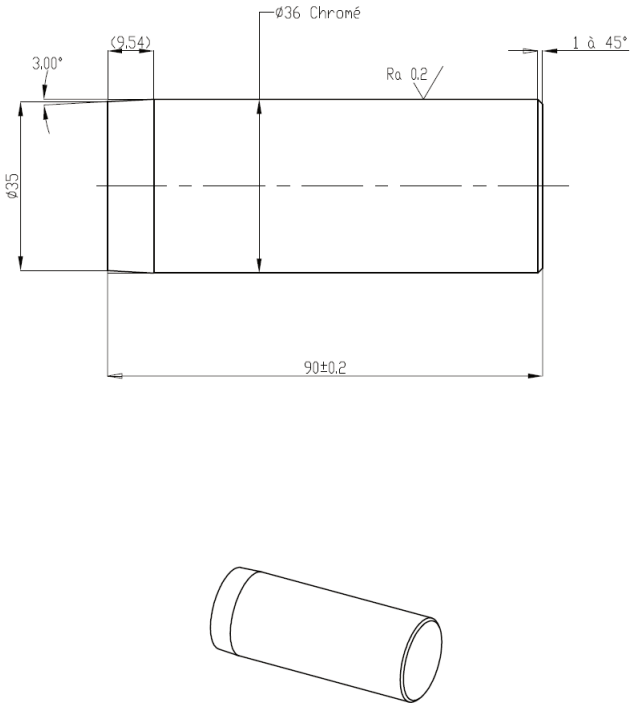

FIGURE A.5: PTS assembly - Part IV

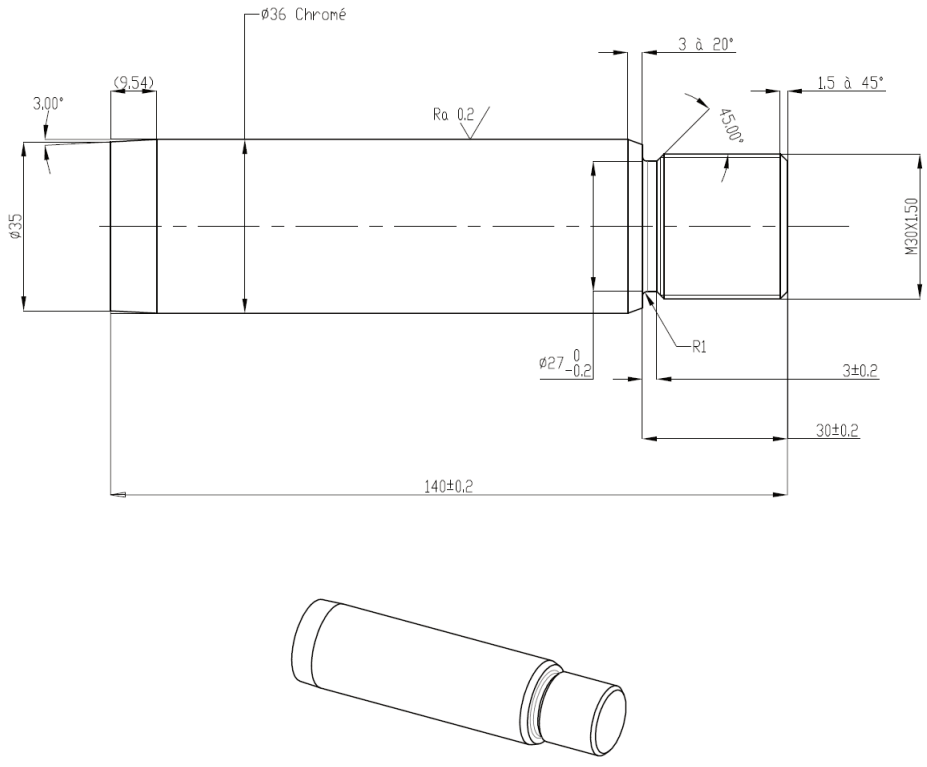

FIGURE A.6: PTS assembly - Part V

Appendix B

Strain gages configuration

B.1 Strain gages configuration

The general Wheatstone bridge, illustrated in Figure B.1, is a network of four resistive legs with an excitation voltage, V_{EX} that is applied across the bridge.

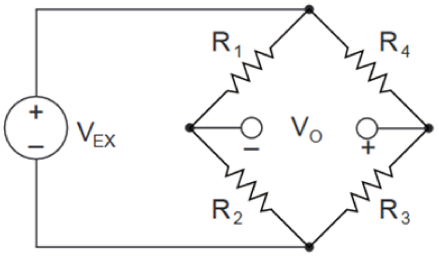

FIGURE B.1: The Wheatstone bridge circuit

The Wheatstone bridge is the electrical equivalent of two parallel voltage divider circuits. R_1 and R_2 compose one voltage divider circuit, and R_3 and R_4 compose the second voltage divider circuit. The output of a Wheatstone bridge, V_0, is measured between the middle nodes of the two voltage dividers.

$$V_0 = [\frac{R_3}{R_3 + R_4} - \frac{R_2}{R_1 + R_2}] \tag{B.1}$$

When R_1 /R_2 = R_4 /R_3, the voltage output V_0 is zero and the bridge is said to be balanced. A change in resistance in any leg of the bridge leads to a nonzero output voltage. Therefore, the number of active legs in the Wheatstone bridge determines the kind of bridge configuration.

B.1.1 Quarter-bridge configuration

The quarter-bridge has one active leg, i.e., one leg with a changing resistance. Let's consider R_0 the nominal resistance of this strain gage, the strain-induced change in resistance, ΔR is given by:

$$\frac{\Delta R}{R_0} = k\frac{\Delta l}{l} = k\varepsilon \tag{B.2}$$

where k is the gage coefficient. The bridge equation can be written to express the strain as function of the measured voltage.

$$\begin{aligned} V_0 &= [\frac{R_0}{R_0 + R_0} - \frac{R_0}{R_0 + \Delta R + R_0}]V_{EX} \\ V_0 &= [\frac{1}{2} - \frac{R_0}{2R_0 + \Delta R}]V_{EX} \\ V_0 &= [\frac{\Delta R}{2(2R_0 + \Delta R)}]V_{EX} \\ V_0 &= [\frac{\Delta R/R_0}{2(2R_0 + \Delta R)}]V_{EX} \\ V_0 &\approx \frac{\Delta R}{4R_0}V_{EX} \end{aligned} \tag{B.3}$$

Since the Output voltage is too small (in the range of few mV), the acquisition card has an amplifier which multiplies V_0 by a gain G and which introduces the relation:

$$\Delta V_{measured} = G.V_0 \tag{B.4}$$

where ΔV_0 is the variation of the voltage measured at the end of the chain measurement. Therefore, from equations (B.2), (B.3) and (B.4) we can derive an expression for the strain gage as a function of the measured voltage:

$$\varepsilon = \frac{4}{K.G.V_{EX}}\Delta V_{measured} \tag{B.5}$$

B.1.2 Full-bridge configuration

In the full-bridge configuration, each of the four gages is considered in the resistances of the bridge. If one considers R_L the resistance of the longitudinal gage and R_T the one for the transversal gage for each set of gages and assuming that the bars are isotropic, one can write:

$$\Delta R_L = k.\varepsilon_L.R_{L_0} \tag{B.6}$$

$$\Delta R_T = -k.\nu.\varepsilon_L.R_{T_0} \tag{B.7}$$

The equation (B.1) of the Wheatstone bridge can thus be written;

$$V_0 = [\frac{R_0 + \Delta R_L}{2R_0 + \Delta R_L + \Delta R_T} - \frac{R_0 + \Delta R_T}{2R_0 + \Delta R_L + \Delta R_T}]V_{EX}$$

$$V_0 = [\frac{\Delta R_L - \Delta R_T}{2R_0 + \Delta R_L + \Delta R_T}]V_{EX} \tag{B.8}$$

By combining equations (B.6) and (B.7) with equation (B.8), we can write:

$$V_0 = [\frac{k.\varepsilon.(1+\nu)}{2}]V_{EX} \tag{B.9}$$

Finally, by using equation (B.4), the relation between the voltage measured and the strain gage deformation is the following:

$$\varepsilon = [\frac{2}{V_{EX}.k.G.(1+\nu)}].\Delta V_{measured} \tag{B.10}$$

Appendix C

Mesoscopic Simulations

A 3D mesoscopic modeling for the numerical analysis of the shear behavior of concrete is proposed. The real micro-structure of concrete is simulated where two different phases are differentiated: the mortar paste which includes the cement past with sand and fine aggregates and the aggregates. An anisotropic damage model is used to simulate the behavior of concrete under shear. It correctly reproduces the damage zones observed on actual samples which can help in the understanding of meso-scale phenomena and their influence on macro-scale behavior.
Because of the geometry of the sample, there is a presence of distorted finite elements during meshing. This should be avoided by choosing the best random distribution and meshing technique. Due to time constraints, this issue could not be developed in this report. A lot of hypothesis were taken into account in order to reduce the computational time and some results are presented to validate the model even though they don't represent the correct values.

C.1 Mesoscopic method principles

Concrete is a multi-scale material which include aggregates, sand, cement and pores. To improve the understanding of the concrete behavior, the properties of these individual components have to be taken into account (Wriggers and Moftah [2006], Segurado and Llorca [2002], Schlangen and Van Mier [1992], Erzar and Forquin [2011] and Caballero et al. [2006]). Some authors considered the concrete a biphasic material composed of coarse aggregates embedded in mortar (Comby-Peyrot et al. [2009]). Others authors introduced the interfacial transition zone as a third component (Caballero et al. [2006]). These elements were inserted along all potential crack planes in the mesh.

Due to high computational costs the majority of the models existing in the literature have been developed in 2D. However, recently, more models are developed in 3D due to the increase of the computational power.

The mesoscopic models were used for different applications. Wriggers and Moftah [2006] applied the model for unconfined compression tests, Dupray et al. [2009] for triaxial tests and Erzar and Forquin [2011] studied the behavior of concrete under impact. The different methods allowed the understanding of the local mechanisms inside concrete and the better simulation of damage initiation and growth.

C.2 Application on punching-through shear test

C.2.1 Geometry

The generation process of the spheres is relatively complex. A python code has been written taking into consideration the random structure of the aggregates, similar to the real R30A7 concrete composed of six classes as shown in Figure C.1. The volume fraction of aggregates with respect to the concrete volume is 40%. The attribution of each sphere inside the concrete volume starts with the largest particles.

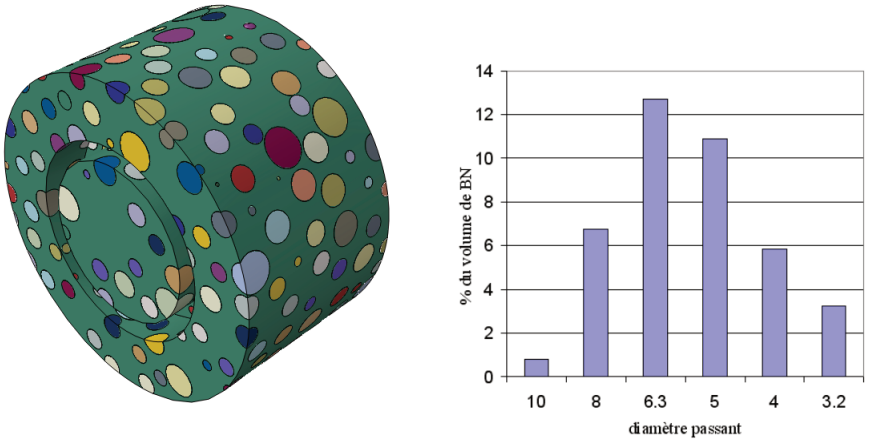

(a) (b)

FIGURE C.1: (a) Heterogeneous concrete sample generated by Abaqus (b) Particle size distribution

To represent the real distribution of aggregates in concrete, the technique used is resumed in these 4 steps (Wriggers and Moftah [2006]):

- Define the size of aggregate and the volume percentage of each size.
- Calculate the number of aggregates for each size.

- Place the aggregates into the sample, the bigger aggregates are placed first, the aggregates are distributed until the volume of aggregates to be generated is not enough to generate another particle.
- The distance between two adjacent particles should exceed a minimum value, it was fixed to 1.05*(R[s]+R[s-1]) where R[s] is the radius of the particle being generated and R[s-1] the radius of the particle already present in the volume.

In the study, aggregates are generated beyond the cylindrical surfaces inside a cubic shape and then are cut as shown in Figure C.1. Afterwards, the geometry of the cylindrical specimen with the top and bottom notches is drawn.

C.2.2 Mesh and loading

The C3D10M, a 10-node modified quadratic tetrahedron, was assigned to the aggregates to create the mesh. Then, the loading which consists of a hydrostatic pressure in the first stage and of an axial loading in the second stage, is applied (Figure C.2).

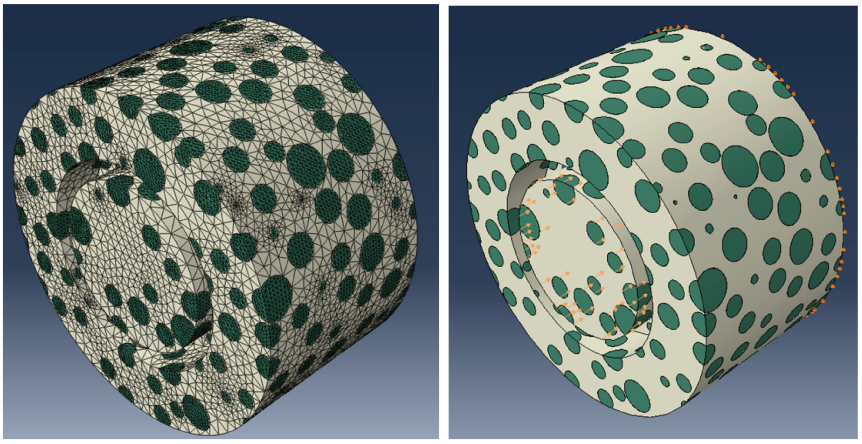

(a) (b)

FIGURE C.2: Mesh and loading of the mesoscopic model

C.2.3 Model parameters

An elastic behavior of aggregates is assumed and an anisotropic damage model (DFH) coupled with a plasticity model (KST) have been used to represent the matrix. The DFH model accounts for single and multiple fragmentation process with a cohesive law, based on the approach of weakest link theory and Weibull model. It describes the initiation of cracks and the obscuration of critical defects under high strain-rate. A detailed description of this model can be found in Forquin and Hild [2008] and Hild [2015]. The KST model is developed to simulate the behavior of geo-materials under

	Matrix (Saturated)	**Concrete (Saturated)**	**Aggregates**
γ (kg/m^3)	2170	2380	2700
Elastic parameters			
E (GPa)	27.5	42	70
ν	0.19	0.2	0.2
Hydrostatic parameters			
K^{final} (Pa)	2.3x10^{10}	2.3x10^{10}	
(ϵ_i, P_i) (MPa)	(0,0)	(0,0)	
	(-0.0024,30)	(-0.0017,30)	
	(-0.067,135)	(-0.025,100)	
	(-0.084,207)	(-0.045,195)	
	(-0.089,300)	(-0.055,300)	
	(-0.093,360)	(-0.065,500)	
	(-0.102,535)	(-0.073,700)	
	(0.112,750)	(-0.08,900)	
Deviatoric parameters			
a_0 (MPa^2)	1.61x10^{15}	1.61x10^{15}	
a_1 (MPa)	5x10^7	9.8x10^7	
a_2	0.275	0.54	
$\sigma_{eq}{}^{max}$	105	210	
Weibull parameters for DFH model			
σ_w (MPa)	6.1	6.1	
V_{eff} (mm^3)	284	284	
m	12	12	
Crack Velocity parameter			
k	0.38	0.38	

TABLE C.1: Identification of concrete and matrix parameters of saturated R30A7 concrete (Erzar and Forquin [2011])

high confining pressure The identification of the DFH and KST model are identified from experimental data in Erzar and Forquin [2011] and are reported in Table C.1.

C.2.4 Simplified model

In order to simplify the calculation and reduce the computational time, only aggregates present in the unnotched zone are simulated. For the remaining zone, the elements are assigned the concrete parameters (Figure C.3). Moreover, in the following simulations, only the aggregates having a diameter larger than 5 mm were generated and the total volume of aggregates inside the sample doesn't exceed the 20%. These approximations

were assumed in order to show some results but future work should be considered to account as close as possible to a real representation of heterogeneities.

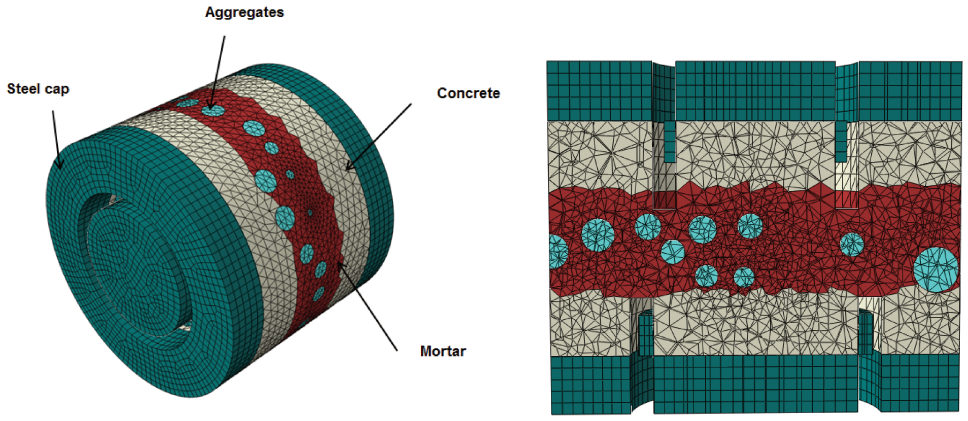

(a) (b)

FIGURE C.3: (a) A 3D view of the simplified mesoscopic model (b) A cut inside the sample

C.3 Preliminary Results

A 3D homogeneous model was simulated and the material parameters of concrete as listed in Table C.1 are assigned to the elements. The mesh of this homogeneous model is represented in Figure C.4.

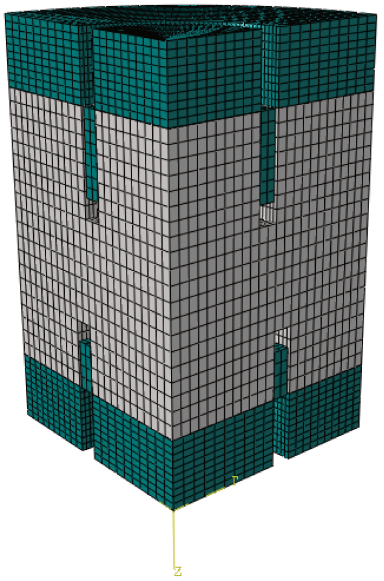

FIGURE C.4: The mesh of the homogeneous shear model

The results obtained by this homogeneous model and the ones obtained with the mesoscopic model are compared to data obtained with experiments. The axial force as function of the vertical displacement is plotted in Figure C.5. A good correlation is observed for the homogeneous mesh with the experiments. However, the calculation in the mesoscopic model was not able to reach high level of axial displacement, this is mainly caused by the over-deformation of the elements located in the shearing zone.

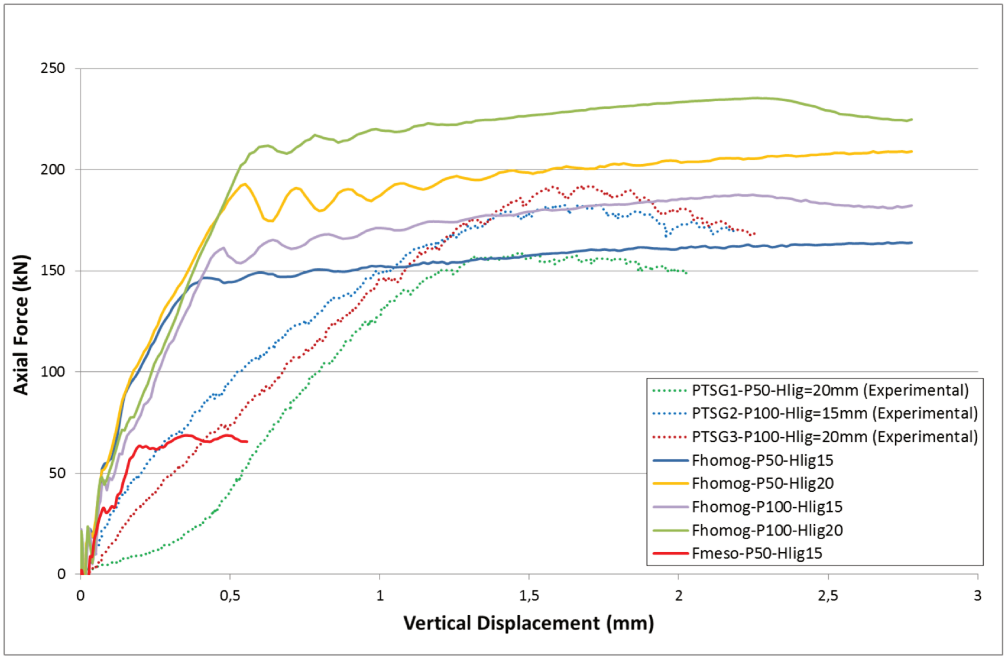

FIGURE C.5: Axial force obtained from experimental tests and numerical models for different confining levels and ligament lengths

The shear strength and the damage field inside the concrete sample for the homogeneous and the mesoscopic models are represented in Figure C.6 and Figure C.7 respectively. The distribution of stresses inside the ligament and of the damage in the shear zone are observed in both simulations.

The numerical model presented herein is a very simplified model of the mesoscale mechanics in concrete but it already reproduces the shear behavior of concrete during punch-through shear test. The real volume of aggregate should be used and a special attention should be paid in order to avoid distorted finite elements. A sensitivity study on various parameters can be done. The effects of the voids, of the aggregates shape and composition and the aggregate/mortar interface could be studied. In addition, an identification of the models parameters should be done in order to reproduce the peak and the post peak behavior.

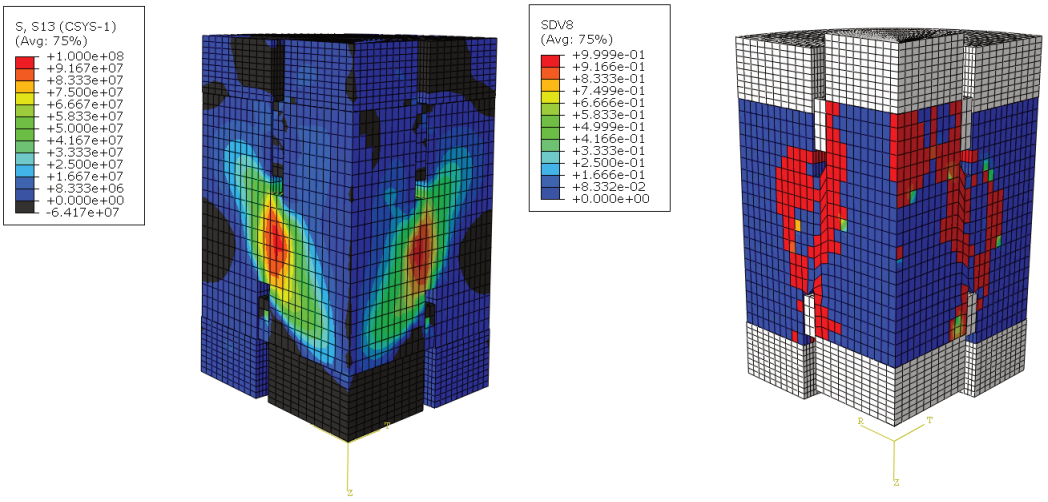

(a) (b)

FIGURE C.6: Homogeneous numerical simulation of shear test after 0.5 mm of displacement (a) Shear Stresses (b) Damage

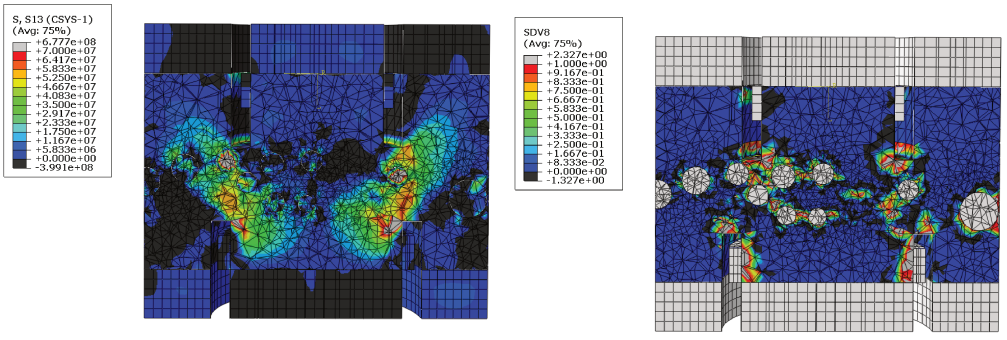

(a) (b)

FIGURE C.7: Mesoscopic numerical simulation of shear test after 0.5 mm of displacement (a) Shear Stresses (b) Damage

Bibliography

Backers, T. (2004). *Fracture Toughness Determination and Micromechanics of Rock Under Mode I and Mode II Loading*. PhD thesis, Potsdam University.

Backers, T., Dresen, G., Rybacki, E., and Stephansson, O. (2004). New data on mode II fracture toughness of rock from the Punch-Through Shear test. *International Journal of Rock Mechanics and Mining Sciences*, 41(3):1–6.

Backers, T. and Stephansson, O. (2012). ISRM Suggested Method for the Determination of Mode II Fracture Toughness. *Rock Mechanics and Rock Engineering*, 45(6):1011–1022.

Backers, T., Stephansson, O., and Rybacki, E. (2002). Rock fracture toughness testing in Mode II - punch-through shear test. *International Journal of Rock Mechanics and Mining Sciences*, 39:755–769.

Bailly, P. (1994). Une modélisation d'un matériau fragile avec prise en compte d'effets dynamiques. *Compte Rendu Académie des Sciences*, Série II:727–732.

Bailly, P., Tombini, C., and Le Vu, O. (1996). Modélisation de géomatériaux sous sollicitations dynamiques élevées. i : Un tir de pénétration sur cible en béton,. *Colloque du réseau GEO,Aussois, 2-6 décembre, France.*

Barr, B. and Derradj, M. (1990). Numerical study of a shear (mode II) type test specimen geometry. *Eng. Fract. Mech.*, 35:171–180.

Bazant, Z. P., Bishop, F. C., and Chang, T.-p. (1986). Confined Compression tests of cement paste and concrete up to 300 ksi. *ACI journal proceedings*, 83:553–560.

Bazant, Z. P. and Pfeiffer, P. A. (1986). Shear fracture tests of concrete. *Materials and Structures*, 19(110):111–121.

Bischoff, P. and Perry, S. (1995). Impact behavior of plain concrete loaded in uniaxial compression. *Journal of Engineering Mechanics*, 121:685–693.

Burlion, N. (1997). *Compaction des bétons: éléments de modeélisation et caractérisation expérimentale*. PhD thesis, Ecole Normale Supérieure de Cachan, France.

Burlion, N. (2004). Quelques résultats sur le couplage séchage – comportement mécanique des matériaux cimentaires. Technical report.

Burlion, N. and Gatuingt, F. Concrete under high compaction: a new experimental method. *Fracture mechanics of concrete structures*, pages 605–614.

Burlion, N., Gatuingt, F., Pijaudier-Cabot, G., and Daudeville, L. (2000). Compaction and tensile damage in concrete: constitutive modelling and application to dynamics. *Computer Methods in Applied Mechanics and Engineering*, 183(3):291 – 308.

Burlion, N., Pijaudier-Cabot, G., and Dahan, N. (2001). Experimental analysis of compaction of concrete and mortar. *International Journal for Numerical and Analytical Methods in Geomechanics*, 25(15):1467–1486.

Caballero, A., Carol, I., and López, C. M. (2006). A meso-level approach to the 3D numerical analysis of cracking and fracture of concrete materials. *Fatigue & Fracture of Engineering Materials and Structures*, 29(12):979–991.

Cadoni, E., Labibes, K., Albertini, C., Berra, M., and Giangrasso, M. (2001). Strain-rate effect on the tensile behaviour of concrete at different relative humidity levels. *Materials and Structures*, 34(1):21.

Carol, I., Prat, P., and Lopez, C. (1997). Normal/Shear cracking model: Application to discrete crack analysis. *Journal of Engineering Mechanics*, 123(8).

Chen, W. and Ravichandran, G. (1996). An Experimental Technique for Imposing Dynamic Multiaxial-compression with Mechanical Confinement. *Experimental Mechanics*, 36(2):155–158.

Chen, W. and Ravichandran, G. (1997). Dynamic compressive failure of a glass ceramic under lateral confinement. *Journal of the Mechanics and Physics of Solids*, 45(8):1303–1328.

Comby-Peyrot, I., Bernard, F., Bouchard, P.-O., Bay, F., and Garcia-Diaz, E. (2009). Development and validation of a 3D computational tool to describe concrete behaviour at mesoscale. Application to the alkali-silica reaction. *Computational Materials Science*, 46(4):1163–1177.

Drucker, D. and Prager, W. (1952). Soil mechanics and plastic analysis or limit design. *Quaterly of Applied Mathematics*, 10:157–165.

Dupray, F., Malecot, Y., Daudeville, L., and Buzaud, E. (2009). A mesoscopic model for the behaviour of concrete under high confinement. (January):1407–1423.

Erzar, B. (2010). *Ecaillage, cratérisation et comportement en traction dynamique de bétons sous impact : approches expérimentales et modélisation.* PhD thesis, Université Paul Verlaine-Metw.

Erzar, B. and Forquin, P. (2011). Experiments and mesoscopic modelling of dynamic testing of concrete. *Mechanics of Materials*, 43(9):505–527.

Erzar, B. and Forquin, P. (2014). Analysis and modelling of the cohesion strength of concrete at high strain-rates. *International Journal of Solids and Structures*, 51(14):2559–2574.

Forquin, P. (2003). *Endommagement et fissuration de matériaux fragiles sous impact balistique.* PhD thesis, Ecole Normale Supérieure de Cachan, France.

Forquin, P. (2011a). Influence of free water and strain-rate on the shear behaviour of concrete. *Applied mechanics and materials*, 82:148–153.

Forquin, P. (2011b). Influence of strain-rate and confining pressure on the shear strength of concrete. In *Dynamic Behavior of Materials, Volume 1*, chapter Proceeding, pages 29–35. Springer New York.

Forquin, P., Arias, A., and Zaera, R. (2006). An experimental method of measuring the confined compression strength of high-performance concretes. *EDP Sciences*, 134:629–634.

Forquin, P., Arias, a., and Zaera, R. (2007). An experimental method of measuring the confined compression strength of geomaterials. *International Journal of Solids and Structures*, 44(13):4291–4317.

Forquin, P., Arias, a., and Zaera, R. (2008a). Relationship Between Mesostructure, Mechanical Behaviour and Damage of Cement Composites Under High-Pressure Confinement. *Experimental Mechanics*, 49(5):613–625.

Forquin, P., Arias, a., and Zaera, R. (2008b). Role of porosity in controlling the mechanical and impact behaviours of cement-based materials. *International Journal of Impact Engineering*, 35(3):133–146.

Forquin, P. and Erzar, B. (2009). Dynamic fragmentation process in concrete under impact and spalling tests. *International Journal of Fracture*, 163(1-2):193–215.

Forquin, P., Gary, G., and Gatuingt, F. (2008c). A testing technique for concrete under confinement at high rates of strain. *International Journal of Impact Engineering*, 35(6):425–446.

Forquin, P. and Hild, F. (2008). Dynamic Fragmentation of an Ultra-High Strength Concrete during Edge-On Impact Tests. *ASCE Journal of Engineering Mechanics*, 134(4):302–315.

Forquin, P. and Hild, F. (2010). *A probablistic damage model of the dynamic fragmentation process in brittle materials*, volume 44. Elsevier Inc.

Forquin, P., Nasraoui, M., Rusinek, a., and Siad, L. (2012). Experimental study of the confined behaviour of PMMA under quasi-static and dynamic loadings. *International Journal of Impact Engineering*, 40-41(August):46–57.

Forquin, P., Piotrowska, E., and Gary, G. (2015a). Experimental Characterization of the Confined Behaviour of Concrete . Influence of Saturation Ratio and Strain-Rate. In *Dymat 2015, Lugano, Switzerland; EPJ web of conferences 94*.

Forquin, P., Safa, K., and Gary, G. (2010). Influence of free water on the quasi-static and dynamic strength of concrete in confined compression tests. *Cement and Concrete Research*, 40(2):321–333.

Forquin, P. and Sallier, L. (2012). Compte rendu d'avancement de contrat intitulé: Ecaillage, cratérisation et comportement en traction dynamique de béton. Technical report.

Forquin, P. and Sallier, L. (2013). A testing technique to characterise the shear behaviour of concrete at high strain-rates. In Chalivendra, V., Song, B., and Casem, D., editors, *Dynamic behavior of Materials, Volume1*, pages 531–536. Springer New York.

Forquin, P., Sallier, L., and Pontiroli, C. (2015b). A numerical study on the influence of free water content on the ballistic performances of plain concrete targets. *Mechanics of Materials*, 89(Supplement C):176 – 189.

Gabet, T. (2006). *Comportement triaxial du béton sous fortes contraintes*. PhD thesis, Université Joseph Fourier.

Gabet, T., Malécot, Y., and Daudeville, L. (2008). Triaxial behaviour of concrete under high stresses: Influence of the loading path on compaction and limit states. *Cement and Concrete Research*, 38(3):403–412.

Gary, G. and Klepaczko, J. (1992). Résumé des résultats expérimentaux sur mini-béton, essais de compression greco géomatériaux. *Rapport scientifique, projet 1.3, dynamique des bétons et des roches*, pages 105–118.

Gatuingt, F. (1999). *Prévision de la rupture des ouvrages en béton sollicités en dynamique rapide*. PhD thesis.

Griffith, A. (1921). The phenomena of rupture and flow in solids. *Philosophical Transactions of the Royal Society of London. Series A*, 221:163–198.

Hakami, H. and Stephansson, O. (1990). Shear fracture energy of stripa granite – results of controlled triaxial testing. *Eng. Fract. Mech.*, 35:855–865.

Hanchak, S., Forrestal, M., Young, E., and Ehrgott, J. (1992). Perforation of concrete slabs with 48 MPa (7 ksi) and 140 MPa (20 ksi) unconfined compressive strengths. *International Journal of Impact Engineering*, 12(1):1 – 7.

Heukamp, F., Ulm, F.-J., and Germaine, J. (2001). Mechanical properties of calcium leached cement paste: triaxial stress states and the influence of pore pressure. *Cement and Concrete Research*, 31:767–774.

Hild, F. (2015). Mechanics of Materials On characteristic parameters involved in dynamic fragmentation processes. *Mechanics of Materials*, 80:340–350.

Ingraffea, A. (1981). Mixed mode fracture initiation in indiana limestone and westerly granite. *Proc. 22nd US Symp. Rock Mech., Cambridge, MA.*, pages 186–191.

Irwin, G. (1958). *Fracture. In: Handbuch der Physik. Springer Verlag, Berlin, Vol. 6.*

Kolsky, H. (1949). An Investigation of the Mechanical Properties of Materials at very High Rates of Loading. *Proceedings of the Physical society. Section B*, 62(11):676–700.

Li, Q. M., Reid, S. R., Wen, H. M., and Telford, A. R. (2005). Local impact effects of hard missiles on concrete targets. *International Journal of Fracture*, 32:224–284.

Lukić, B. and Forquin, P. (2015). Experimental characterization of the punch through shear strength of an ultra-high performance concrete. *International Journal of Impact Engineering*, 91:34–45.

Luong, M. (1990). Tensile and shear strenghts of concrete and rock. *Engineering Fracture Mechanics*, 35(1/2/3):127–135.

Luong, M. (1992). Fracture testing of concrete and rock materials. *Nuclear engineering and design*, 133:83–95.

Martin, B., Kabir, M. E., and Chen, W. (2013). Undrained high-pressure and high strain-rate response of dry sand under triaxial loading. *International Journal of Impact Engineering*, 54:51–63.

Meyers, M. A. *Dynamic Behavior of materials.* John Wiley & Sons, New York.

Montenegro, O., Sfer, D., Lopez, C., and Carol, I. (2013a). 3D numerical model of a confined fracture tests in concrete. In *XII International Conference on Computational Plasticity Fundamentals and Applications COMPLAS XII*, pages 470–478.

Montenegro, O., Sfer, D., López, C. M., and Carol, I. (2013b). Experimenal tests and numerical modeling to identify the asymptotic shear-compression mode IIA of concrete fracture. In *VIII International Conference on Fracture Mechanics of Concrete and Concrete Structures FraMCoS-8*.

Montenegro, O. I., Sfer, D., and Carol, I. (2007). Characterization of concrete in mixed mode fracture under confined conditions. In *ICEM13 conference, Alexandroupolis, Greece*.

Pedersen, R. R., Simone, A., and Sluys, L. J. (2013). Mesoscopic modeling and simulation of the dynamic tensile behavior of concrete. *Cement and Concrete Research*, 50:74–87.

Piotrowska, E. (2013). *Role of coarse aggregates in the triaxial behavior of concrete : experimental and numerical*. PhD thesis, Université de Grenoble.

Piotrowska, E. and Forquin, P. (2015). Experimental Investigation of the Confined Behavior of Dry and Wet High-Strength Concrete: Quasi Static Versus Dynamic Loading. *Journal of Dynamic Behavior of Materials*, 1(2):191–200.

Piotrowska, E., Forquin, P., and Malecot, Y. (2016). Experimental study of static and dynamic behavior of concrete under high confinement: Effect of coarse aggregate strength. *Mechanics of Materials*, 92:164–174.

Piotrowska, E., Malecot, Y., and Ke, Y. (2014). Experimental investigation of the effect of coarse aggregate shape and composition on concrete triaxial behavior. *Mechanics of Materials*, 79:45–57.

Poinard, C. (2010). *Comportement du béton sous chargement triaxial sévère : analyse tomographique et modélisation à l'échelle mésoscopique*. PhD thesis, Université de Grenoble.

Poinard, C., Piotrowska, E., Malecot, Y., Daudeville, L., and Landis, E. N. (2012). Compression triaxial behavior of concrete: the role of the mesostructure by analysis of X-ray tomographic images. *European Journal of Environmental and Civil Engineering*, 16(sup1):115–136.

Pontiroli, C., Erzar, B., and Buzaud, E. (2014). Concrete behaviour under ballistic impacts : effects of materials parameters to penetration resistance and modeling with PRM model. In *Computational Modeling of Concrete and Concrete Structures (EURO-C 2014)*, number JANUARY 2014.

Pontiroli, C., Rouquand, A., and Mazars, J. (2010). Predicting concrete behaviour from quasi-static loading to hypervelocity impact. *European Journal of Environmental and Civil Engineering*, 14(6-7):703–727.

Prasad, M., Hasan, N., Kumar, A., Kumar, H., Engineering, M., Pradesh, U., and Delhi, N. (2011). Design studies of a square ring shaped force sensor. 1(4):727–733.

Rao, Q. (1999). Pure shear fracture of brittle rock. *Doctoral thesis, Division of Rock Mechanics, Luleå University, Sweden.*

Ravichandran, G. (1995). Modeling constitutive behavior of particulate composites undergoing damage. 32(6):979–990.

Rice, J. (1980). The mechanics of earthquake rupture. *In: Dziewonski, A.M. and Boschi, E. (eds.). Physics of the Earth's Interior, Italy*, pages 555–649.

Rittel, D. and Brill, A. (2008). Dynamic flow and failure of confined polymethylmethacrylate. *Journal of the Mechanics and Physics of Solids*, 56(4):1401–1416.

Rossi, P. (1991). A physical phenomenon which can explain the material behaviour of concrete under high strain rates. *Materials and Structures*, 24:422–424.

Safa, K. (2008). *Mise au point d'un essai de compaction dynamique. Application au béton.* PhD thesis, Ecole Polytechnique.

Schlangen, E. and Van Mier, J. G. M. (1992). Experimental and Numerical Analysis of Micromechanisms of Fracture of Cement-Based Composites. 14:105–118.

Schmidt, M. J., Cazacu, O., and Green, M. L. (2009). Experimental and theoretical investigation of the high-pressure behavior of concrete. *International Journal for Numerical and Analytical Methods in Geomechanics*, 33:1–23.

Segurado, J. and Llorca, J. (2002). A numerical approximation to the elastic properties of sphere-reinforced composites. 50:2107–2121.

Sfer, D., Carol, I., Gettu, R., and Etse, G. (2002). Study of the Behavior of Concrete under Triaxial Compression. *Journal of Engineering Mechanics*, 128(2):156–163.

Srinath, L. S. and Acharya, Y. V. G. (1953). Stresses in a circular ring. Comparison of theory with experiment. *Applied Sciences Research*, 4:189–194.

Timoshenko, S. and Goodier, J. (1951). *Theory of Elasticity.* Mcgraw hill book company edition.

Torrenti, J.-M., Pijaudier-Cabot, G., and Reynouard, J.-M. *Mechanical Behavior of Concrete.* John Wiley & Sons.

Toutlemonde, F. (1994). *Résistance au choc des structures en béton: du comportement du materiau au calcul des ouvrages.* PhD thesis, Ecole Nationale des Ponts et Chaussées.

Vu, X. D. (2013). *Vulnérabilité des ouvrages en béton sous impact : Caractérisation, modélisation, et validation*. PhD thesis, Université de Grenoble.

Vu, X.-H. (2007). *Caractérisation expérimentale du béton sous fort confinement : influences du degré de saturation et du rapport eau / ciment*. PhD thesis, Université Joseph Fourier.

Vu, X.-H., Malecot, Y., Daudeville, L., and Buzaud, E. (2009a). Effect of the water/cement ratio on concrete behavior under extreme loading. *International Journal for Numerical and Analytical Methods in Geomechanics*, 33:1867–1888.

Vu, X.-H., Malecot, Y., Daudeville, L., and Buzaud, E. (2009b). Experimental analysis of concrete behavior under high confinement: Effect of the saturation ratio. *International Journal of Solids and Structures*, 46(5):1105–1120.

Warren, T. L., Fossum, A. F., and Frew, D. J. (2004). Penetration into low-strength (23 MPa) concrete : target characterization and simulations. 30:477–503.

Watkins, J. (1983). Fracture toughness test for soil-cement samples in mode II. *International Journal of Fracture*, 23:135–138.

Watkins, J. and Liu, K. (1985). A finite element study of the short beam test specimen under mode II loading. *Int. J. Cement Composites and Lightweight*, 7:39–47.

Williams, E. M., Akers, S. A., and Reed, P. A. (2006). Laboratory characterization of sam-35 concrete. *Rapport technique ERDC/GSL TR-06-150. US Army Engineer Research and Development Center*.

Wriggers, P. and Moftah, S. (2006). Mesoscale models for concrete: Homogenisation and damage behaviour. *Finite Elements in Analysis and Design*, 42(7):623–636.

Wu, H., Kemeny, J., and Wu, S. (2017). Experimental and numerical investigation of the punch-through shear test for mode II fracture toughness determination in rock. *Engineering Fracture Mechanics*, 184:59–74.

Xu, Z., Ding, X., Zhang, W., and Huang, F. (2017). A novel method in dynamic shear testing of bulk materials using the traditional SHPB technique. *International Journal of Impact Engineering*, 101:90–104.

Yao, W., Xu, Y., Yu, C., and Xia, K. (2017). A dynamic punch-through shear method for determining dynamic Mode II fracture toughness of rocks. *Engineering Fracture Mechanics*, 176:161–177.

Zhang, M., Shim, V., Lu, G., and Chew, C. (2005). Resistance of high-strength concrete to projectile impact. *International Journal of Impact Engineering*, 31(7):825 – 841.

Zhao, H. and Gary, G. (1996). On the use of SHPB techniques to determine the dynamic behavior of materials in the range of small strains. *International Journal of Solids and Structures*, 33(23):3363 – 3375.

Zingg, L. (2013). *Influence de la porosité et du degré d'humidité interne sur le comportement triaxial du béton.* PhD thesis, Université de Grenoble.

Zingg, L., Briffaut, M., Baroth, J., and Malecot, Y. (2016). Influence of cement matrix porosity on the triaxial behaviour of concrete. *Cement and Concrete Research*, 80:52–59.

Zukas, J. (1990). *High Velocity Impact Dynamics.* John Wiley & Sons.

Zukas, J. (1992). Penetration and perforation of solids. *Impact Dynamics. Krieger Publishing Co.*

List of Figures

List of Tables